

Dissertation

submitted to the
Combined Faculties for the Natural Sciences and for
Mathematics
of the Ruperto-Carola University of Heidelberg, Germany
for the degree of
Doctor of Natural Sciences

Presented by
Dipl.-Phys. Thomas Pflüger
born in
Landau in der Pfalz

Oral examination: 02.05.2012

Electron Impact Ionization Studies of Small Rare Gas Clusters

Referees: Priv.-Doz. Dr. Alexander Dorn
Prof. Dr. Andreas Wolf

Zusammenfassung

Die durchgeführten Experimente, über die diese Arbeit berichtet, haben zum Ziel, Einblick in die Dynamik von Stößen zwischen Elektronen und kleinen Edelgasclustern zu geben. Hierzu wurden kinematisch vollständige ($e, 2e$) Experimente an Argondimeren und kleinen Argon-Clustern mit 100 eV Stoßenergie durchgeführt. Verglichen mit den gleichzeitig gemessenen atomaren Daten, zeigen die Wirkungsquerschnitte eine erhöhte Wahrscheinlichkeit für zusätzliche elastische Stöße mit zunehmender Clustergröße. In einem zweiten Experiment wurden mit 61 eV schnellen Elektronen Neondimere ionisiert. Hier zeigten die gemessenen dreifach differentiellen Wirkungsquerschnitte deutliche Unterschiede zu den simultan gemessenen atomaren Wirkungsquerschnitten, welche sich in Form von Keulen darstellen. Diese geben erste Hinweise auf den Einfluss molekularer Orbitalsymmetrien beim Ionisationsprozess in Dimeren. Zusätzlich wurde die dissoziative Ionisation von Argondimeren in zwei geladene Fragmente mit 120 eV Elektronen untersucht. Der Zerfall in zwei einfach geladene Ionen offenbarte zwei Reaktionspfade: die sequentielle Ionisation und die Doppelionisation eines Dimerbestandteils mit nachfolgendem radiativen Zerfallsprozess. Der dreifach geladene Endzustand konnte dem interatomaren Coulombzerfall zugeordnet werden, einem ultraschnellen Prozess der eng mit dem Augerzerfall verwandt ist. Für alle Zerfallskanäle wurden Winkelverteilungen sowohl von den Ionen als auch von den emittierten Elektronen aufgetragen.

Abstract

The course of experiments reported in this work is dedicated to give insight into the collision dynamics between electrons and small rare gas clusters. Kinematically complete ($e, 2e$) experiments were performed for the ionization of argon dimers and small argon clusters with 100 eV impact energy. Compared to parallel measured data for atomic argon, the cross-sections reveal a significant probability of additional elastic scattering processes for increasing target size. In a second experiment 61 eV electrons were used to ionize neon dimers. The obtained triple-differential cross-sections show distinct differences in form of lobes that are not observed for the simultaneously obtained atomic cross-sections. These give first indications for the influence of molecular orbitals symmetries in the ionization process in dimers. Furthermore, the dissociation of argon dimers into two charged fragments was studied by 120 eV electrons. The fragmentation into two singly-charged ions reveals two different pathways: one by sequential ionization, the other by double ionization of one constituent and a subsequent radiative decay process. The triply-charge final state, could be assigned to interatomic coulombic decay, an ultra-fast process closely related to the Auger decay. For all studied channels angular distributions of the ionic fragments as well as for the emitted electrons are presented.

Contents

1. Introduction	1
2. Brief Introduction to Electron Impact Ionization	7
2.1. An Introduction to $(e, 2e)$ Experiments	7
2.2. Theoretical Models in $(e, 2e)$ Reactions	18
2.2.1. The Lippman-Schwinger Equation	20
2.2.2. Distorted-Wave Approximation	23
2.3. Van der Waals Molecules	26
2.3.1. Interatomic Coulombic Decay	31
2.3.2. Two-center Interference Model	35
3. The Reaction Microscope	43
3.1. Spectrometer	43
3.2. Position Sensitive Detectors	45
3.2.1. Microchannel Plate	46
3.2.2. Delayline Anode	48
3.2.3. Wedge-and-Strip Anode	50
3.3. Target	54
3.4. Electron Gun	57
3.5. Data Acquisition	58
4. Data Processing and Analysis	61
4.1. Data Analysis Code	61
4.2. Time and Position Information	63
4.3. Momentum Calculation	67
4.3.1. Longitudinal Momentum	68
4.3.2. Transversal Momentum	68
4.4. Calibration Procedure	70
4.5. Experimental Resolution	75
4.5.1. Acceptance	76
4.5.2. Resolution	83
4.6. Triply-Differential Cross-Section	90

5. Results	95
5.1. Single Ionization of Rare Gas Dimers	96
5.1.1. Argon	98
5.1.2. Neon	106
5.2. Dissociative Ionization of Small Argon Clusters	119
5.2.1. Doubly-charged Final State: $\text{Ar}^+ + \text{Ar}^+$	124
5.2.2. Triply-charged Final State: $\text{Ar}^{2+} + \text{Ar}^+$	129
5.2.3. Doubly-charged Trimer Breakup: $\text{Ar}_2^+ + \text{Ar}^+$	132
6. Summary and Outlook	137
A. Atomic Units	143
B. Charge-Sensitive Amplifier	145
Bibliography	149

1. Introduction

The study of collisions is an integral part in experimental physics. Whether it is ionizing collisions, where the charge of the studied target changes, excitation or elastic collision, all have been used for decades to investigate the structure of atomic and subatomic particles. In a pioneering experiment conducted by James Franck and Gustav Ludwig Hertz in the early 20th century they found strong evidence of discrete energy levels in the atoms from mercury vapor which was used for collisions with electrons [Franck and Hertz (1914)]. The outcome was a strong support for Bohr's model of atoms which had been introduced shortly before and serves as a good example for the power of collision experiments. Nowadays, the use of enormous accelerators makes it even possible to probe the structure of hadrons, such as the proton, in collisions which lead to the discovery of the structure of subatomic particles and paved the way for modern particle physics [Bloom et al. (1969)]. Studies carried out in this manner serve as tool to acquire structural information of the target while the projectile serves in the same manner as light serves in conventional microscopy.

Another kind of collision experiment is concerned with the actual dynamics of the collision process. There, not only the outcome of the reaction is of interest but also the way this outcome is reached. Concerning electron impact, the foundations for detailed dynamical studies of ionization processes were created by Ehrhardt [Ehrhardt et al. (1969)]. In this experiment, for the first time, electrons after single ionization of helium were detected in coincidence and the angular correlation was studied. Subsequently, studies of the kind were dubbed $(e, 2e)$ -experiments – indicating the number of free electrons before and after single ionization – where the angle and energy of both electrons after the collision is recorded. As a consequence, very detailed information about the studied process in terms of the triply-differential cross-section (3DCS) is obtained.

Originally, $(e, 2e)$ studies were performed in experiments, where, on a circular path

around the target, two energy sensitive detectors were moved (e.g., [Schubert et al. (1979)]). With knowledge about the target's ionization potential, all other kinematical parameters that determine the ionization can be fixed. Hence, experiments of this kind are also called to be kinematically complete. With those machines, a single kinematical condition is probed at a time and – due to the construction of these $(e, 2e)$ spectrometers – the two electrons are detected in the same plane. Consequently, experiments of this type have been dubbed to be *coplanar*.

The employment of imaging techniques marked a significant improvement over the original design by Ehrhardt. Now, instead of movable detectors, particles are projected onto fixed detectors by electric and magnetic fields. Originally designed to improve experiments for recoil ion momentum spectroscopy in heavy ion collisions, the reaction microscope (REMI) extended the functionality to be able to also detect the created electrons [Ullrich et al. (2003)]. This setup proved to be quite versatile and is now used – apart from $(e, 2e)$ experiments [Dorn et al. (2007)], which marks another important modification – for positron impact, strong-field ionization and multi-photon ionization experiments. The essential advancement over common $(e, 2e)$ spectrometers is the fact that the detection of electrons covers the full solid angle and a large energy range, and is not bound to a single plane and a particular energy, which makes the reaction microscope tremendously more efficient.

Considering the theoretical description of a process like single ionization, one has to know that even for the most simple case, the ionization of atomic hydrogen, the problem consists of three particles and, therefore, eludes from an analytical solution. The possibilities that remain to solve such a fundamental problem are to make approximations by simplifying the situation to an effective two-body problem, or to do an exact treatment by applying numerical methods. Neither approach is perfect: the former cannot be applied to every problem due to the approximations that have to be made, which might just not be applicable, while the latter can involve an enormous amount of computer power given the actual complexity of the atom or molecule. Nowadays the situation is as such that the numerical models are applied to light targets such as helium and molecular hydrogen, consisting only of few electrons, whereas approximative methods are used when the numerical models are not usable. Among the most renowned models are the convergent close-coupling [Bray and Stelbovics (1992)] and the time-dependent close-coupling [Colgan et al. (2002)], while the approximative approaches are mostly based on the

Born approximation. Two renowned representatives being the distorted-wave Born approximation by Madison [Madison et al. (1977)] and the distorted-wave R-matrix by Bartschat and Burke [Bartschat and Burke (1987)]. The theoretical improvement in the description of the ionization of light targets has been substantial in recent years. For helium it has been even proclaimed to be solved theoretically [Bray et al. (2010)]. Concerning more complex targets it turns out to be extremely difficult for theory to produce a consistent picture – in both shape and magnitude – due to the approximations that are necessary depending on the kinematics of the actual collision under study. Especially in the low to intermediate energy range, where complex scattering processes are to be expected, theory is most challenged. At the same time, only with the reaction microscope it was feasible for experimentalists to present three-dimensional cross-sections, which proved to be a very critical test for theory [Ren et al. (2010); Schulz et al. (2003)]. Here, even state-of-the-art theories failed to reproduce the results convincingly for all geometries. It is therefore indispensable to provide precise experimental data to test the different theoretical models and shed light on the processes involved.

To the most extent, studies in $(e, 2e)$ collisions have been performed on atoms and molecules. However, there have been experiments carried out on thin layers of solid targets (e.g., [Canney et al. (1997)]). In between these extremes of sole constituents and macroscopic matter, i.e., for clusters formed by van der Waals forces, no experiments have been reported so far. On the other hand, fragmentation studies of rare gas clusters induced by electron impact have been a long standing field [Buck and Meyer (1986)]. Experiments of this type are exclusively concerned with the ionic size after the ionization of the parent cluster and generally performed with a constant projectile energy. Neither the momenta of the electrons nor of the ions are detected.

On the other hand, clusters, especially dimers, are renowned for decay processes enabled by electron correlation. Among those, one of the most prominent ones is Interatomic Coulombic Decay, where an inner-shell vacancy in one constituent decays by transferring the transition energy to a neighbor, leading to Coulomb explosion of the, in this case, dimer [Cederbaum et al. (1997)]. This turns out to be an extremely efficient decay channel and has since been observed in rare gas dimers and even water clusters [Jahnke et al. (2010)]. The energy transfer of ICD can occur over extremely large distances. In the helium dimer it was found that this takes

place at internuclear separations of up to 14 Å, which is 10 times its van der Waals radius [Sisourat et al. (2010)].

The study of clusters in $(e, 2e)$ experiments can, however, give valuable insight in the ionization dynamics of objects, which can be seen as an intermediate state between single atoms and macroscopic matter. A number of interesting questions concerning rare gas clusters in collisions with electrons arise:

- is the ionization behavior similar to single atoms or closer to molecules?
- can multiple scattering at different centers occur due to the number of neighboring constituents?
- is it possible to observe interference effects from multi-center scattering?
- does for dissociative ionization the spacial alignment hold information about the underlying mechanism?
- can decay mechanisms such as ICD or radiative charge transfer (RCT) be observed?

From a historical standpoint, the lack of experimental data is partly owed to the fact that a cluster target needs an additional, special preparation. Furthermore, since it turns out to be extremely challenging to provide sufficiently dense size-selected cluster targets, with mixed-size targets it is essential to detect the created ion in coincidence with the electron in order to confidently distinguish the target. Both prerequisites are not met by spectrometers of the type used by Ehrhardt but are natural to reaction microscopes.

The following work is dedicated to provide the first kinematically complete electron impact ionization studies of small rare gas cluster. In the course of experiments, two different target species were studied: argon clusters at a projectile energy of 100 eV and neon dimers at 61 eV. In the experiment at low to intermediate energy with argon one major focus was the change in ionization dynamics with varying size of the target, whereas the objective of the low energy experiment with neon dimers was a thorough investigation of the 3DCS. Both experiments are compared their respective atomic data, which was obtained in the same experimental run.

In a second step, a fragmentation experiment was performed with argon dimers at 120 eV projectile energy. Only events were considered, where the two charged

ions emerged after the ionization in coincidence with an electron. Here, different multi-ionization channels are studied. The fragmentation process gives access to the spatial alignment of the dimers with respect to the projectile direction, while the energy of the Coulomb explosion gives insight into the dynamics of the breakup.

In the subsequent chapter an outline of the basic concepts in electron impact ionization and their theoretical description will be given. Afterwards, the target species – van der Waals clusters – will be introduced. Focusing on their characteristic nature, dedicated decay mechanisms for this species, such as ICD, will be discussed. In a next step, the experimental technique for this course of experiments will be explained in detail (chapter 3). This will include the different components of the setup as well as the analysis of the recorded data, which is an integral part of the used technique (chapter 4). Additionally, the performance of the experiment under the chosen settings will be quantified. Finally, the results that were obtained for the experiments outlined above will be presented and discussed (chapter 5).

2. Brief Introduction to Electron Impact Ionization

In the following chapter the theoretical foundation of the experimental work will be outlined. Starting with an overview of the experimental technique, the important quantities and the geometry, the general idea of $(e, 2e)$ experiments will be introduced. Followed by a brief explanation of the theoretical approaches and their applications relevant to this work, information about the targets of interest – single atoms that are bound together to molecules solely by van der Waals forces – will be presented. Therein, particular emphasis is placed on fragmentation studies following charged particle impact and the resulting abundances of specific masses. Furthermore, processes characteristic to this target species – most prominently the Interatomic Coulombic Decay – will be introduced briefly.

2.1. An Introduction to $(e, 2e)$ Experiments

The goal of electron impact single ionization or $(e, 2e)$ experiments is to gain insight into the dynamics of such a process. In fact, it is synonymous for a series of experiments where the kinematics have been fully determined and are, hence, called *kinematically complete*. The fundamental reaction of interest is



an electron e^- interacts with a target A , which is at rest, and the positively charged target and two electrons emerge. The energies and momenta are such that

$$\underbrace{(\vec{p}_0, E_0)}_{\text{projectile}} + A \rightarrow \underbrace{(\vec{p}_i, E_i)}_{\text{residual ion}} + \underbrace{(\vec{p}_{e1}, E_{e1}) + (\vec{p}_{e2}, E_{e2})}_{\text{final state electrons}} . \quad (2.2)$$

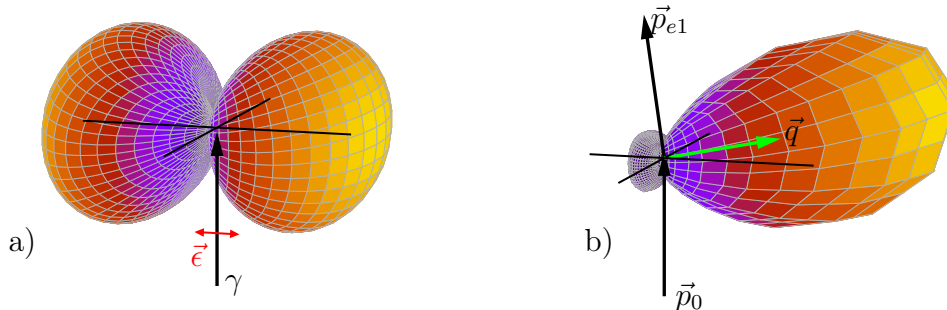


Figure 2.1.: Angular distribution of ejected electrons for: (a) photoionization and (b) electron impact ionization of helium. The propagation direction of the laser field is denoted by γ and its polarization by $\vec{\epsilon}$, while the projectile electron is denoted by \vec{p}_0 , the scattered projectile and the momentum transfer by \vec{p}_{e1} and \vec{q} , respectively.

For a given projectile energy E_0 , to release a bound electron to the continuum, the ionization potential V_{IP} has to be exceeded and the excess energy $E_0 - V_{\text{IP}}$ can, in principle, be shared arbitrarily between the electrons in the final state. The ion, emerging from the reaction can also undergo a momentum change, while its energy is negligible due to its large mass.

In the following, the magnitude of projectile energy E_0 is used to classify the basic $(e, 2e)$ reaction into different regimes. Here, three different regions will be distinguished. The high energy regime that is defined by the validity of the first Born approximation (see section 2.2), where the projectile in the initial and final state is described as a plane wave and only a single interaction with the target is considered. Next is the regime of intermediate energy. Here, higher-order interactions as well as initial and final state interactions become important. The relatively simple dynamics of the high energy regime no longer exist and theoretical descriptions have to include higher perturbation orders and/or use more realistic wave functions. Finally, the threshold region is considered briefly, which is characterized by small excess energies and strong correlation of the final state electrons.

High Projectile Energy: 1. Born Approximation

Three-dimensional electron emission patterns are shown in Figure 2.1 for an ionized electron from photoionization (panel (a)) and for electron impact ionization (panel (b)) of an s -electron. While the two processes are in fact of different nature, one can see that there are strong similarities. For the photoionization process, the angular distribution of the electrons shows the typical dipole pattern, oriented along the linear polarization $\vec{\epsilon}$ of the laser field. The $(e, 2e)$ counterpart in panel (b) has the (high energy) projectile with a momentum \vec{p}_0 coming from below, scattered under some angle with a momentum \vec{p}_{e1} in the final state. The momentum that is transferred to the target system is denoted by \vec{q} . This observable is known as the *momentum transfer*. If we consider the projectile's momentum before and after the collision, $\vec{p}_0 - \vec{p}_{e1} =: \vec{q}$ can be derived from simple momentum conservation. It is, of course, implied that the projectile can be distinguished from the ejected electron. Whether or not this can be accomplished will be discussed shortly.

As one can see from Fig. 2.1, the momentum transfer shares an analogy with the polarization vector in photoionization as it defines a symmetry axis for the ejected electrons. This is a general characteristic for processes that can be described by the first Born approximation. However, in contrast to photoionization, the emission is not equally probable for directions \vec{q} and $-\vec{q}$. Most of the electrons, for the case of electron impact ionization, are emitted in the direction of \vec{q} , which form the so-called *binary lobe*, while only a smaller part is emitted in the opposite direction. They form the *recoil lobe*. In a simple picture, the binary lobe consists of electrons that were ejected after a single interaction with the projectile, similar to a classical collision. The reason that the emission is not confined to this direction and that electrons are found which have a transversal momentum component with respect to \vec{q} is due to the initial momentum of an electron in its bound state. Depending on the angular momentum state, this can be a significant value in the order of 1 a.u. The origin of the recoil lobe, on the other hand, can be understood by the possibility of the ejected electrons to scatter on the remaining ionic potential and being emitted in the direction of $-\vec{q}$. Since now the residual ion is involved in the scattering process, it will gain momentum. In between the two lobes the emission pattern experiences a pronounced minimum, separating the two mechanisms.

One way of categorizing the dynamics involved in the ionization is by the amount

of momentum $|\vec{q}|$ that is transferred [Ehrhardt et al. (1986)]. In the extreme case of large $|\vec{q}|$, the electrons are exclusively emitted in the direction of the momentum transfer while no electrons are observed in the opposite direction. In other words, the recoil peak vanishes. Here, all the momentum is transferred to the bound electron in a single collision and neither the residual ion nor the remaining target electrons participate. To maximize the value of $|\vec{q}|$, symmetric conditions have to be chosen. These are foremost equal energies $E_{e1} = E_{e2}$ and equal scattering angles of 45° . The characteristics of the emission is now solely governed by the bound state of the emitted electron and the dynamics that are contained are well understood. Historically, this type of collision is called a *binary* collision and the corresponding regime the binary limit. This was where the term binary peak originated from. Experiments of this type are used, e.g., to probe the bound state momentum distribution of the target electrons (i.e., electron momentum spectroscopy or EMS) (e.g., [Daoud et al. (1985); Lahmam-Bennani et al. (1986)]).

In the other extreme, a vanishing $|\vec{q}|$, the emitted electrons share the same symmetric emission pattern with respect to \vec{q} . However, in this regime, the probability for electrons to be ejected in the $-\vec{q}$ direction is identical. As a consequence, the ionization mechanism can be seen very similar to photoionization, where also essentially no momentum is transferred and the ejected electrons display a dipolar emission pattern aligned along the polarization direction. In charged particle impact this extreme is also called photo-limit to indicate that the projectile only interacts once and a single *virtual* photon is exchanged with the target electron. For adequately high projectile energies E_0 the first Born approximation can be used to link this case to photoionization (see section 2.2.1). Historically, this regime was used to obtain dipole oscillator strengths for photoionization processes (e.g., [Brion and Thomson (1984)]).

In between these extremes lies the region of intermediate momentum transfer $|\vec{q}|$. Here, the size of the recoil peak, i.e., the probability for electrons to be re-scattered depends now strongly on the actual value of the the momentum transfer. Generally, the larger $|\vec{q}|$ is, the smaller the recoil peak, since one approaches the binary limit. Reducing $|\vec{q}|$ brings the situation towards the photo-limit, hence, the recoil peak increases.

For these very high energies, much larger than the ionization potential of the target (typ. $> 20 V_{IP}$), the interaction time is very short (\lesssim fs) and the projectile

is most likely scattered to very small scattering angles θ_{e1} . Hence, the momentum transfer $|\vec{q}|$ is small. The high energy region is characterized by the validity of the first Born approximation and the implication that the ionization process is independent of the charge sign of the projectile. Consequently, the total cross-section in this region behaves identical for all projectiles (e.g., electrons, positrons and heavy ions), provided they have equal velocity and charge. In experiments for such a condition it is found that energy partitioning between the final state electrons is highly asymmetric. One electron carries almost all the excess energy, which can be identified as the scattered projectile, while the other only very little, which is the ejected electron. For the high energy projectile to transfer a significant amount of energy to the target would involve a strong interaction and an accompanying large scattering angle and high momentum transfer.

While the extreme case of a high projectile energy yields structural information about the target, the dynamics involved in the ionization process are simple and in general well understood (e.g., [Zitnik et al. (1993)]).

Intermediate Projectile Energy

By lowering the projectile energy (below $10V_{IP}$) one enters the regime of intermediate projectile energy. Still, the energy partition between the final state electrons is most likely asymmetric and the scattered projectile can be distinguished from the ejected electron. Experiments of this kind find the direction of the symmetry with respect to the direction of \vec{q} to be broken for the binary as well as for the recoil peak. The deviation from the symmetry defined in the previous cases depends strongly on the final state correlation between the electrons. Generally one can say, that the lower the projectile energy and the higher the amount of momentum transferred, the more the binary and recoil lobes will be tilted away in the backwards direction. For a better visualization, Fig. 2.2 shows the electron emission pattern in this regime schematically. The projectile with the momentum \vec{p}_0 comes from below and is scattered to an angle θ_{e1} with a momentum \vec{p}_{e1} . The resulting momentum transfer \vec{q} is indicated by the black arrow, while its symmetry axis is the dashed black line. The emission direction of the emitted electron follows the continuous black curve with respect to the origin. The symmetry axis of the binary and recoil peak, respectively, is depicted by the dashed red lines. As mentioned above, in this regime, they do

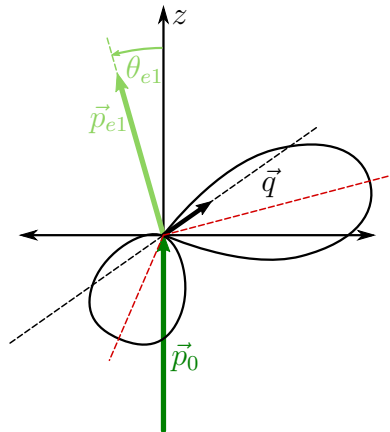


Figure 2.2.: Schematic emission pattern for intermediate energies E_0 . The projectile with a momentum \vec{p}_0 comes from below, is scattered to θ_{e1} with momentum \vec{p}_{e1} . The direction of momentum transfer \vec{q} is denoted by the black dashed line. The emitted electrons are depicted by the continuous black line. The dashed red lines depict the symmetry axis of the binary and recoil peak.

not coincide with the momentum transfer. Still, the relative size of the recoil peak depends on the magnitude of momentum that is transferred.

The natural consequence of the broken symmetry is that the first Born approximation is no longer suited to describe the ionization process [Klar et al. (1987)]. It has been shown that in order to reach agreement with the experimental data, higher-order processes in terms of perturbation have to be considered or more realistic wave functions to describe the initial and final state electrons have to be used (see section 2.2.2). In an experiment by Ehrhardt et al., 500 eV electrons were used to ionize helium and it was found that the inclusion of second-order interactions in the calculation yielded in a significant improvement in the agreement with the experimental data [Ehrhardt et al. (1982)].

Furthermore, it can be distinguished between *symmetric* and *asymmetric* final state energies. For symmetric cases, only coincident electrons are analyzed which have identical energies $E_{e1} = E_{e2}$. In literature, this case is often referred to as *equal energy sharing*. In experiments of this nature it has been shown that even for relatively simple targets, such as hydrogen and helium complex ionization mechanisms are involved than one would not expect classically or from a binary knock-out. This can be understood by the fact that for a significant energy loss of the projectile,

a strong interaction with the target and a large momentum transfer is necessary. In a classical picture, the collision needs to be close. As a result, the interaction with other target constituents besides the ejected electron are strongly increased. To reproduce data for ionization of helium and neon from 100 eV to 500 eV it was possible to use first-order interactions, but the interaction potential is modified to approximate the effect of the target electrons on the projectile [Rosel et al. (1991)]. In an asymmetric experiment by Ren et al., helium was ionized by 70.6 eV projectiles and very good agreement over a large kinematical range could be achieved by the state-of-the-art non-perturbative approaches that solve the Schrödinger equation numerically [Ren et al. (2011)].

The transition from high to intermediate energies invokes an important effect. Basically, the lower the projectile energy is, the closer the energies of final state electrons will be. Consequently, the repulsion due to their identical charge sign and the accompanying long-range Coulomb potential starts to modify the angular distribution. This is commonly referred to as *post-collision-interaction* (PCI) [Kuchiev and Sheinerman (1989)]. To visualize this effect Figure 2.3 shows one experimental and two calculated triply-differential cross-sections for the $3p$ ionization of argon at 100 eV projectile energy. The dashed arrows represent the directions of the incoming and the scattered projectile; the scattering angle θ_{e1} of the latter was fixed at 10° while the ejection energy was $E_{e2} = 15$ eV. The arrow \vec{q} depicts the corresponding direction of the momentum transfer. The red curve was calculated using the Distorted-Wave Born approach (see section 2.2.2). Based on the plane wave first Born approximation, the final state interaction of the electrons is not accounted for. Two features are apparent: most electrons are ejected in the direction of the momentum transfer \vec{q} – as explained above – they form the binary peak, indicating that the mechanism behind this emission is a binary interaction between the projectile and the target. A lesser amount is scattered in the direction of the recoil peak. Due to the wave functions not being plane waves and the energy being intermediate, the symmetry with respect to \vec{q} is broken.

The second, blue curve shows a convolution of the calculation resulting in the red curve with a factor that accounts for PCI (the so-called Macek factor [Ward and Macek (1994)]). Technical details will be explained in greater depth in section 2.2.2. Briefly, this factor was introduced to account for PCI without losing the advantage of the theory being computationally inexpensive by having to include the final state

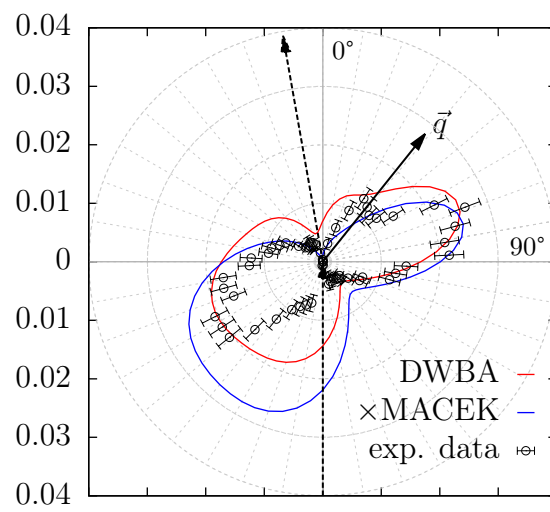


Figure 2.3.: A polar plot of the 3DCS for argon calculated in the distorted-wave Born model. The red curve represents the plain DWBA calculation while for the blue curve, this model is convoluted with the so-called Macek factor to account for PCI. The black data points are from an actual experiment. The scattering angle is $\theta_{e1} = 10^\circ$, the ejection energy $E_{e2} = 15 \text{ eV}$. The corresponding momentum transfer quantities are $\theta_q = 37^\circ$ and $|\vec{q}| = 0.6 \text{ a.u.}$

Coulomb interaction to all orders in the calculation of the final state wave function. This approach, however, has a major drawback since it destroys the absolute scale of the calculation, making it necessary to rescale the cross-section. In Fig. 2.3 both curves were normalized to their respective integrals which, in this case, have a ratio of 0.6. As a result one can compare the effect of the inclusion of PCI to this simple model. Doing so, one can see that consideration of PCI in terms of the Macek factor (blue curve) leads to a strong modification of the cross-section. The ejection of electrons in the general direction of the projectile is greatly suppressed while the binary and recoil peaks are pushed away in the backwards direction. For the exact value of scattering angle of the projectile, the cross-section goes almost down to zero. The corresponding experimental data is plotted in black. While the agreement of the recoil lobe is mediocre, one can see that the suppression in the direction of the scattered projectile is much stronger than the plain first order model predicts and that the binary peak is matched quite well by the inclusion of PCI in terms of the Macek factor. Experiments by Whelan et al. showed that in order to achieve agreement with the first-order model it had to be convoluted with this factor to reproduce final state interaction between the two electrons [Whelan et al. (1994)]. Subsequent investigations involving heavy rare gases by Rioual et al. came to a similar conclusion [Rioual et al. (1997)].

Sometimes in literature it is found that the region between the high energy and the threshold regime is – besides the intermediate region – divided further in a dedicated *low energy* regime. This distinction is made to indicate that the collision dynamics differ between the upper and the lower boundary of this region. As outlined above, at sufficiently high intermediate projectile energies, the inclusion of second-order interactions in the perturbation delivers a satisfactory description of the ionization process. By lowering the energy further, additionally, exchange-effects become increasingly important and have to be considered theoretically. These are interactions, where either a free electron is exchanged by a bound one or, simply the fact that the (scattered) projectile and the ejected electron may be exchanged for on another. As a result, the possibility for distinction between the final state electrons becomes less possible with decreasing projectile energy. In an early attempt to explicitly account for exchange in a perturbative calculation, Ray et al. found for the exemplary case of $(e, 2e)$ on atomic hydrogen at 150 eV and 250 eV that the effect is almost negligible for the higher energy [Ray and Roy (1992)]. For the lower

energy it was found that the influence of the exchange term was increasing for an increasing ejection energy E_{e2} , at a constant scattering angle θ_{e1} , and for increasing θ_{e1} for fixed E_{e2} . They find deviations in the magnitude of the binary peak of up to 16 %. To achieve satisfactory agreement with experimental data, however, PCI had to be included in the theoretical treatment.

The discussion up to now has been done without much regard to the state of the bound electron. In fact it was somewhat implied that it was in an s -state. There is, however, a difference concerning the emission direction if the valence electron is in a p -state. One can find kinematical conditions where $|\vec{p}_{e2}| = |\vec{q}|$, the absolute values of the ejected electron's momentum and the momentum transfer are chosen to be equal. This condition is also known as *Bethe-ridge*. In the case of a pure binary collision, the bound electron must have zero momentum – or $|\langle \mathbf{p} | \psi_i \rangle|^2 = 0$ – to be emitted in the direction of \vec{q} . This is possible for a s -state but not for a p -state electron. There, the momentum distribution has a node for zero momentum and a maximum for a discrete positive value. Consequently, the emission pattern experiences a pronounced suppression in the direction of \vec{q} .

Threshold Energy

At the other end of the energy scale – close to the ionization threshold – the electrons in the final state become virtually indistinguishable due to the small excess energy. Near-threshold studies have been a long standing field in electron collision experiments since the first investigations by Wannier and the law by the same name [Wannier (1953)]. Wannier found the behavior of the total single ionization cross-section with respect to the excess energy to be $\sigma_{\text{tot}} \propto E^n$ with $n = 1.127$, while the correlation between the outgoing electrons proved to be strong. Since now the ionization mechanism is a real-three body process no distinction between binary and recoil peak can be performed. Both electrons emerge exclusively back-to-back with a mutual angle $\theta_{12} = \pi$, while the projectile momentum is exclusively carried away by the recoil ion (e.g., [Williams et al. (2006)]).

Geometrical Considerations

The observable of an $(e, 2e)$ experiment is a differential cross-section (DCS). In fact it is a triply-differential cross-section (3DCS);¹ a 3-fold derivative of the total cross-section:

$$\frac{\partial^3 \sigma}{\partial \Omega_1 \partial \Omega_2 \partial E_2}, \quad (2.3)$$

where $d\Omega_i = \sin \theta_i d\theta_i d\phi_i$ denote the solid angles of the two final state electrons, respectively, and E_2 the ejected electron energy.² The geometry of a typical experiment is shown in Fig. 2.4. The projectile with a momentum \vec{p}_0 comes in from the left and interacts with the target at the origin of the coordinate system. The projectile scatters off the target with the momentum \vec{p}_{e1} , while ionizing a bound electron. This formerly bound electron has a momentum \vec{p}_{e2} . The momenta \vec{p}_0 and \vec{p}_{e1} define the blue reaction plane dubbed *scattering plane*. In common experimental setups, the two movable detectors define this plane. Since electrons are only detected in this plane, their azimuthal angle ϕ_i is fixed by the construction of the setup and the angle by which they scatter is θ_i . Within the scientific community an arrangement like this is also referred to as *coplanar*. Typically, since the azimuthal angles are already fixed, a common representation of the 3DCS is to additionally fix θ_{e1} and E_{e2} and to plot (2.3) as a function of the ejected electron's emission angle θ_{e2} . This is in stark contrast to photoionization, where the energy of the ejected electron is defined by the photon energy and the ionization potential of the target. For electron impact, significant momentum can be transferred to the target system and consequently a continuous distribution of electron energies is produced while the projectile loses energy.

The coplanar geometry shows the position, magnitude and shape of the binary and recoil peaks (cf. Fig. 2.1). This yields detailed information of the collision dynamics and allows for critical tests of theories. However, it has been shown, that higher-order contributions to ionization mechanisms can give rise to an emission of electrons outside of this plane. Experiments by Dürr et al., where electrons over the complete 4π solid angle were detected, revealed significant deviations of data for non-coplanar geometries with theory that could describe the coplanar data very

¹For the case that the studied target is spherically symmetric the term fully-differential or FDSCS applies.

²We count the solid angle element $d\Omega := \sin \theta d\theta d\phi$ as a single variable.

well [Dürr et al. (2006, 2008)]. Thus, to obtain more insight into the dynamics of different ionization mechanisms, experiments have to extend their angular range to be able to study also non-coplanar geometries (see section 4.6).

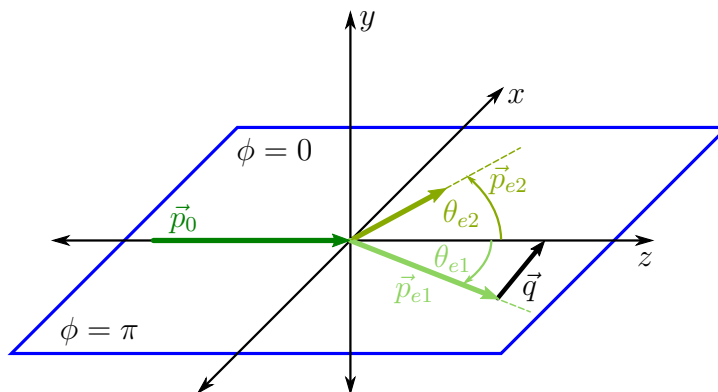


Figure 2.4.: Principle scattering geometry of an $(e, 2e)$ experiment. The blue plane – the *scattering plane* – is defined by \vec{p}_0 and \vec{p}_{e1} . The positive x direction corresponds to an azimuthal angle of $\phi = 0$, the negative x direction to $\phi = \pi$.

In a non-coplanar arrangement the ejected electron is detected explicitly in a plane that does not coincide with the scattering plane. Prominent choices are either a plane which consists of $\phi_{e2} = \{\frac{\pi}{2}, \frac{3}{2}\pi\}$ (i.e. the yz -plane in Fig. 2.4) or one that consists of $\theta_{e2} = \pi$ (i.e. the xy -plane). Both planes have in common that they are more sensitive to contribution of additional – higher-order – scattering processes. This is apparent in the fact that the 1st Born approximation is no longer appropriate to describe the behavior of the 3DCS for low to intermediate projectile energies (see e.g. [Furtado and O’Mahony (1989); Zhang et al. (1990)]). Especially for the emission of both electrons to the xy -plane, i.e., $\theta_{e1} = \theta_{e2} = 90^\circ$, a series of interactions are required that depend strongly on the ionic potential of the target [Al-Hagan et al. (2009)].

2.2. Theoretical Models in $(e, 2e)$ Reactions

Even for the simplest target – the hydrogen atom – theory has to face the fact that single ionization by electron impact is already a three-body problem and, hence, eludes an analytical solution. As a result, in order to predict cross-sections in par-

ticular for more complicated systems, theory has to rely heavily on approximations. Several ideas have emerged on how to get a grip on these problems. They can be divided in approximate perturbative and non-perturbative numerical models.³ Even if, for the latter models, it is in principle possible to acquire an exact numerical solution for the ionization of atomic hydrogen, these methods need to approximate more complicated systems e.g. by “freezing” all but one active electrons. To name two important representatives, on is the Convergent-Close-Coupling [Bray (1994); Bray and Stelbovics (1992)], the other the Time-Dependent-Close-Coupling [Colgan et al. (2002)]. Both of which have not yet been extended to heavy rare gases due to their complexity and accompanying exponential increase in computer power needed to solve the Schrödinger equation.

The perturbative approaches revolve exclusively around the Born approximation, which treats the projectile/target interaction as small and the scattering process is split in discrete orders of the interaction potential.

Generally, in ionizing collisions the quantum mechanical system is described by its Hamiltonian \hat{H} . Since here, the situation before and after the collision, i.e., the initial and final states, is different, the complete Hamiltonian can be presented as such

$$\hat{H} = \hat{H}^i + \hat{V}^i = \hat{H}^f + \hat{V}^f . \quad (2.4)$$

The indices denote initial state i to a final state f for the transition $i \rightarrow f$, while \hat{H}^{if} is the Hamiltonian of the non-interaction system, \hat{V}^{if} the interaction. The solution is quite generally given by the time-dependent Schrödinger equation

$$i\hbar \frac{\partial}{\partial t} |\Psi(t)\rangle = \hat{H} |\Psi(t)\rangle . \quad (2.5)$$

Since the actual process develops in time, starting at $t = -\infty$ to $t = +\infty$, it is important to define the asymptotic states of the system as

$$|\Psi_{\pm}^{if}\rangle \xrightarrow{t \rightarrow \mp\infty} |\Phi^{if}\rangle . \quad (2.6)$$

Theses states $|\Phi^{if}\rangle$ represent the initial and final system at the temporal extremes.

In the following, only those approaches shall be introduced that apply to this

³The qualifier “approximate” has been chosen to indicate that the numerical methods can in principle be exact solutions of the Schrödinger equation.

work.⁴

2.2.1. The Lippman-Schwinger Equation

In a very general way, to solve a problem like charged particle impact ionization – or in a more general way the transition from an initial to a final state – a solution of the Schrödinger equation

$$(\hat{H} - E) |\Psi\rangle = 0 \quad (2.7)$$

has to be found. Here, $\hat{H} := \hat{H}_0 + \hat{V}$ is the complete Hamiltonian of the system, E are the energy eigenvalues and $|\Phi\rangle$ are the states of the Hamiltonian \hat{H}_0 . In the simplest case, \hat{H}_0 describes the free particle. For (2.7) the time-independent Schrödinger equation was used to simplify the problem. The same formal solution can also be found with a time-dependent approach (e.g., [Sakurai (1994)], pp. 424). A solution of (2.7) can easily be obtained by

$$|\Psi_{\pm}\rangle = |\Phi\rangle + \hat{G}_{\pm} \hat{V} |\Psi_{\pm}\rangle . \quad (2.8)$$

The subscript \pm denotes the asymptotic behavior of the wave function as outgoing or incoming, respectively, while $|\Phi\rangle$ is a plane wave and the solution of the free particle's Hamiltonian as introduced above. The operator \hat{G}_{\pm} is known as the *Green* operator which is defined by a inverse differential operator in the asymptotic limit

$$\hat{G}_{\pm} = \lim_{\epsilon \rightarrow 0} \frac{1}{E - \hat{H}_0 \pm i\epsilon} , \quad (2.9)$$

where ϵ has a small, positive value. The expression (2.8) is also known as the *Lippman-Schwinger* equation. The evaluation for a local potential \hat{V} at large distances, gives the well-known solution for $|\Psi_{+}\rangle$ ($|\Psi_{-}\rangle$) as a superposition of a plane wave and an outgoing (incoming) spherical wave.

In order to calculate the cross-section for a scattering event, one has to find a solution for the T -matrix element (transition matrix) for the transition $i \rightarrow f$

$$T^{fi} := \langle \Psi^f | \hat{T} | \Psi^i \rangle , \quad (2.10)$$

⁴For a comprehensive introduction to this subject see e.g. [Chaudhry et al. (2011); McCarthy and Weigold (1995)].

which is directly connected with the scattering amplitude f^{fi} . Still, a direct solution of (2.8) cannot generally be given, which is due to the fact that $|\Psi_{\pm}\rangle$ is unknown. Therefore, one of the earliest approaches to was to use (2.8) to expand the T -matrix element for a small potential \hat{V} , which gives the *Born*-series:

$$\langle \Psi^{\text{f}} | \hat{T} | \Psi^{\text{i}} \rangle = \langle \Phi^{\text{f}} | \hat{V} + \hat{V} \hat{G}_0 \hat{V} + \hat{V} \hat{G}_0 \hat{V} \hat{G}_0 \hat{V} + \dots | \Phi^{\text{i}} \rangle . \quad (2.11)$$

First Born Approximation

Of course, one could think of a special expression for the system's Hamiltonian, where it is partitioned into a the unperturbed systems Hamiltonian \hat{H}_0 and a (small) perturbation \hat{V} . Both are possible to be described *prior* or *post* collision, such that

$$\hat{H} = \hat{H}_0^{\text{i}} + \hat{V}^{\text{i}} = \hat{H}_0^{\text{f}} + \hat{V}^{\text{f}} . \quad (2.12)$$

Additionally, we define the wave functions of the unperturbed system as follows:

$$\begin{aligned} (\hat{H}_0^{\text{i}} - i \frac{\partial}{\partial t}) | \Phi^{\text{i}}(\vec{r}, t) \rangle &= 0 \\ (\hat{H}_0^{\text{f}} - i \frac{\partial}{\partial t}) | \Phi^{\text{f}}(\vec{r}, t) \rangle &= 0 \end{aligned} \quad (2.13)$$

The previous expansion (2.11) implies that the interaction potential \hat{V} is small compared to the projectile energy. Secondly, one has to break the (infinite) series at some point to acquire a reasonable result.⁵ Experience shows that the second term can be calculated – although with a significantly higher effort – while all higher terms are basically not sensibly calculable. This is already a prototypical example for a perturbative approach to find a transition-matrix element. Per definition it holds only for intermediate to high energy collisions while at the same time higher-order contributions – which e.g. are necessary for emission to special experimental geometries (see section 2.1) – are hardly accessible. In detail it was found that for doubly-differential cross-sections the first Born approximation is unreliable below 200 eV and above 2 keV [Bell and Kingston (1975)]. The disagreement at high energies is, however, restricted to slow electrons emitted in the forward direction and fast electrons in the backwards direction, i.e., in very close collision with strong projectile-

⁵Especially for $(e, 2e)$ reactions it was shown that the Born series is divergent [Stelbovics (1990)].

target interaction.

In order to satisfy completeness of the introduced concept so far, we define the first-order Born amplitude $T_{(1)}^{\text{fi}}$ by truncating (2.11) after the first term. For the most general case of a N -electron system, we can express the interaction operator as

$$\hat{V} = -\frac{Z_p Z_t}{R} + \sum_{j=1}^N \frac{Z_p^2}{|\vec{r}_j - \vec{R}|}. \quad (2.14)$$

The subscripts p,t denote the *projectile* and *target*, respectively. The vectorial quantities \vec{R} and \vec{r}_j are the distances between the projectile and the target and the nucleus and the target electrons of an N -electron system, respectively. This leads to an expression for the first Born approximation with a scattering amplitude as follows:

$$T_{(1)}^{\text{fi}} \sim \frac{Z_p}{q^2} \langle \Psi_-^{\text{f}} | \sum_{j=1}^N \exp[i\vec{q} \cdot \vec{r}_j] | \Phi^{\text{i}} \rangle. \quad (2.15)$$

Here, $\vec{q} = \vec{k}^{\text{f}} - \vec{k}^{\text{i}}$ is the momentum transfer as introduced in section 2.1. To briefly sketch the evaluation, the first term in (2.14) vanishes, while the second term gives $\sim \sum_j \exp[i\vec{q} \cdot \vec{r}_j]$. The state $|\Phi^{\text{i}}\rangle$ represents the unperturbed bound states of the target, while $\langle \Psi_-^{\text{f}} |$ are the exact continuum states. This result holds an intriguing analogy to photoionization. For vanishing momentum transfer, the exponential function can be expanded to $1 + \vec{q} \cdot \vec{r}$, which will give $\vec{q} \cdot \vec{r}$ due to the orthogonality of the states. The matrix element for the absorption of a photon consists of $\vec{\epsilon} \cdot \vec{p}$, where $\vec{\epsilon}$ is the linear polarization direction. Consequently, electron collisions which meet the requirement of vanishing momentum transfer, which is to be found in the high energy regime (cf. section 2.1), can be interpreted by the exchange of a virtual photon.

Depending on the representation of the wave functions and the exploitation of the symmetric properties of the actual problem one can state that for a simple ionization with cylindrical symmetry the scattering amplitude is directly connected to the triply-differential cross-section

$$\frac{d^3\sigma}{d\Omega_{e1}d\Omega_{e2}dE_{e2}} \propto |T_{(1)}^{\text{fi}}|^2. \quad (2.16)$$

A typical property of the first order calculation is the symmetry with respect to the

momentum transfer. It can therefore be inferred that if this symmetry appears to be broken, higher-order effects participate in the scattering process. Secondly, since the cross-section is proportional to the squared absolute value of the matrix element, it is independent of the sign of the charge.

Basically, the only feasible progression is the second-order contribution, where, additionally to the initial and final state, a second interaction to an intermediate state is considered. Now, the cross-section is proportional to the squared absolute value of the sum of the two contributions and, hence, odd powers enter the calculation. Consequently, the total cross-section for different projectiles experiences a dependence on the charge sign for intermediate energies, where higher-order contributions are dominant (see above).

2.2.2. Distorted-Wave Approximation

Instead of neglecting the influence of the target potential on the projectile and the final state electrons, a significant improvement is to introduce a small *distorting* potential U_D , which describes the effect of the projectile-target interaction. It consists of a nuclear part as well as an approximate interaction between projectile and target electrons. As an effect, additional elastic scattering in the entrance and exit channels is taken into account. In this manner – especially for charged particle impact and/or ionization – the introduced potential can specifically be chosen to be the Coulomb potential.

Practically, the Hamiltonian is partitioned into a distorting channel and a residual interaction

$$\hat{H} = \hat{H}_0 + (\hat{V} - U_D).^6 \quad (2.17)$$

The first term in (2.17) consists of the distortion potential U_D plus the channel Hamiltonian, which can be expressed as $\hat{H}_0 = K_0 + \hat{H}_T + U_D$, the sum of the kinetic energy operator K_0 , the atomic (or molecular) target Hamiltonian \hat{H}_T and the distortion potential. By itself, \hat{H}_0 approximates the initial state. The second term – the *residual interaction* – is the difference of the projectile-target potential \hat{V} and U_D . By choosing the interactions appropriately – i.e. by including the Coulomb interaction in U_D – one can assume \hat{V} to be weaker than that for the plane-wave Born

⁶In similar fashion as eqn. (2.13) the Hamiltonian can be expressed in prior and post form which shall be omitted here.

approximation and, hence, to converge faster. The two Hamiltonians, introduced in (2.17) satisfy the following relations

$$\begin{aligned} (E - \hat{H}) |\Psi_f\rangle &= 0 \\ (E - \hat{H}_0) |\Phi_i\rangle &= 0. \end{aligned} \quad (2.18)$$

The distorted waves, denoted by χ , are to be chosen such that they satisfy

$$(\epsilon_i - K_0 - U_D) \chi_i = 0, \quad (2.19)$$

whereas the final state is approximated by $\Psi_f \approx \chi_p \chi_e \psi_r$, a product of the three final state particle wave functions: χ_p for the scattered projectile, χ_e for the ejected electron and ψ_r for the recoil ion. The T -matrix element can then be expressed in terms of the corresponding distorted wave states $|\chi_p\rangle$ and $|\chi_e\rangle$:

$$T_{\text{fi}}^{\text{DWBA}} = \langle \chi_p \chi_e \psi_r | \hat{V} - U_D | \psi_T \chi_i \rangle. \quad (2.20)$$

Important aspects are now that the interactions which are contained in the acquisition of the initial and final state wave functions are treated to all orders of perturbation. Only the ones contained in the operator in (2.20) are treated solely to first order. This, however, is not to be confused with the ordinary first Born approximation, where plane waves are used

The first application of the distorted-wave Born approximation (DWBA) for $(e, 2e)$ reactions was performed by Madison et al. for the single ionization of helium at projectile energies of up to 256.5 eV [Madison et al. (1977); Madison and Al-Hagan (2010)]. Already in this early calculation it was found that, while being a significant improvement over the plane-wave Born approximation, the agreement between experiment and theory was considerably worse for lower projectile energies. For the highest energy an extremely good agreement is achieved, whereas for lower energies the recoil peak seemed to be underestimated and direction of the binary peak was strongly shifted to the forward direction. Stevenson et al. performed an $(e, 2e)$ experiment on heavy noble gases such as argon which enabled access to the whole angular range in coplanar geometry [Stevenson and Lohmann (2008)]. For ejection energies between 2 eV to 5 eV they found the largest deviation between the

experimental data and the DWBA calculation in direction of the recoil peak. In addition, the data was compared to a modified distorted wave model (3DW), where – in analogy to BBK⁷ – the Coulomb interaction between the projectile and the ejected electron (i.c. PCI) is included in the final state wave function and is, hence, treated to all orders of perturbation theory. While the calculation changed the shape of the recoil peak drastically, agreement remains dissatisfactory. In fact, Prideaux et al. investigated the effects of PCI inclusion to the DWBA for argon and compared the theory to other extensions of the distorted-wave model – all of which were first order calculations – namely with the inclusion of exchange effects for projectile energies of 113.5 eV and 200 eV [Prideaux et al. (2005)]. The possible channels for exchange are on one hand between the two final state electrons or between either and a target electron. Since the latter tends to introduce distortion to the final state wave function it is often called exchange distortion. Similar problems arise for increasing ejections energies, where all flavors of the DWBA model do a reasonably good job describing the binary emission while the largest deviations arise in the direction of the recoil peak.⁸ As one would expect, however, the overall disagreement between theory and experiment is larger for the lower projectile energy.

A good deal of disagreements can be explained by the fact that the (plain) DWBA does not include an electron-electron interaction in the final state (i.e. PCI). A way to include this interaction was found in terms of the so-called Gamow factor. However, since for the DWBA a major advantage is that for the transition matrix all angular components can be solved analytically, hence, severely reducing the computation time, the inclusion of PCI is sought to be not included in the integration. Botero et al. proposed a modification of the final state Coulomb interaction where the 3DCS is expressed as

$$\frac{\partial^3 \sigma}{\partial \Omega_1 \partial \Omega_2 \partial E_2} = N_{ee} \cdot \left. \frac{\partial^3 \sigma}{\partial \Omega_1 \partial \Omega_2 \partial E_2} \right|_{\text{DWBA}}, \quad (2.21)$$

where in this case the right-hand side 3DCS is the plain DWBA cross-section and

⁷also called 3C model for the description of the final state as three Coulomb wave functions; introduced by Brauner, Briggs and Klar [Brauner et al. (1989)].

⁸It should be noted here that the experimental data had a severely confined angular range for the detection of the ejected electron, especially prohibiting access to direction of the scattered projectile.

N_{ee} is the Gamow factor [Botero and Macek (1992)]:

$$N_{ee} := \frac{\pi/k_{12}}{\exp(\pi/k_{12}) - 1}. \quad (2.22)$$

Here, $k_{12} = \mu \nu_{12}$ is product of the reduced mass μ of the final state electrons and their relative velocity ν_{12} , as introduced by Ward and Macek [Ward and Macek (1994)]. A satisfactory agreement with experimental data could be achieved even in the extreme case of the Wannier regime with impact energies smaller than 5 eV above threshold. However, the example of Stevenson et al. shows that there can be cases where only including the PCI (even to all orders) does not describe the situation accurately and leave open the possibility for either including higher-orders in the perturbation (i.e. 2nd-order contributions) or whether the situation changes if one were to account properly for exchange distortion (e.g. [Prideaux et al. (2005)]).

In that respect, another important extension to the distorted-wave method is the hybrid DWBA R-matrix (DWBA RM) approach by Bartschat and Burke [Bartschat and Burke (1987)].⁹ Here, the idea is to divide the configuration space in an internal and external volume. The border R of these two volumes is referred to as the *channel radius*. In this particular description of $(e, 2e)$ reactions, the projectile – both incoming and scattered – is described in terms of distorted-waves while the initial and final target states as well as the ejected electron is expanded in the R-matrix basis. This separation is chosen in that way to access the correlations between the ejected electron and the target final state. In particular, exchange distortion of the ejected electron is treated exactly but at the cost of neglecting Coulomb interaction between the final state electrons. It is, however, possible to introduce second-order contributions (DWB2 RM) to the interaction [Reid et al. (1998)]. This extension has been successfully applied to single ionization of heavy rare gases such as argon [Bartschat and Vorov (2005)].

2.3. Van der Waals Molecules

Apart from single atoms and molecules, which are covalent-bonded, the term *van der Waals* molecules applies to variety of small clusters that are held together by

⁹A review about the principle of R-matrix theory can be found, e.g., [Descouvemont and Baye (2010)]

the *van der Waals* force.¹⁰ In reality the term van der Waals force is applied to attractive or repulsive forces that can be of different nature. It can result from induced dipole (or multipole) interaction, from a permanent dipole (or multipole) as well as from spontaneously induced dipole interaction. While the former is called *polarization* the latter is known as *dispersion* or London force. In fact, the London force is the only reason why noble gases exist in liquid form. At the same time it presents a reasonable explanation as to why the boiling point of the elements in the 8th main group (or 18 in IUPAC) increases with the period: the attractive force increases with the number of electrons. However weak van der Waals forces may be – on a relative scale the bond strength of the London force is about $\frac{1}{1000}$ compared to a covalent bond – combined with the hydrogen bond, make up about all macroscopic matter. In the special case of noble gas molecules, such as Ar_2 , a low temperature is needed in the sense of translational and vibrational energy for them to be stable. In other words $k_{\text{B}}T$ must not exceed the binding energy of the molecule. Since the binding energy of e.g. Ar_2 is about $E_{\text{B}} = 10 \text{ meV}$, which corresponds to a temperature of $T = 11.6 \text{ K}$ which is significantly below room temperature, special measures need to be taken in order to synthesize a noble gas molecule. In the present work this was achieved by employing *supersonic expansion* of the target gas into a vacuum chamber (see section 3.3). By this technique temperatures well below 10 K are reached, producing stable van der Waals molecules of mean sizes up to 25 in case of argon. For neon, to even reach a measurable dimer count, the gas had to be cooled prior to the expansion (see 3.3).

The formation of noble gas molecules is a more or less statistical process of the expanding gas. Hence, a size or mass selected target beam is not feasible in the sense that the conditions of the expansion could be chosen to favor a particular size. As a consequence, for given experimental properties (i.e. stagnation pressure, gas temperature and nozzle diameter), the target jet consists of a distribution of sizes. Any selection in sizes to create a target of only a single size has to be performed afterwards with the consequence of further reducing the target density. Fundamental work in estimating such a size distribution has been done by Hagena [O. F. Hagena (1981, 1992)]. He found an empirical way to connect the mean size $\langle n \rangle$ of a cluster

¹⁰Named after Dutch physicist Johannes Diderik van der Waals.

with the reduced Hagena parameter Γ^* :

$$\langle n \rangle = A(\Gamma^*/1000)^\gamma . \quad (2.23)$$

The parameters A and γ have to be chosen according to the value determined for Γ^* , which by itself is a function of the stagnation pressure P_0 , the expansion temperature T_0 and the geometry of the nozzle. In the case of a radially symmetric nozzle, as used in this work, it depends foremost on its diameter d_n . An expression for Γ^* can be given as

$$\Gamma^* = (P_0 d_n^q T_0^{0.25q-2.5}) K_{\text{ch}}, \quad 0.5 < q \leq 1 . \quad (2.24)$$

For argon, the parameter $K_{\text{ch}} = 1650$ while is $q = 0.85$ [Danylchenko et al. (2008)]. A detailed selection of characteristic values for a variety of noble gases and metals can be tabulated in [O. F. Hagena (1987)]. For our experimental conditions we can estimate the mean size of clusters in the jet for Ar to be $\langle n \rangle \sim 25$. This is, however, a very rough estimate considering that the introduced formalism is usually applied to conditions of cluster sizes $\langle n \rangle > 100$. The formation of small clusters with mean sizes in order of $10^{\text{atoms}/\text{cluster}}$ is still a matter of investigation. Compared to larger clusters, it has been argued that the stability depends strongly on the exact number of constituents. Experiments for Xe found discrete sizes, which were more abundant than other, creating the term *magic numbers* that were originally assigned to number of atoms needed for the most compact arrangement [Echt et al. (1981)]. Subsequent studies, however, indicated that this behavior was not found for other atomic species, such as He or Ar, as well as problems in the experimental methods identifying the sizes [Soler et al. (1984)]. Finally, it was pointed out that the magic numbers do not reflect the stability of the neutrals but rather give insight into the fragmentation process following ionization [Foltin et al. (1991); Märk (1987); Märk et al. (1986)].

Especially the ionic abundance of dissociation products from small clusters has been investigated for decades.¹¹ Early experiments include those by Buck et al. where size selected argon cluster targets were created by elastic scattering off a crossed helium jet [Buck and Meyer (1986)]. The clusters were then dissociated by electron bombardment and the ionic size distributions were measured. The results

¹¹The term *small clusters* is used to distinguish the occurring sizes in this work from those of common cluster experiments where sizes in the order of $> 10^3 \text{ atoms}/\text{cluster}$ are studied.

are indeed interesting: the determined fragmentation probabilities f_{nk} – the probability of formation of a ionic cluster of the size k by ionization of the neutral parent cluster of size n – show that while $f_{21} = 0.4$ ($\rightarrow f_{22} = 0.6$), no trimer ion was created from ionization of neutral trimers; in other words $f_{33} = 0.0$, indicating that the trimer ion is not stable upon electron impact. On the other hand, $f_{32} = 0.7$, the majority of the ionized trimers dissociate into dimer ions rather than monomers. The latter finding is even more emphasized by including parent sizes up to $n = 6$, where almost no ion sizes larger than $k = 2$ are found. The general tendency towards fragmentation of small clusters can be understood by looking at the potential curves for Ar_2 in Fig. 2.5. The neutral dimer – with a internuclear distance of 3.8 \AA [Tao and Pan (1992); Ulrich et al. (2011)] – undergoes a vertical transition upon ionization, which is indicated by the Franck-Condon region. One can see that the only probable possibility to create the dimer ion Ar_2^+ in its ground state is in a high vibrational state close to the $\text{Ar}^+ + \text{Ar}$ dissociation limit. The corresponding vibrational energy of about 1 eV is two orders of magnitude larger than the binding energy of the neutral dimer of 10 meV . Consequently, if the ionization of a small cluster is imagined as the creation of a dimer ion, this ion can reduce its internal energy by transferring it to the cluster [Burgt and McConkey (1995); Scharf et al. (1986)]. This leads to an *evaporation* of comparatively weakly bound neutrals and a reduction in the size of the detected cluster ion.

An early attempt to describe the observed behavior of charged cluster fragmentation was given by Haberland [Haberland (1985)]. The ionization – and subsequent fragmentation – of small noble gas clusters is described as the creation of a delocalized positive charge within the cluster. This positive charge (or hole) can move from one constituent to another since the system is not in a stationary state. The predicted time-scale for the displacement of the hole is in the order of 10^{-14} s . After an total time of 10^{-12} s the hole is localized in a dimer ion. Since this dimer ion is created in high vibrational state it can be associated with the creation of an exciton state. Due to tremendously smaller internuclear distance of the de-excited dimer ion the probability of displacement of the positive charge is greatly decreased and the hole is trapped. In this respect, also the tendency for the preference of the dimer ion after fragmentation can be understood in a qualitative picture. Subsequent theoretical studies have tried to improve upon this early attempt to investigate the ionic abundance after electron impact ionization with hybrid classical/quantum mechan-

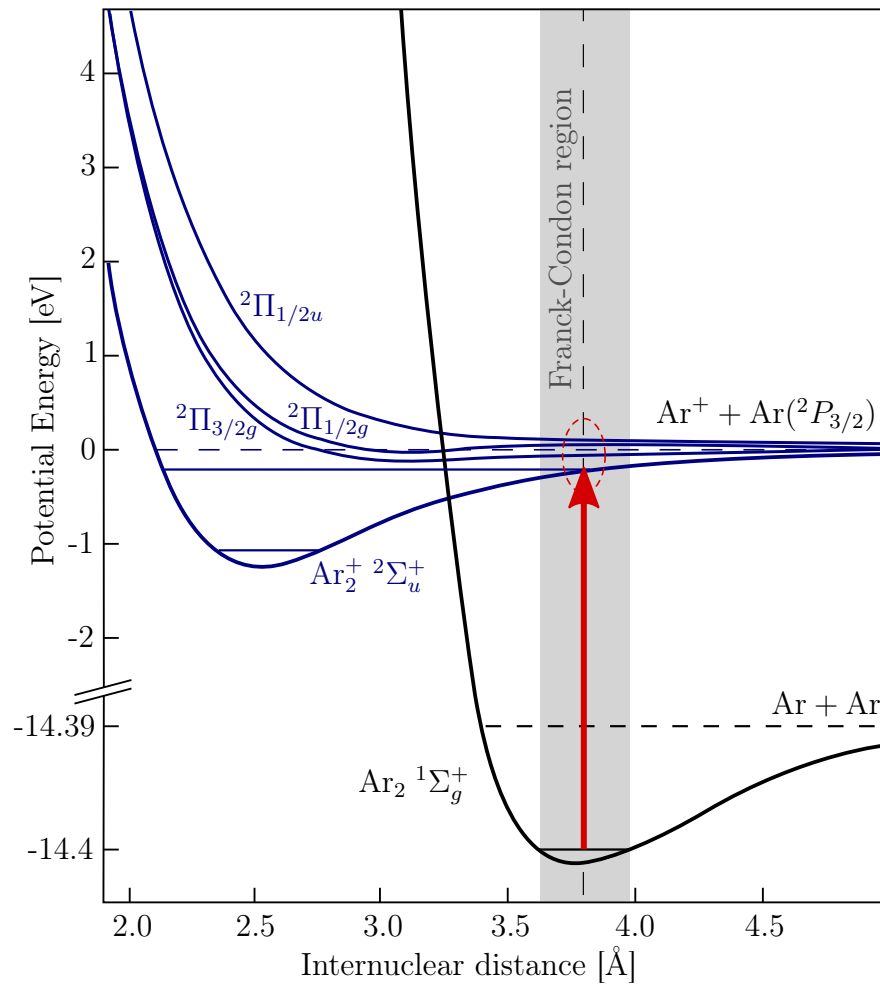


Figure 2.5.: Potential curves for Ar_2^+ . A vertical transition in the center of the gray-shaded Franck-Condon region is indicated with a red arrow. Curves are from [Wadt (1978)].

ical methods [Bastida et al. (1996)]. Bonhommeau et al. modeled the fragmentation of small argon cluster for parent sizes $n = 2$ to 11 [Bonhommeau et al. (2006)]. The calculations reveal a fragmentation probability for neutral dimers into Ar_2^+ of $f_{22} = 66\%$ while for $n = 6$ this probability has a maximum of $f_{62} = 95\%$. Additionally, $f_{i3} = 0$ for $i < 5$, stable trimer ions are created only for parent cluster sizes larger than Ar_5 . Similar studies for heavier species such as krypton and xenon clusters found strong discrepancies in terms of monomer production [Bonhommeau et al. (2007); Poterya et al. (2009)]. While the theoretical calculations for Xe_n , $n = 2 - 5$ predict – in accordance with the predictions for Ar – a preference of Xe_2^+ production with a maximum of $f_{42} = 76\%$, the experimental findings, however, measured a Xe^+ abundance of more than 90%. As possible causes for this very different behavior it has been argued, whether possible processes which can occur in the experiment might be neglected in the theoretical description. Among the issued possibilities are multiple scattering events of the outgoing electrons as well as additional excitations of valence electron or inner shell ionization as well as different dissociation mechanism such as Interatomic Coulombic Decay.

The above imposes several conditions to an experiment that have to be considered if the ionization dynamics are to be studied for specific sizes of small clusters such as dimers. Either the target itself has to be size selected or the ions which emerge from a reaction have to be detected. In this work the latter approach was chosen in order to maintain as much target density as possible. Additionally, if it proves feasible to detect the ionic fragments, a distribution of cluster sizes creates a big advantage. Then, in a single experiment under identical conditions, reactions with all sizes can be measured and compared with the same systematical error. This proves vital in the case of non-dissociative ionization of dimers, where – compared to atoms – only small differences in the cross-section are to be expected due to the very weak binding energy and the large internuclear separation.

2.3.1. Interatomic Coulombic Decay

The ionization of small clusters – as compared to the ionization of molecules – can lead to special fragmentation pathways that were described in the late 90s by Cederbaum et al. [Cederbaum et al. (1997)]. The proposed mechanism – dubbed *In-*

teratomic Coulombic Decay (ICD) – leads to very effective and ultra-fast¹² multiple ionization, which is closely related to the Auger decay in atoms [Auger (1925)]. The Auger decay is a process, where an inner-shell vacancy in an atom or molecule is filled by a transition of a bound electron from an energetically higher orbital while the excess energy is transferred to a valence electron which is released to the continuum. This can only happen, if the excess energy is sufficient to overcome the ionization potential of another bound electron. Otherwise, the energy is released in terms of an x-ray photon.

In its basic formulation, ICD is enabled by a neighboring atom where Auger decay would otherwise be energetically forbidden. The excess energy is then transferred to a valence electron of the neighboring atom by means of a virtual photon, leading to its ejection and leaving both atoms in ionized states.¹³

A qualitative picture of an ICD process can exemplarily be given for the neon dimer Ne_2 (see Fig. 2.6). Atomic neon has an electronic configuration of $[1s^2 2s^2 2p^6]$. Consequently, creating a $2s$ vacancy is not sufficient to invoke Auger decay in Ne: the energy of the $2p \rightarrow 2s$ transition with $E_{2p \rightarrow 2s}(2s^2 2p^5) = 26.91 \text{ eV}$ is too small to remove a second $2p$ valence electron, for which an energy of 40.96 eV would be needed. However, the energy could be transferred to a second, neutral neon atom by removing a $2p$ electron, for which the ionization potential is about $E(2p^{-1}) = 21.56 \text{ eV}$ [Ralchenko et al. (2011)]. A process like this will create an electron of low energy (below 5 eV in the case of Ne_2) as well as the back-to-back emission of two Coulomb-exploding neon ions. In order to prove experimentally whether ICD occurred, the coincident detection of the two neon ions and a low energetic electron has to be ensured. Furthermore, the sum kinetic energy of the ions (i.e. the *kinetic energy release* or KER) and the ICD electron energy will have to be correlated by $E_{\text{KER}} + E_{\text{ICD}} = \text{const.}$ Furthermore, since the process takes place instantaneously, the KER will have to reflect the neutral internuclear distance of the dimer according to $E_{\text{KER}} \propto 1/R_{\text{int.}}$, which corresponds to the Coulombic energy of the two exploding ions. If the KER spectrum contains features that translate to smaller internuclear distances (i.e., higher KER values), possibly other processes than ICD are involved.

As the name indicates, e.g. a dimer is treated as two independent atoms in close proximity rather than a molecule by neglecting the orbital overlap. In this respect

¹²In the order of fs

¹³Interestingly, the Auger effect was discovered by Lise Meitner and reported in 1922.

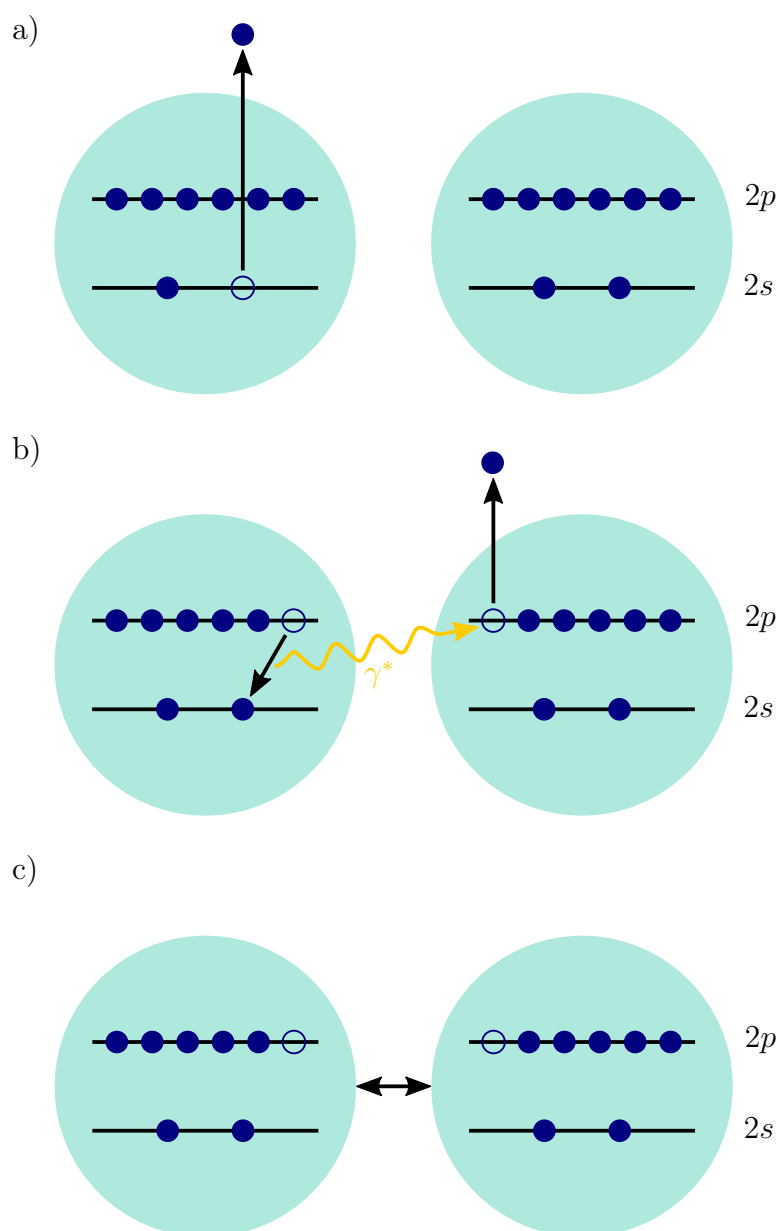


Figure 2.6.: Schematic of an ICD process in Ne₂: a) 2s ionization, b) 2p → 2s decay and 2p ionization by virtual photon, c) Coulomb explosion.

ICD is to be understood as environment-enhanced effect. However, Averbukh et al. investigated the validity of this assumption for clusters theoretically [Averbukh et al. (2004)]. Since it is experimentally extremely difficult to create a situation where two independent atoms reside at a defined distance – even more so to be able to make it repeatable up to a statistical significance – it was necessary to show whether a weakly bound van der Waals molecule was subject to ICD. They find that – however weak the orbital overlap may be – it is of essential importance to predict ICD rates. Furthermore, the simple picture of virtual photon exchange holds only for clusters with very large internuclear distances, where the Coulomb interaction is comparably weak.

The first experimental evidence for ICD was found in Ne_2 and was performed by Jahnke et al. using X-ray radiation from a synchrotron source to create the inner-shell vacancy [Jahnke et al. (2004)]. Since then, ICD has been identified in a number of targets involving a number of different configurations in most of which synchrotron radiation was used to prepare the initial core-ionization. Another particular example involves the argon dimer [Morishita et al. (2006)].¹⁴ Here, $3s$ ionization is energetically not sufficient to create a doubly ionized final state. The energy difference for the $3p \rightarrow 3s$ transition is $E_{3p \rightarrow 3s}(3s^2 3p^5) = 13.48 \text{ eV}$ while the first ionization potential is $E(3p^{-1}) = 15.76 \text{ eV}$. However, a $2p$ vacancy ($E(2p^{-1}) \sim 250 \text{ eV}$) can create a one-site doubly ionized final state via $L_{2,3}M_1M_{2,3}$ Auger decay, in which a $3s$ electron fills the vacant p -hole while emitting a valence electron. Now, the ICD channels opens up for the $3p \rightarrow 3s$ transition, creating a triply ionized final state. Energetically, the $\text{Ar}^{2+}(3s^{-1}3p^{-1})$ states are mixed via configuration interaction with $3p^{-3}3d$ states and vice versa [Hansen and Persson (1987)]. The $(3s^{-1}3p^{-1})^3P$ states for example start at 14.1 eV , while the $(3s^{-1}3p^{-1})^1P$ states, which are configuration-mixed with the $(3p^{-3}3d)^3P$, start at 17.86 eV . A summary of the possible states is collected in table 2.1. In general, it is possible to invoke ICD from a doubly charged $(3s^{-1}3p^{-1})$ state, as well as, from a $3p^3 3d$ state.

Of course, it is also possible to imagine a situation where the starting point for a doubly-charged final state is not created by an inner-shell vacancy, even if, historically, ICD studies involved such a preparation. Since excited states can also be created by a simultaneous ionization/excitation or *shake-up* and it has been specu-

¹⁴Other examples of ICD following Auger decay can be found e.g. [Demekhin et al. (2008, 2009); Liu et al. (2007); Sakai et al. (2011)]

configuration	term	IP [eV]	mixing
$(3s3p^5$	3P	14.109465	76 % $3s^23p^3(^2D)3d$
$3s3p^5$	1P	17.856498	43 % $3s^23p^3(^2D)3d$
$3s^23p^3(^2D)3d$	3P	26.526638	60 % $3s3p^5$
$3s^23p^3(^2D)3d$	1P	27.265174	48 % $3s3p^5$

Table 2.1.: States of Ar^{2+*} that participate in the ICD process to create a triply-charged final state. The ionization potential is given with respect to the $(3p^{-2})$ ground state [Saloman (2010)].

lated whether they are able to invoke ICD and couple to the doubly-charged final state. Evidence for such a process was found by Lablanquie et al. for the case of the argon dimer [Lablanquie et al. (2007)]. Here, the process evolves via an excited singly-ionized state and leads to a doubly-charged final state. Figure 2.7 shows the corresponding potential curves, in particular the repulsive $\text{Ar}^+ + \text{Ar}^+$ state that coincides with the Franck-Condon region of the neutral argon dimer ground state at ~ 35 eV.

In the wake of ICD there is another process which can lead to Coulomb explosion. There, the energy is not transferred by a virtual photon but a valence electron of the neutral constituent is removed and transferred to the other, doubly-charged constituent while the excess energy is released by a (real) photon. Consequently, this process is known as Radiative Charge Transfer (RCT) [Johnsen and Biondi (1978)]. This process depends strongly on the generally long lifetime of the initial state and in turn the, e.g., dimer ion can contract to a smaller internuclear distance. This results in a higher KER as compared to ICD, which makes both processes distinguishable in an experiment. A schematic of such a process is depicted in Fig. 2.8 for double ionization of the argon dimer. After a one-site double ionization to $\text{Ar}^{2+}(3p^{-2})$, the ion contract to about 2.8 \AA and Coulomb explodes into two singly-charged argon ions.

2.3.2. Two-center Interference Model

The scattering of a charged particle with a diatomic molecule holds an interesting analogy to a fundamental principle in quantum mechanics, namely the wave-like nature of particle. Every particle can be described as a matter wave and consequently possesses a wavelength. The famous experiment conducted by Thomas Young al-

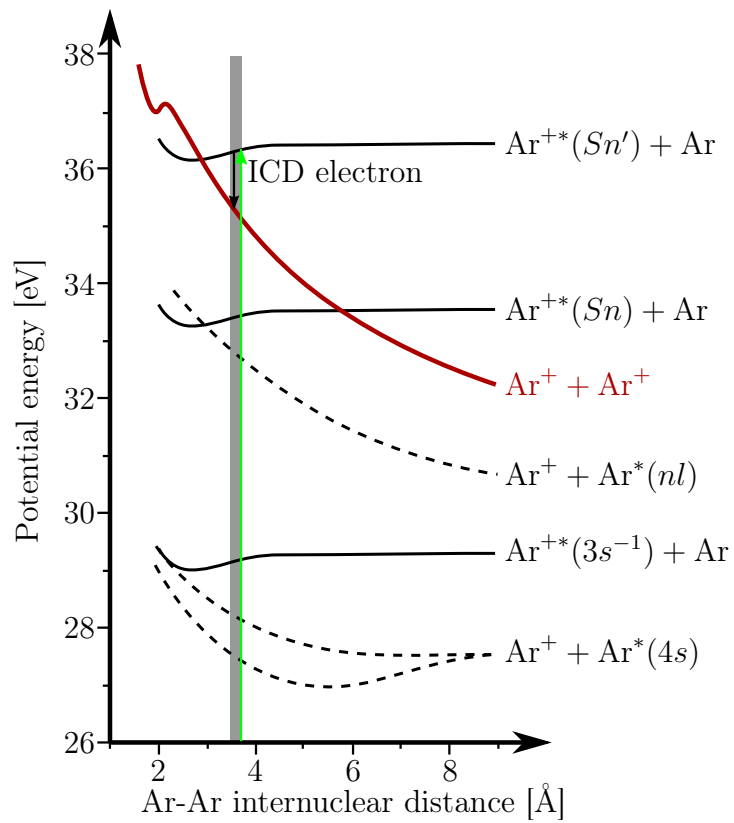


Figure 2.7.: Ar_2^{+*} potential curves (after [Lablanquie et al. (2007)]). The gray area depicts the Franck-Condon region of the Ar_2 ground state.

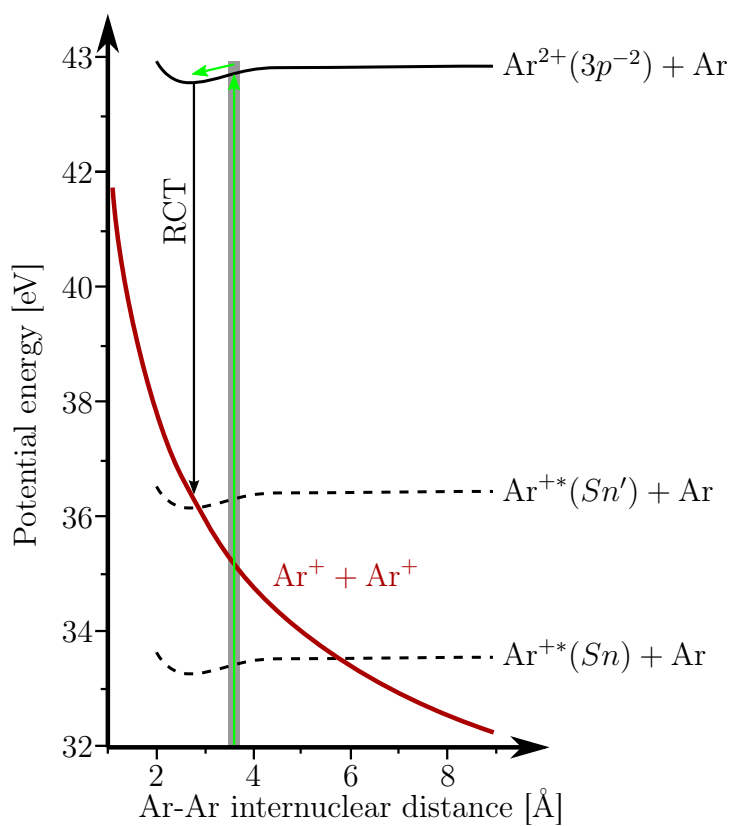


Figure 2.8.: Ar_2^{2+} potential curves. The gray area depicts the Franck-Condon region of the Ar_2 ground state. The vertical arrow marks the RCT transition.

ready in 1806, to investigate the nature of light in the dispute of whether it consists of particles (or corpuscles) or has a wave-like nature, produced convincing evidence (namely an interference pattern) that light was indeed a wave [Young (1804)]. Only in the early 20th century, with the development of quantum mechanics, it became evident that particle- or wave-like nature was actually a duality and formed one of the cornerstones of modern physics. Experiments of this nature were repeated on multiple occasions including a famous installment by Jönsson et al. studying the interference of electrons with a grating [Jönsson (1961)]. Shortly afterwards, Cohen and Fano predicted interference effects for photoionization of diatomic homo-nuclear molecules [Cohen and Fano (1966)]. A particular beautiful example of a gedanken-experiment by Feynman about a double-slit experiment, where a single electron interferes with itself was performed by Chesnel et al. using a double capture channel in a collision of an alpha-particle with H₂ [Chesnel et al. (2007)]. The neutral helium atom is created in a highly excited state which undergoes Auger decay. In the event that the Auger electron is emitted in the direction of the doubly-charged hydrogen molecule, the two protons – which are Coulomb exploding – serves as a double-slit.

One can derive the differential cross-section for elastic scattering on a two-atom system as the cross-section for scattering at one center times an interference term [Messiah (1999)]:

$$\frac{\partial \sigma_{A_2}}{\partial \Omega} = \frac{\partial \sigma_A}{\partial \Omega} \cdot [1 + \cos(\vec{q} \cdot \vec{R})]. \quad (2.25)$$

The vector \vec{R} denotes the distance between the two centers and $\vec{q} := \vec{k}_f - \vec{k}_0$ is the difference between the projectile's final state and initial state momentum. If, however, the electron scatters inelastically from either one of the scattering centers, leaving it in an excited state, the interference term vanishes, making the cross-section essentially two times the single-center cross-section. In a phenomenological picture this behavior makes perfect sense. Exciting one of the two (localized) centers is like marking one of the slits in a double-slit experiment, hence, revealing information about the pathway. Consequently, the electron (or photon) acts like a particle rather than a wave.

For an inelastic event like ion impact ionization of a diatomic molecule Stolterfoht et al. proposed a model similar to (2.25) describing the emission of an electron from

H₂ [Stolterfoht et al. (2001)]. The cross-section is then expressed as

$$\frac{\partial \sigma_{A_2}}{\partial \vec{q} \partial \Omega \partial \epsilon} = \frac{\partial \sigma_{2A}}{\partial \vec{q} \partial \Omega \partial \epsilon} \cdot [1 + \cos(\vec{p} \cdot \vec{R})], \quad (2.26)$$

where \vec{q} is the momentum transfer and ϵ the ejection energy. The interference term consists of the product of the internuclear distance vector \vec{R} and $\vec{p} = \vec{k}_f - \vec{q}$, the difference between the final state electron momentum and the momentum transfer. If one has no possibility of knowing the alignment of the molecule, an integration over all angular components of \vec{R} then delivers

$$\frac{\partial \sigma_{A_2}}{\partial \vec{q} \partial \Omega \partial \epsilon} = \frac{\partial \sigma_{2A}}{\partial \vec{q} \partial \Omega \partial \epsilon} \cdot \left[1 + \frac{\sin(pd)}{pd} \right]. \quad (2.27)$$

Stia et al. used this approach to model the $(e, 2e)$ cross-section for H₂ with 4 keV projectiles, which – at the time – could not be compared to experimental data [Stia et al. (2003)]. However, Senftleben et al. accomplished in performing such an experiment at 200 eV impact energy, where five fold differential cross-sections could be measured [Senftleben et al. (2010,2010)]. The molecular alignment was extracted by invoking the dissociation of the hydrogen molecule in a transition to the vibrational continuum of the ionic ground state. The results reveal a reversed dependence of the cross-section on the alignment as predicted by the theoretical model. It should, however, be noted that the original assumption of two independent scattering centers are not well reproduced by a small molecule such as H₂.

In an experiment by Hargreaves et al., studying $(e, 2e)$ reactions with randomly aligned N₂ at a projectile energy of 150 eV, the interference factor (2.27) was applied to an atomic first-order calculation and compared to an improved molecular calculation (see section 2.2.2) [Hargreaves et al. (2009)]. Here, a suppression of the recoil peak of roughly 50% with respect to the binary maximum is observed that is partly matched in intensity by the interference factor. Due to a reduced angular acceptance for the ejected electron, only few data points agree with theory while a steep decrease towards the acceptance boundaries is observed. Hence, the shape of the data in the recoil peak cannot be compared to the calculation and leaves the intensity as the only indicator.

In Fig. 2.9 the interference term from (2.27) is plotted for argon dimers with an internuclear distance of $R = 3.8 \text{ \AA}$ and a projectile energy of $E_0 = 100 \text{ eV}$ in

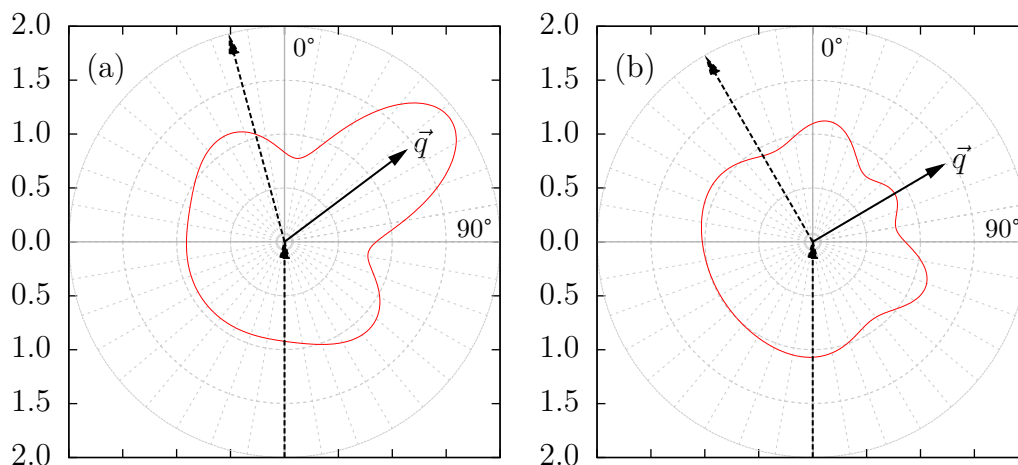


Figure 2.9.: Interference factor from (2.27) for randomly aligned argon dimers with $R = 3.8 \text{ \AA}$ and a projectile energy of $E_0 = 100 \text{ eV}$. The scattering angle is $\theta_{e1} = 15^\circ$ and the ejection energy is $E_{e2} = 10 \text{ eV}$ for panel (a). Panel (b) shows the situation for $\theta_{e1} = 30^\circ$ and $E_{e2} = 10 \text{ eV}$.

a coplanar arrangement. For the first case in Fig. 2.9(a) the scattering angle is $\theta_{e1} = 15^\circ$ and the ejection energy $E_{e2} = 10 \text{ eV}$. Here, a strong enhancement of almost a factor of 2 is observed in the direction of \vec{q} , whereas for the remainder of the angular range the interference term gives values close to 1. For the same ejection energy but double the scattering angle, Fig. 2.9(b) shows a similar shape and magnitude for the most part. The direction of the momentum transfer, however, is slightly suppressed. In general, the distribution is symmetric with respect to \vec{q} and has by far the largest effect in this very direction.

Since the vector $\vec{p} = \vec{k}_f - \vec{q}$ is not bound to a coplanar geometry – i.e., \vec{q} is by definition not dependent on ϕ , \vec{k}_f on the other hand is – one can plot the three-dimensional interference factor as a function of polar and azimuthal angle $I := I(\theta, \phi)$. Fig. 2.10 shows these distributions for neon dimers with an internuclear separation of 3.1 \AA and a projectile energy of $E_0 = 61 \text{ eV}$. The kinematical parameters are $\theta_{e1} = 30^\circ$ and $E_{e2} = 5 \text{ eV}$ for Fig. 2.10(a), while for Fig. 2.10(b) $\theta_{e1} = 25^\circ$ and $E_{e2} = 10 \text{ eV}$. Apparently, the interference factor is radially symmetric with respect to the momentum transfer.

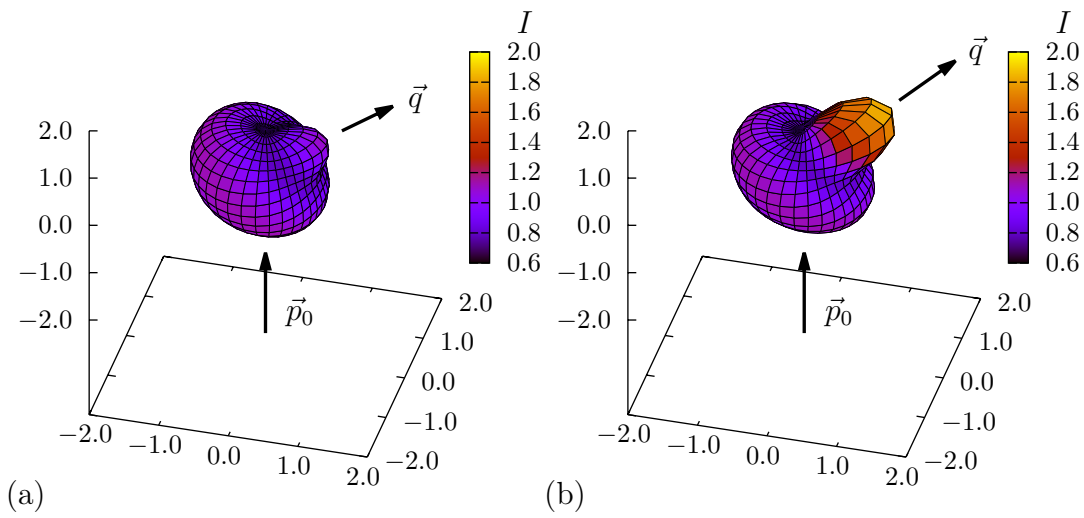


Figure 2.10.: Interference factor from (2.27) in 3D for randomly aligned neon dimers with $R = 3.1 \text{ \AA}$ and a projectile energy of $E_0 = 61 \text{ eV}$. The projectile comes from below, \vec{p}_0 , and is scattered to $\theta_{e1} = 30^\circ$. The ejection energy is $E_{e2} = 5 \text{ eV}$ for panel (a). Panel (b) shows the situation for $\theta_{e1} = 25^\circ$ and $E_{e2} = 10 \text{ eV}$. The resulting momentum transfer is denoted by \vec{q} .

3. The Reaction Microscope

The experimental results have been acquired employing a technique commonly known as a reaction microscope (REMI). A thorough overview of its first use and later adoptions can be found here [Duerr (2006); Ullrich et al. (2003)]. The setup, which was originally designed for recoil-ion-momentum-spectroscopy, underwent a number of important modifications to adapt it to experiments involving electron-impact-ionization. This advanced version of the REMI is now capable of performing ordinary ($e, 2e$)-experiments on atomic targets as well as experiments involving clusters and dissociation of molecules.

Put simply, an electron beam is crossed with a target beam inside a vacuum and by means of homogeneous electric and magnetic fields the charged fragments emerging from the collision are imaged onto two position-sensitive detectors. Hence, no distinction on the scattering geometry, detection angles or energies is performed during data taking, making it extremely efficient. The collected events have to be decoded, calibrated and finally the momenta of all detected fragments can be calculated and analyzed.

3.1. Spectrometer

In Fig. 3.1 an overview of the working principle of the REMI is shown. In contrast to conventional ($e, 2e$) spectrometers the detectors have fixed positions while the particles are imaged onto them by a homogeneous electric field \vec{E} . The actual cross-section is then derived during offline analysis.

The individual components of the experiment are from left to right: the electron gun (see section 3.4), the ion detector, the electric field region and the electron detector (see section 3.2). Electron and ion detector are used here synonymous for negative and positive charge detectors which is in principle decided by aligning the electric field parallel or anti-parallel to the spectrometer axis. The spectrometer

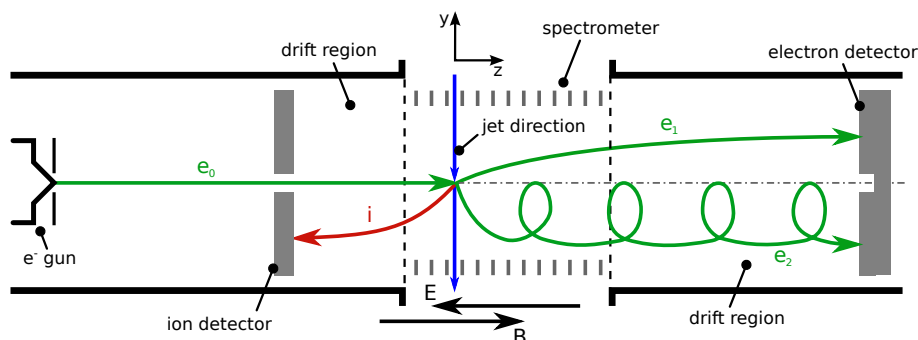


Figure 3.1.: Schematic of the spectrometer. The green arrows mark the electrons, the red arrow the ion and the blue arrow depicts the direction of the expanding neutral target.

itself consists of a field region and two adjacent field-free or drift regions on either side. The connection between field and field-free region consists of high transmission grids to create sharp boundaries and prevent field-bending at the edges of the acceleration stage. Unlike previous arrangements (e.g. [Pflüger (2008)]) the distances for acceleration and drift were chosen to be asymmetric during the course of these measurements, effectively shortening the clearance of the ion detector with respect to the interaction region. However, the *time-focusing* condition was still satisfied. Briefly, the time-focusing condition is satisfied for a relation between drift and acceleration length of $2a = d$. This configuration decouples the time-of-flight (TOF) of the particle from the actual starting point within the jet.¹ The electric field is created by an array of equidistant plates at the ends of which a voltage is applied. The individual plates are connected to each other by resistors creating a voltage gradient from one end of the acceleration stage to the other. Two of these array are placed across from one another with the spectrometer axis in the center. This arrangement creates a homogeneous electric field in the center. Typical values for the electric field range from 1 V/cm to 3 V/cm in anti-parallel orientation (i.e. $-z$). Acceleration length and drift length for the electrons were $a_e = 11 \text{ cm}$ and $d_e = 22 \text{ cm}$, respectively. For the ion the shortened dimensions were $a_i = 4 \text{ cm}$ and $d_i = 8 \text{ cm}$. While an arrangement like this is sufficient for ion detection, electrons have a much higher velocity which limits the solid angle were detection is still possi-

¹Detailed information on the time-focusing condition of this experiment can be found in [Pflüger (2008)], pp. 71-73.

ble. To restrain the radial extension with respect to the active detector area, an additional homogeneous magnetic field \vec{B} is needed. It forces electrons with a large transversal momentum onto a helicoid trajectory. This is achieved by two coils in Helmholtz configuration. Due to the rather large distance of the electron detector from the center of the spectrometer, the coils need a diameter of about 2 m to ensure a sufficient extension of the homogeneous part of the field. Common values for the magnetic field are in the order of 10 Gs. With above given values the addition of the \vec{B} -field increases the radial acceptance of the spectrometer to ≤ 35 eV for electrons.

3.2. Position Sensitive Detectors

Since the measurement procedure relies on single-shot event based data acquisition, efficient detection of the charged particles is essential. This has to be achieved with a high resolution in both time and position for a – in principle – varying number of particles. To achieve this task, what is called detector consists of different elements, each for certain purposes. First and foremost, the single particle charge is too small to be detected with a satisfying signal-to-noise ratio and consequently has to be amplified. Secondly, the TOF of each particle has to be determined which requires a fast signal. Typical TOFs for electrons are in 100 ns range in which two particles have to be distinguished. All these tasks can be performed by a *microchannel plate* (MCP) (section 3.2.1). To acquire position information a position-sensitive anode is used. According to the special demands of detection (e.g. short dead-time etc.), different approaches may be chosen. Here, the electron detection requires multi-hit capability in order to detect two electrons close in time which can be achieved by a *delayline anode* (section 3.2.2). Since short dead-time was no prerequisite for ion detection, a simpler position-encoding device was chosen, namely a *wedge-and-strip anode* (section 3.2.3).

Additionally, at least the electron detector needs to have a central hole to let the projectile beam pass through (see Fig. 3.1). Otherwise, the MCP would saturate and eventually break. The ions, on the other hand, gain little momentum in the collision compared to the initial momentum they gain by the supersonic expansion (see section 3.3). Consequently, a small detector placed below the spectrometer axis with respect to jet direction is sufficient. In order to increase the acceptance for the

ions, especially when it comes to dissociative ionization, where large momenta are to be expected, a detector that is radially symmetric with respect to the spectrometer axis is necessary. To let the projectile beam pass this detector needs a central hole, as well. For the electron detector – being on the far side of the experiment with respect to the electron gun – this could be overcome by having a hole in the MCP only. Compared to the amplified signal, the primary beam is hardly detectable which makes the top layer of the delayline anode the beam dump. For the ion detector, however, the hole needs to penetrate both the MCP and the position sensitive anode. This proves to be challenging for a delayline style detector since it implies gaps in the windings of the individual layers which have to be corrected during off-line analysis [Senftleben (2009)].

3.2.1. Microchannel Plate

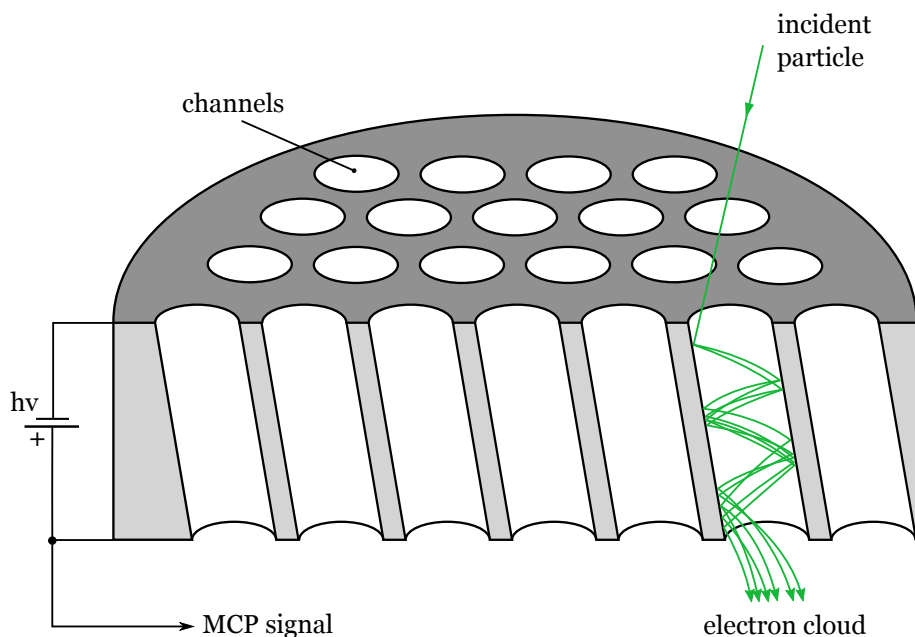


Figure 3.2.: Schematic view of a MCP. The incident particle releases an electron avalanche that is accelerated to the opposite end of the plate.

The working principle of an MCP is that of a secondary electron multiplier, which creates additional electrons each time the wall of the multiplier-tube or channel is hit. To achieve secondary emission the channel surface has to have a small work

function for electrons which is usually achieved by semiconductor materials such as gallium phosphide (GaP) or gallium arsenide phosphide (GaAsP). A high voltage (typ. 1 kV to 2 kV) across the channel accelerates the particles until at the end a cloud of electrons is emitted that can be processed further.

An MCP is now an array of such channels with diameters of $\sim 25 \mu\text{m}$ oriented in parallel made into a wafer of leaded glass as shown schematically in Fig. 3.2. To increase the total gain and improve the signal-to-noise ratio, usually a stack of two MPCs is used, where two (or more) are placed on top of each other. While a single plate has a gain of $G_s \sim 10^4$, the total gain of the stack is theoretically 10^8 . This is dependent on the voltage across the stack but to a greater extent limited by positive ion feedback. Those are ions which are created by ionization of background gas and desorption from the channel surface. In an experimental setup with two detectors opposite to each other (as depicted in Fig. 3.1), this effect proves to be highly undesirable as these ions can reach the ion detector with significant energy. However, one efficient way to greatly reduce the background created by those ions is by a *Chevron*-arrangement, where the channels of each plate in a stack have a slight angle with respect to each other. Ions that are created at the output are now prevented from reaching the channel entrance directly without hitting the channel wall.²

The detection efficiency – which is crucial to coincident experiment – is dependent on the operating voltage and the impact energy. It can reach from 50 % to 85 % for electrons. Therefore, all particles pass a short ($\sim 5 \text{ mm}$) high-field region before hitting the top layer of the stack in order to maximize the efficiency. Not only does the charge need to be amplified, a precise and fast time signal is required for the momentum calculation. A *Chevron* configuration can deliver signal pulses of 1 ns fwhm with a considerably steep rise time. The position resolution is generally limited by the spacing of the individual channels which is on the order of the channel diameter. Since the resolution of the position sensitive anodes used in this work have resolutions far larger than this, the channel spacing poses no effective limit.

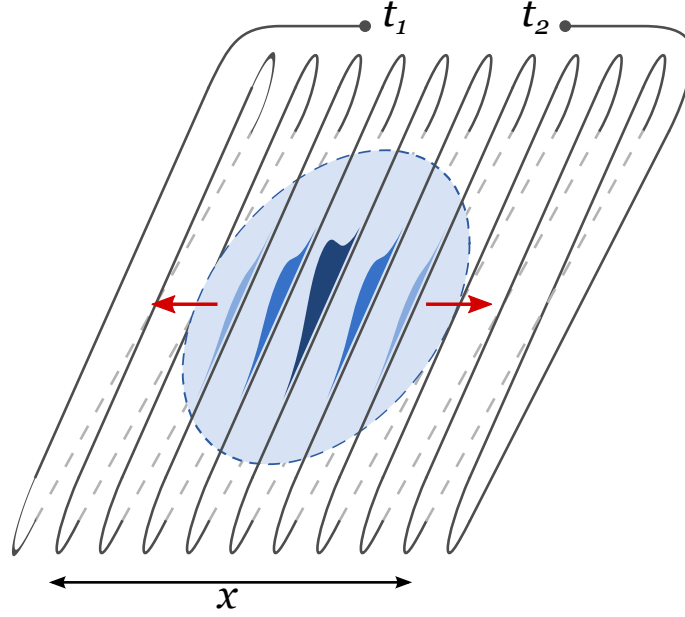


Figure 3.3.: Charge propagation in a single layer of a delayline. The detected position information is perpendicular to the wire.

3.2.2. Delayline Anode

To acquire the position of the impinging particle a position sensitive anode needs to be used which encodes the physical information into electronic signals. A delayline anode does so by propagating the charge induced by the charge cloud of the MCP along a wrapped wire of finite length. Since the charge travels along the wire towards both ends, the time difference of those signals is proportional to the center-of-mass of the incident charge distribution. A depiction of such a propagation can be seen in Fig. 3.3. To encode the 2D coordinates of the charge distribution at least two wires perpendicular to each other are needed. One direction of the coordinate can then be decoded by

$$x = \frac{v_{\text{propa.}}}{2} \cdot ((t_1 - t_0) - (t_2 - t_0)) = \frac{v_{\text{propa.}}}{2} \cdot (t_1 - t_2), \quad (3.1)$$

where $t_{1,2}$ are the respective propagation times towards the wire ends with respect to the MCP signal, $t_0 = t_1 + t_2$ is constant time sum and $v_{\text{propa.}}$ is the effective propagation velocity of the charge perpendicular to the wire in the direction of the

²An overview of MCP characteristics and production can be found e.g. [Wiza (1979)]

coordinate. Since the charge created by the MCP by no means constant for one event to another, the same goes for the charge effectively seen by the delayline. Therefore, the pulses at the wire ends need to be processed by *constant-fraction-discriminators* (CFDs). A CFD can determine the center of a pulse independent of its height. By doing so, the center of the induced charge cloud is acquired, which – if said cloud extends over several windings – decouples the actual position resolution from the physical wire spacing. The effective resolution can therefore be better than the distance of the wires.

To further increase the fidelity of encoding, each layer of the anode consists of two parallel wires – one called *signal*, the other *reference*. Both raw signals are fed to a differential amplifier, effectively canceling noise that may be induced due to the close proximity of the wires.

Another important modification to adapt this principle to the specific needs of multi-electron detection is to add redundancy to the anode, effectively lowering the dead time. The need for doing so comes from the fact that always two coincident electrons have to be detected and given the kinematics of the studied process, the time differences of arrival at the detector can go down to as little as 10 ns. Hence, a third layer is added in a way, that each 2D position component (i.e., (x, y)) can be calculated by every possible combination of two layers (i.e., (u, v) , (u, w) and (v, w)). Geometrically, the orientation of the layers has to be changed to hexagonal shape with each layer rotated by 60° to one another as depicted in Fig. 3.4, forming essentially a hexagon. Hence the name *hexanode*.

As mentioned earlier, the MCP has a hole in the center. The reason for this is that the projectile beam of electron travels towards the detector. Out of every shot of the electron gun only one coincident event at the most is recorded. Consequently, all the remaining electrons in the bunch pass the interaction volume unscattered. If they would be allowed to hit the MCP, it would immediately saturate and eventually destroy it. Additionally, a massive charge cloud would impinge on the anode wires making position detection impossible. However, to let the beam pass through the anode as well proves disadvantageous, destroying the symmetry within the layers by creating large gaps where no detection is possible. This makes it very difficult to calibrate such an arrangement (see [Senftleben (2009)]). The local change in impedance of the wire seems to introduce a large noise signal making it necessary to effectively remove an area larger than the physical extension of the gap. Therefore,

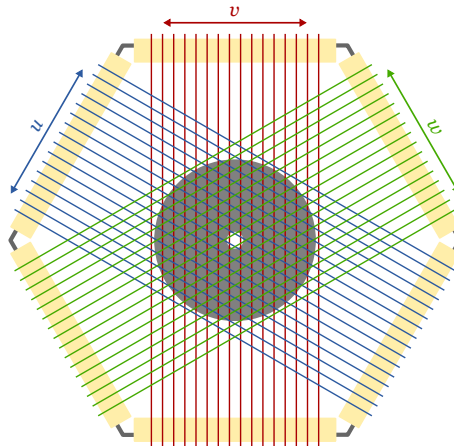


Figure 3.4.: Wire and coordinate orientation of a *hexanode*. The gray-shaded area depicts the active detection region of the MCP.

the primary beam was allowed to hit the delayline anode directly, which served as a beam dump. Since the gain of a *Chevron* arrangement is in the order of 10^6 to 10^7 , it is still 2-3 orders in magnitude larger than the charge of initial projectile pulse (i.e. $\sim 10^4$ C) and has a negligible influence on the position detection while no modification of the individual layers need to be performed.

3.2.3. Wedge-and-Strip Anode

While a delayline anode encodes the position of the arriving particle in terms of time differences in signal runtime in a wire, a *wedge-and-strip* anode has specific geometric shapes that vary in area with respect to different coordinate directions and uses the collected charge to encode the position information. A simple schematic of a circular shaped anode can be seen in Fig. 3.5. Here, the area of the electrode named *strip* varies in x -direction while the area of the *wedges* vary in y -direction. The purpose of the *meander* is to collect the remaining charge so that the total charge of the arriving could be

$$Q_{\text{tot.}} = Q_{\text{wedge}} + Q_{\text{strip}} + Q_{\text{meander}} . \quad (3.2)$$

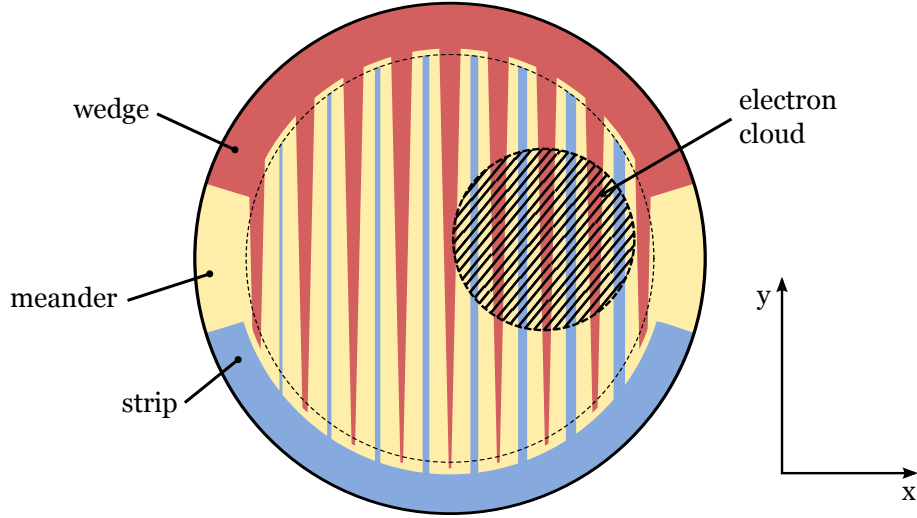


Figure 3.5.: Schematic depiction of a *wedge-and-strip* principle. The dashed circle marks the border of the active detection area.

A single coordinate is proportional to the ratio of the amount of charge collected by the respective electrode to the total charge

$$x \propto \frac{Q_{\text{strip}}}{Q_{\text{tot}}}, \quad y \propto \frac{Q_{\text{wedge}}}{Q_{\text{tot}}}. \quad (3.3)$$

A desirable working condition has the arriving charge cloud extended over several periods of the anode structure to ensure a proper proportionality over the complete active area which – in turn – gives the centroid position of the cloud and decouples the position resolution from the actual periodicity of the structure. According to Siegmund et al. the fwhm of the electron cloud arriving at the anode can be estimated to be

$$\delta w = 2.355 \left[2d \sqrt{\frac{T}{eV}} \right], \quad (3.4)$$

where T is the mean transversal energy of the electrons, d is the distance between the MCP and the anode and V the potential difference [Siegmund et al. (1986)]. With typical parameters used in the experiment, $T \sim 1 \text{ eV}$, $d = 15 \text{ mm}$ and $V = 200 \text{ V}$, a $\delta w \approx 5 \text{ mm}$ is reached which is sufficient for a step size of $\sim 1 \text{ mm}$.

The original anode used in this experiment had a diameter of 40 mm and the electrodes were made of Ge-substrate on a glass wafer with a periodicity of 1 mm. The arrangement was such that the detector was positioned below the projectile beam

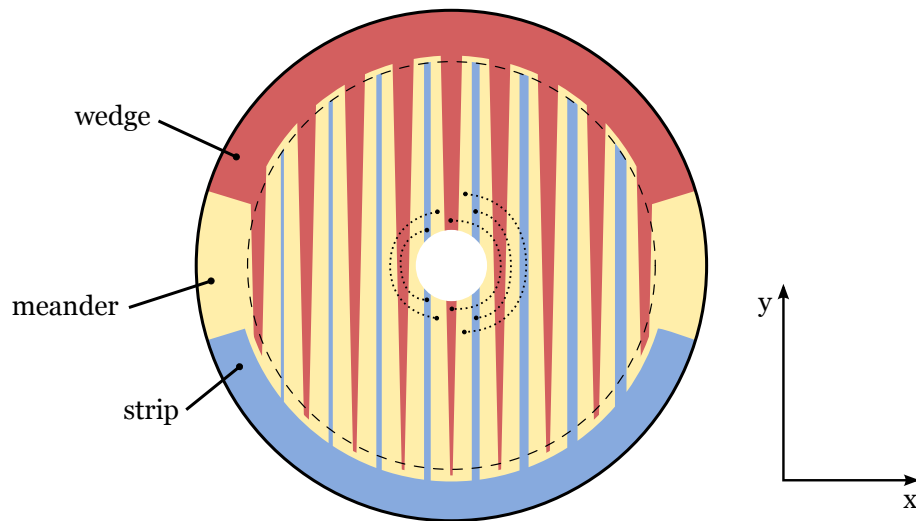


Figure 3.6.: Revised *wedge-and-strip* design with center hole. The dashed lines depict the interconnections needed to maintain the integrity of the electrode structure.

and covered only a fraction of the solid angle solely for pure ionization experiments. To overcome this limitation and extend the detection possibilities, a new anode was designed with a 80 mm active region and a central hole to let the electron beam pass through. A schematic image is shown in Fig. 3.6. This anode can be positioned with its center coinciding with the spectrometer axis, allowing an azimuthal acceptance of 2π . The anode itself was constructed from circuit board with a copper layer of 35 μm thickness. Usually, the other side of the anode is covered by a homogeneous high-resistive layer. This is the actual front side where the charge cloud coming from the MCP impinges. Due to the resistance of the layer, the charge expands slowly, increasing the actual cloud diameter and improving the coverage of anode structure. This charge signal is induced in the electrodes of the anodes and read by the electronics. The second purpose of this arrangement is that impinging electrons on the insulating material of the wafer will eventually charge it and repel subsequent electrons from the MCP. This leads to a tendency of anode structure to be visible in the position image. Since the back of the new anode is used for the connection of the electrodes which are cut by the hole (depicted by the dashed lines in Fig. 3.6), it was not available to apply a resistive layer. As a solution, a glass plate was produced on which a thin germanium layer was applied and placed on top of the anode's

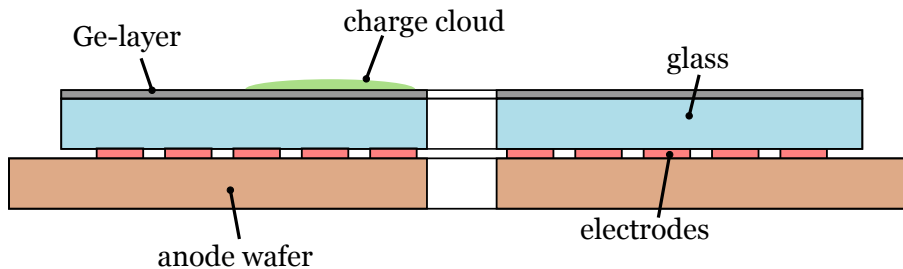


Figure 3.7.: Schematic cut showing the sandwich construction of the revised wedge-and-strip anode.

electrodes (see Fig. 3.7). This sandwich creates the revised anode.

In order to encode the position into a usable signal, it has to be processed after detection of a particle. The charge collected by the electrodes of the anode is converted to a voltage signal of proportional height by a charge-sensitive amplifier (CSA). This signal is basically a step function whose tail is decreasing depending on the decay time τ . In its most simplistic form a CSA is an inverting amplifier as shown in Fig.3.8. The decay time is given by the product of the feedback resistor R_f and the integration capacitor C_f : $\tau = C_f R_f$. Generally, the decay time limits the achievable detection frequency or, in other words, increases the dead-time of the detector. In this arrangement, however, the detector will still process hits arriving with time differences that are shorter than this. The result is a *pile-up* of signal strength leading to errors in the position decoding. The decay-time of the amplifier used in this work was $\tau = 150$ ns, which translates to a frequency of $f_\tau \sim 6700$ kHz. The total detection frequency during the experiment was well below.

The input is AC-coupled by C_{in} to allow the anode to be biased to an arbitrary voltage. A typical application would be the use as an electron detector. In this case, the front of the MCP stack has to have a positive high voltage, while the stack itself has to have a positive gradient across itself to accelerate the electrons in the channels, regardless of the charge sign of the detected particle. A typical value at the back of such a configuration would be in the order of 2500 V. The anode needs to be more positive to attract the charge at the back of the MCP. For ion detection, the anode is usually grounded, while the back of the MCP stack is about -200 V.

Following the CSA the signal is processed by a shaping amplifier which turns the it into a gaussian-like pulse. This signal can then be fed to the ADC to be digitalized. Additionally, a shaping amplifier is used for its feature to restore the baseline of the

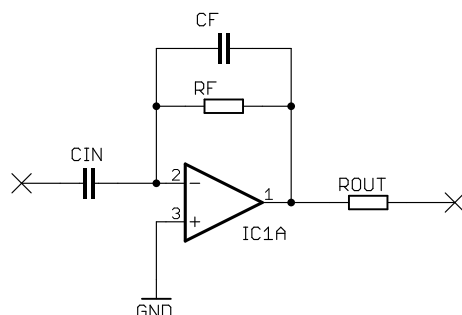


Figure 3.8.: Basic principle of a charge-sensitive amplifier.

signal on a time scale much smaller than the dead time τ , avoiding pile-up at the input of the ADC.

3.3. Target

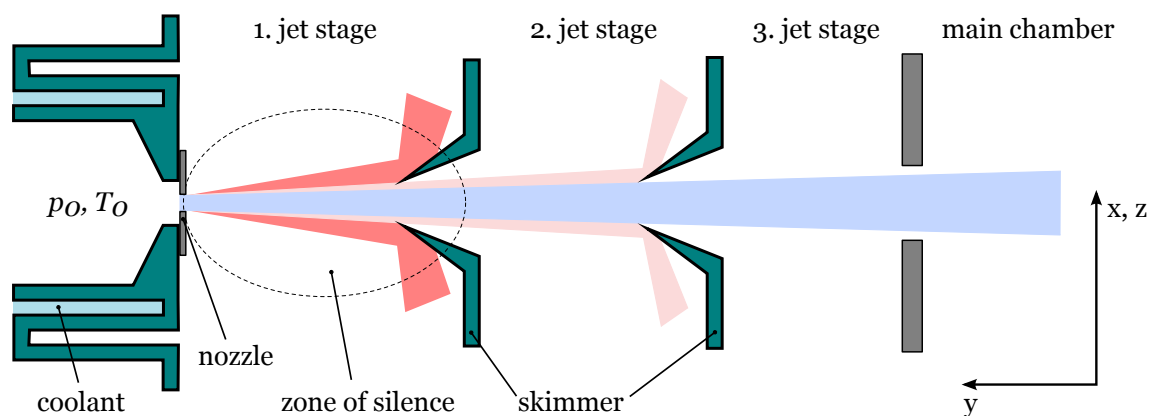


Figure 3.9.: Target preparation via supersonic expansion. The nozzle housing is connected to dewar which allows to adjust the temperature T_0 of the target gas prior to expansion.

In electron impact ionization the scale of momentum that is gained by the reaction fragments is in the order of 1 a.u. This means, of course, the momentum uncertainty of the particles in the initial state has to be much smaller. For the projectile beam this is not usually not a problem. However, the neutral atomic or molecular target beam can easily exceed a momentum uncertainty of 1 a.u. at room temperature making precision spectroscopy essentially futile. For example, the thermal momentum

distribution (fwhm) at room temperature $\delta p_{\text{th.}}(300\text{ K})$ of heavy noble gases like neon and argon – which are subject of this work – with masses of 20 amu and 40 amu, respectively, are $\delta p_{\text{th.}}(300\text{ K})|_{\text{Ne}} = 14.02\text{ a.u.}$ and $\delta p_{\text{th.}}(300\text{ K})|_{\text{Ar}} = 19.83\text{ a.u.}$ These values are not only an order of magnitude larger than the targeted value, they also show that the temperature needed to achieve the desired resolution lies in the 1 K region, severely limiting the possibilities.

The chosen method used in the experiment is based on supersonic expansion of the target gas in a low vacuum region, effectively and efficiently converting the undirected thermal energy $E_{\text{th.}}$ into directed kinetic energy $E_{\text{kin.}}$. Given the experimental parameters, temperatures in the sub-Kelvin regime can be achieved. Of course, there are methods to reach even lower temperatures in the micro-Kelvin regime – and consequently improving the resolution further – like the Magneto-Optical-Trap (MOT) and dipole trap. However, these come with a substantial increase in experimental complexity while at the same time restraining the possible target species to a single atom. In this respect, the *supersonic jet* has the advantage that potentially every gaseous species can be studied. Even liquids can be used in combination with a pick-up gas (usually helium). This, however, comes at the expense of a reduced target density and the accompanying prolonged measurement time.³

The technical realization of the target preparation can be seen in Fig. 3.9. The chosen atomic or molecular species is compressed in the nozzle ($\varnothing = 30\text{ }\mu\text{m}$) with a stagnation pressure p_0 and a temperature T_0 and expands into the first differentially pumped stage (1. jet stage). This stage has to handle by far the highest gas load and is pumped by two turbo-molecular pumps with a maximum pumping speed of about 700 l/s each.⁴ For a common stagnation pressure like $p_0 = 4\text{ bar}$ for argon, the pressure reached in the first stage is as low as $p_{1\text{st}} = 2 \times 10^{-3}\text{ mbar}$.

To increase the resolution a *skimmer* with a diameter of $200\text{ }\mu\text{m}$ is placed at the entrance of the second stage. A second skimmer is placed at the entrance to the third stage ($\varnothing = 400\text{ }\mu\text{m}$). Effectively, they limit the maximal transversal momentum with respect to the jet direction (i.e. $-y$) of the target particles can have in order to pass to the next differentially pumped jet stage. After the third stage the jet enters the main chamber and is crossed with the projectile beam. The part of the

³Seeding the jet with a known ratio can also be used to obtain absolute 3DCSs [Hargreaves et al. (2010)].

⁴The exact pumping speed of this kind of pump depends on the mass of the species being pumped.

jet that does not undergo a reaction with the projectile beam (by far the majority) proceeds to the opposite end of the of the main chamber, where it is guided to another two differential pumping stages called the *jet dump*. The dump effectively removes the excess gas from the main chamber, maintaining a low pressure.

The properties of a supersonic gas jet is extensively studied in [Miller (1988)]. Only briefly, the characteristic variable to determine the jet properties is the *speed-ratio* or the *Mach-number*

$$S_\infty = \frac{v_{\text{jet}}}{v_{\text{therm.}}} \equiv M_T \cdot \left(\frac{\gamma}{2}\right)^{-1/2}, \quad (3.5)$$

which describes the ratio of the velocity of the expanded jet, v_{jet} , and the thermal velocity, $v_{\text{therm.}}$, of the particles in the moving jet frame, i.e., how well the expansion converts random thermal velocity to directed velocity. For ideal gases γ , the heat capacity ratio, can be related to the degrees of freedom, e.g. for a spherically symmetric species like an atom $\gamma = 1.67$ and for a linear molecules such as N_2 or O_2 – neglecting the vibrational modes – $\gamma = 1.4$. In reality γ is a function of the temperature and increases with decreasing temperature. The speed-ratio depends on few experimental parameters, such as the properties of the target gas, the stagnation pressure p_0 and the nozzle diameter d . Amongst the many empirical models to estimate the speed-ratio, the following expression can be found [Miller (1988)]:

$$S_\infty = A \left[\sqrt{2} \frac{p_0 d}{k_B T_0} \left(\frac{53 C_6}{k_B T_0} \right)^{1/3} \right]^B. \quad (3.6)$$

Here, k_B is the Boltzmann constant and T_0 the initial temperature of the gas. All other parameters are empirical and can be found too in [Miller (1988)], pp. 46. For argon, $A = 0.527$, $B = 0.545$ and $C_6/k_B = 7.88 \times 10^{-43} \text{ Kcm}^6$, which gives a speed-ratio of

$$S_\infty(T_0 = 300 \text{ K}, p_0 = 3 \text{ bar}) \Big|_{\text{Ar}} = 29.3. \quad (3.7)$$

The final temperature reached in the expansion is given by

$$\frac{T_f}{T_0} = \frac{\gamma}{\gamma - 1} \frac{1}{S_\infty^2}. \quad (3.8)$$

With the determined speed-ratio, this computes to $T_f = 0.87 \text{ K}$. The final jet temperature is connected to the thermal component of the momentum resolution of the

species	p_0 [bar]	T_0 [K]	S_∞	T_f [K]	v_{jet} [m/s]
Ar	3.0	300	29.3	0.87	527.6
Ne	2.0	77.4	41.1	0.11	393.0

Table 3.1.: Summary of theoretical jet characteristics for the targets important for this work.

ions $\Delta p_{y,i}^{\text{th}}$ by

$$\Delta p_{y,i}^{\text{th}} = 2.35 \sqrt{k_B m T_f}, \quad (3.9)$$

where m is the mass of the species in the jet.

In principle, the velocity can be determined experimentally if one has access to the positions of pure ionized species of known mass and change state (see [Senftleben (2009)] section 4.4.2). However, the difficulty of determining the peak position of the distribution introduces a significant error ($\approx 25\%$ fwhm, *ibid.*). Therefore, in this work the jet velocity is determined by the theoretical determination of the speed-ratio. In table 3.1 a summary of the theoretical jet characteristics are collected. One can see that the expected temperatures are in the targeted range and the target preparation is expected to deliver a sufficiently small momentum spread.

3.4. Electron Gun

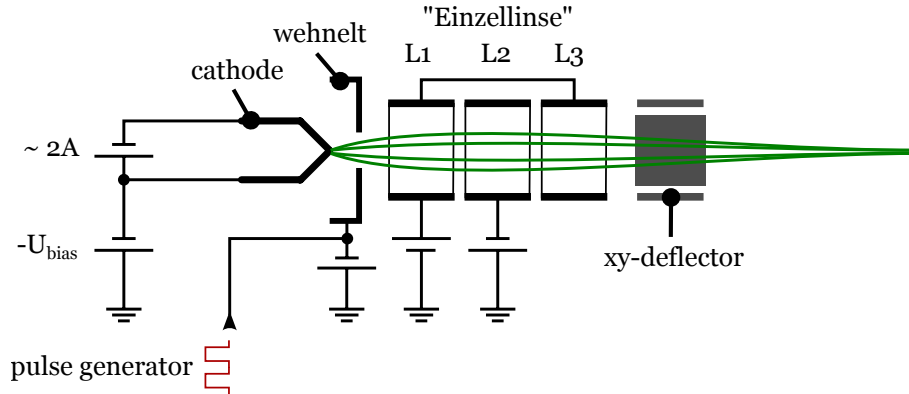


Figure 3.10.: Electron gun.

To create a sufficiently monochromatic and focused projectile beam, a *gun* was employed as depicted in Fig. 3.10. It consists of a tipped thermo-cathode to emit

electrons, a pulsed wehnelt for bunch creation and a *Einzellinse* and deflector section for focusing and steering. For stable working conditions, the wehnelt is biased negative with respect to the cathode, effectively blocking electron emission. A pulse generator is then used to modulate positive spikes on top with a frequency of $f_{\text{gun}} \sim 200$ kHz, creating bunches of approximately 10^4 electrons. The estimated fwhm of the pulse length is in the order of 1 ns. An electrostatic lens focuses the beam and counteracts the repulsion of the electrons within each bunch. The alignment of the projectile beam is quite challenging since not only a firm overlap with target beam has to be achieved. Additionally, it has to pass the hole in the ion detector with an inner diameter of 5 mm and a length of 45 mm. Furthermore, the unscattered beam has to hit the hole in the electron detector's MCP to prevent it from saturating.

The focusing procedure is supported by phosphor screen that can be moved directly in the interaction region. A commercial web-cam is used to image the screen while adjusting the focus. In this way foci of ≤ 1 mm are achieved. Since this value is rather large compared to laser foci, there is the need to apply time-focusing to decouple the TOF from the starting point within the jet.

To adjust the projectile energy, the cathode is biased to a negative voltage with respect to the interaction region. The total kinetic energy of the electron is then defined by the potential difference $\phi_{\text{int.}} - \phi_{\text{cath.}}$. Since the interaction region is kept on ground potential (i.e. 0 V) the kinetic energy is simply $E_{\text{kin.}}[\text{eV}] = eU_{\text{bias}}$. This setup is able provide projectile energies ranging from 25 eV to 1000 eV and can cover a broad range of interaction regimes.

3.5. Data Acquisition

The principle of this work is based on the coincidence technique, where two or more particles emerging from a reaction have to be detected coincidentally. Since the data recording has a finite capacity as to how fast data can be written, there is the need to distinguish *real* events from false ones. In the present experiment this is accomplished by a hardware trigger system. A highly simplistic scheme is depicted in Fig. 3.11. Briefly, the *pulser* which shoots the electron gun is inhibited only under the special condition when the event was deemed good. What good means in this respect will be explained later. A signal of the pulser goes to the time-to-digital-

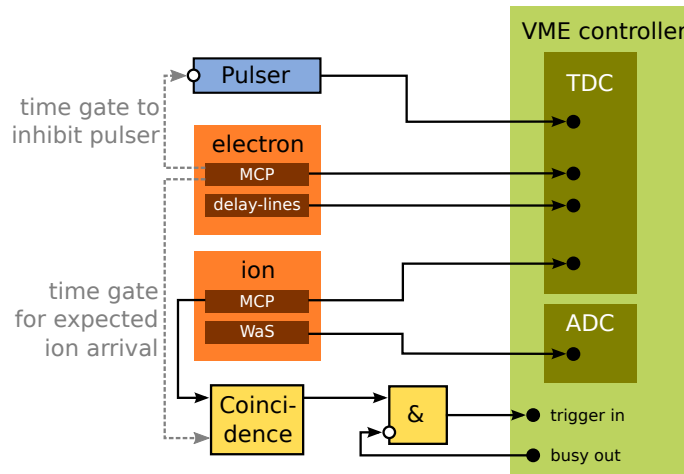


Figure 3.11.: Hardware coincidence trigger and data acquisition (from [Senftleben (2009)]).

converter (TDC). The operation mode of the TDC is *common-stop*, by which the times are referenced with respect to a trigger signal which arrives latest. After a shot of the gun gates open the MCPs and if at least one incident is detected for the electron MCP and one for the ion MCP the data acquisition system is triggered to write the data off the TDC and analog-to-digital-converter (ADC) only if the acquisition does not report to be busy. In the latter instance the event will be discarded.

In more detail, in order for the event to be good, a maximum in time is set which is the latest an electron is allowed create a MCP signal with respect to the pulser. Consequently, we call the event rate that fulfills this condition *good electrons*, since it accounts for the physical nature of the studied reaction. Additionally, the gun is blocked to avoid multiple reactions within one event and the accompanying false coincidences. Secondly, the pulser creates a gate for the ion MCP which is set according to the expected TOF of the respective ionic mass.⁵ If an ion is detected the pulser is inhibited and the acquisition is triggered. The respective count rate is called *valid coincidence*. The event is stored in a listmode file by a MBS stream server which controls the data acquisition and written to a local computer equipped with a raid system. At the same time online monitoring of the collected data is

⁵On a μs time scale it is a safe assumption that the ion TOF is independent of momentum gained in the reaction.

3. The Reaction Microscope

enabled by *go4*.

For the present experiment a multi-hit TDC was used with a time resolution of 100 ps and a dead time of 5 ns. The total recording time of $\sim 50 \mu\text{s}$ was sufficient since the electrons arrive within $\approx 500 \text{ ns}$ while the ions – due to the much larger mass – arrive in the μs regime. However, since the distance to the ion detector was drastically shortened (see section 3.1), so was the TOF for the ions. The data taking for the wedge-and-strip anode consists of a charge-sensitive-amplifier (CSA) and an ADC to convert the charge information into a digitally processable signal.

4. Data Processing and Analysis

It has already been mentioned that in terms of $(e, 2e)$ -experiments the employed technique for this work, described in chapter 3, differs fundamentally. While a conventional $(e, 2e)$ -apparatus measures count rates directly proportional to the 3DCS by scanning the scattering angles and energies in one plane with movable detectors, a REMI is based on imaging techniques where particles are projected onto detectors of a confined detection area.¹ The data collected in this way represents – by itself – no physical meaning: it is *raw* data.

This chapter aims to give an overview on how the collected raw data is processed and analyzed by converting the digital signals from the acquisition system (section 3.5) into physical measures of position and time; finally into momenta. Having acquired the momentum information of all charged fragments, a kinematically complete picture of the reaction is gained. Hence, by selecting the necessary variables 3DCSs can be displayed.

Furthermore, the acceptance and resolution for electrons and ions of the experimental setup will be discussed.

4.1. Data Analysis Code

The basis for data processing and analysis is the CERN developed C++ library ROOT. It provides a large functionality concerning the visualization and manipulating of data. Its main goal is to provide all necessary tools to build a custom analysis. A convenient way of using ROOT and extending its possibilities is the *GSI online/offline object-oriented* framework *Go4*. Basically, it represents a graphical user interface (GUI), an integration for the MBS streaming server (section 3.5) and a general organization to easily organize a data stream into a multi-step analysis

¹An apt description would be the somewhat oxymoronic term *imaging coincidence technique*.

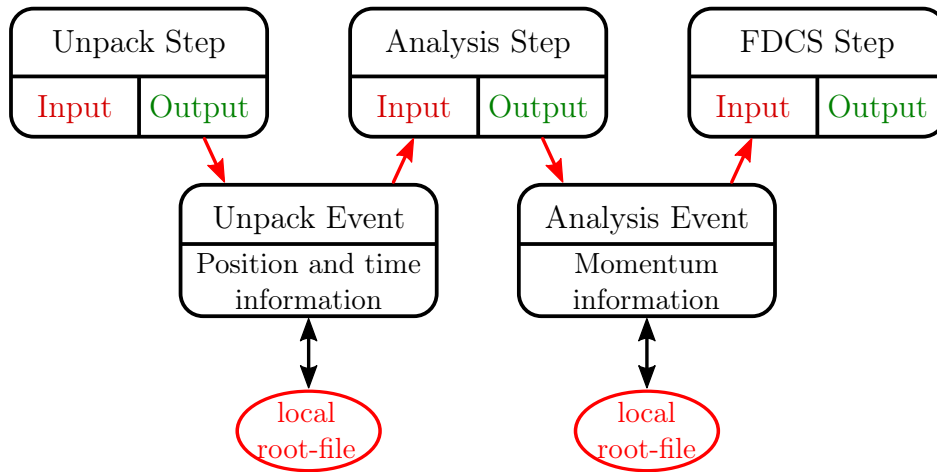


Figure 4.1.: Signal flow for the $(e, 2e)$ adapted version of the GENERiC project.

with input and output options. A great advantage is the parameter object which enables the use of custom parameter classes. The members of these classes can be used as variables to calibrate the data and can be changed interactively during runtime. The analysis input can either be a direct stream from the MBS server as well as local list-mode files and can therefore be used for online monitoring of an experiment and offline processing and analysis.

For the purpose of using Go4 for with experimental data acquired by REMIs, an analysis code named GENERiC was developed that could be adapted for a multitude of different experiments (see [Senftleben (2009)]). The general idea is that without regarding the specific reaction, the basic task of calculating the momentum of a particle is identical and so most of what is needed to perform this task can be generalized into classes and functions. The principal signal flow for the $(e, 2e)$ adapted GENERiC version can be seen in Fig. 4.1. The complete analysis from conversion of the raw data to acquiring the 3DCS has been divided into three different steps: Unpack, Analysis and FDACS. Each step has been assigned to a sole purpose. The Unpack step converts the raw data into physical time and position information. This information is gathered for each particle and each event and is presented at the output of this step. It is then transported to the next step (i.e. in this case Analysis) while, at the same time, the information can be written to a so-called root-file which is capable of storing all the event information. By doing so, the momentum calibration could be performed starting directly from the second

step with the previously saved output. This scheme was adapted to optimize the time to analyze a set of data. For instance, the conversion of raw data usually takes longest since here the double coincident TDC data has to be sorted and checked for triple coincidences. Furthermore, due to the amount of information produced, the delayline detector data (see 3.2) has to undergo sophisticated reconstruction algorithms to account for missing signals to maximize the event rate. The calibration performed in this step is to the most extent independent of the physical reaction. By performing this task once and saving the output the remaining analysis can be completed at much higher rates. With the momentum information of the second step it is possible to select specific reaction channels which can include additional calibration efforts. Additionally, by saving the parameter values of a step (or a sequence of steps) along with the output of the previous step the analysis outcome can always be recreated.

4.2. Time and Position Information

Upon recording of the raw data all hits are referenced to a more or less arbitrary signal, which is basically the first MCP hit on the ion detector (see section 3.5). The first measure in decoding the time-of-flight (TOF) information is to calculate the time differences with respect to the pulser of the electron gun (section 3.4). Although the pulser represents a common point in time for all reactions, it does not coincide with their exact origin due to the time the projectile needs from the gun to reach the interaction volume. While this time might be considered small on a typical micro-second scale for the ions, it is, however, essential for the TOF of the electrons, which is on a nano-second scale. Since this time is not accessible experimentally, it has to be reconstructed during the offline analysis. A sketch of the situation is depicted in Fig. 4.2. Here, the red line marked t represents the actual TOF of a particle, while t' indicates the measured raw time, referenced to the pulser.

The adopted procedure makes use of the fact that the electron's movement is greatly influenced by the homogeneous magnetic field, forcing them on a helicoid trajectory (see section 3.1). Since each electron starts on the spectrometer axis, it has to return to this same axis after each revolution. For such a relatively simple problem of an accelerated charge with a superimposed magnetic field it turns out

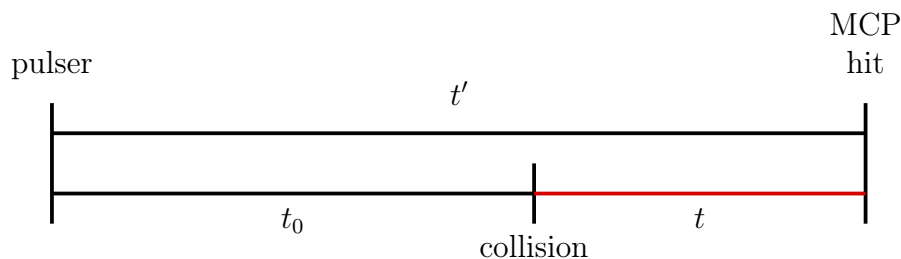


Figure 4.2.: Scheme for the reconstruction of the real time-of-flight of a particle from the collision to the arrival on the detector.

that the time T_c for one revolution depends on the magnetic field strength only, making it essentially constant for a given experimental setting. Additionally, since all electrons return to the spectrometer axis regardless of their transversal momentum, there must be nodal points in a representation where the radial position on the detector is plotted against the TOF. These nodes are points where the momentum information is lost due to a common position of arrival at the detector. Since the electron detector has a hole at its center to prevent the unscattered electrons from hitting the MCP, the position of this common point cannot be detected. However, Fig. 4.3 shows such a plot and the equidistant nodes are clearly visible.

A couple of information can be gained from such a representation. Since the magnetic field defines the cyclotron time T_c , a precise value can be calculated by determining said time. Additionally, the time origin of the reaction can now be retrieved by assuming that the collision took place on the spectrometer axis. This, generally safe assumption, leads to the conclusion that the point of collision in Fig. 4.3 must have been a node, too. Hence, between the *real* zero time and any other node of the spectrum must be an integer number of nodes. Consequently, the difference of the TOF of a particular node t'_n and the real time of that node t_n with respect to the origin is $t_0 = t'_n - t_n$, where $t_n = i \cdot T_c$, $i \in \mathbb{N}$ can be expressed as a multiple of the cyclotron time.

Typically, T_c can be measured to a precision in the order of 0.1 ns. This procedure brings the uncertainty for t_0 down to $\mathcal{O}(T_c)$, which is in a common setup ~ 40 ns. This difference is easy observe if one compares the calculated sum energy of the two final state electrons to the estimated energy of the gun setup.

In contrast to the time, the reconstruction of the position information depends on the type of detector that was used (section 3.2). For the hexanode a thorough

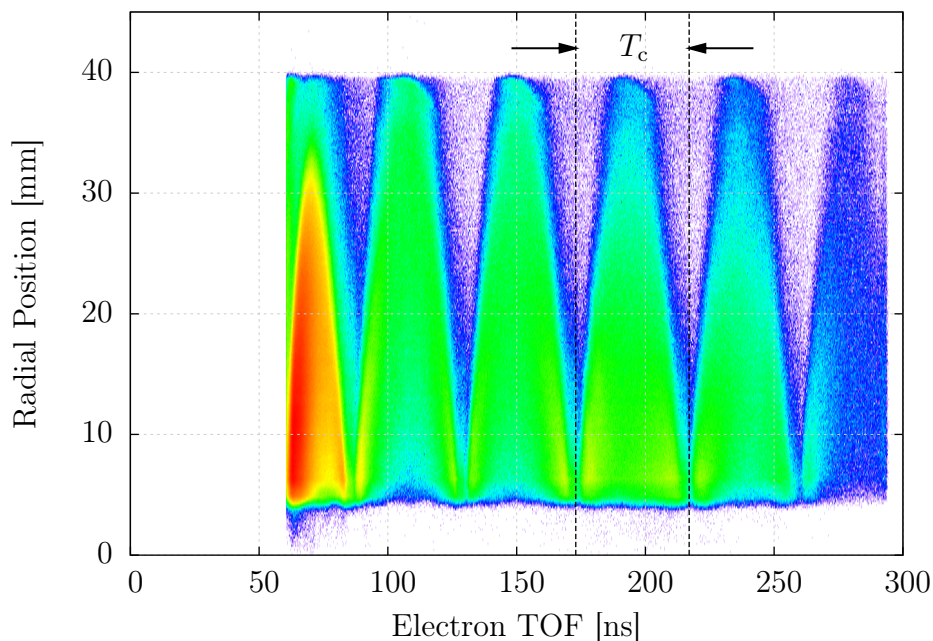


Figure 4.3.: Electron time-of-flight versus radial detector position.

documentation of the position calculation and the reconstruction of missing signals can be found in [Senftleben (2009)]. Briefly, each layer produces two signals which represent the duration the impinging charge needs to reach both ends of the wire (t_1, t_2). Since the length of the wire is constant, so is the sum of the arrival times $t_{\text{sum}} = t_1 + t_2$. This relation can be used for each layer to discriminate true events from false ones and even to reconstruct missing signals. Since a hexanode has three layers, (x, y) information can be obtained from any combination of two layers (i.e. (u, v) , (u, w) and (v, w)), which makes in total three possibilities

$$\begin{aligned}
 \begin{pmatrix} x_{uv} \\ y_{uv} \end{pmatrix} &= \begin{pmatrix} u \\ \frac{1}{\sqrt{3}}(u - 2v) \end{pmatrix} \\
 \begin{pmatrix} x_{uw} \\ y_{uw} \end{pmatrix} &= \begin{pmatrix} u \\ -\frac{1}{\sqrt{3}}(u + 2w) \end{pmatrix} \\
 \begin{pmatrix} x_{vw} \\ y_{vw} \end{pmatrix} &= \begin{pmatrix} v - w \\ -\frac{1}{\sqrt{3}}(v + w) \end{pmatrix}.
 \end{aligned} \tag{4.1}$$

A crucial issue in determining the position is the overlap of the layers. In (4.1)

it is assumed that all three coordinate systems have exactly identical origins. In reality this is hardly the case and the layer coordinates have to be modified. This can be done by scaling the coordinates with three parameters ($\mathcal{S}^u, \mathcal{S}^v, \mathcal{S}^w$) and, additionally, for one coordinate the possibility of an offset has to be considered (\mathcal{O}^w). The calibration can be performed by providing histograms where a coordinate is calculated by the combination of two layers (e.g. y_{vw}) and plotted against the difference of the same coordinate calculated by the other two possibilities (i.e. $y_{uw} - y_{uv}$). The difference of a coordinate which was calculated using different layers should be zero and, consequently, be independent of the coordinate itself. This is done of every permutation of layers and so each layer can be calibrated.

For the second type of detector used for this work – the wedge-and-strip anode – determining the position is much simpler. As indicated in section 3.2, (xy) -coordinates can be obtained by measuring the amount of charge collected by the different electrodes. These coordinates have then to be scaled to represent the real active area of the detector. Additionally, it has to be considered that the specific geometry of the anode can lead to distortion of the detector image. This can happen if the area covered by the charge cloud that reaches the anode is too small and covers less than one period of the structure, or if it is too large and a substantial amount of the charge is not detected. The latter leads to distortion at the outer boundary of the anode. Especially for large anodes, a third kind of distortion can occur which is also known as *cross-talk*. This effect is caused by the inter-electrode capacitance. The capacitance is mainly due to the area of the electrode created by its finite thickness. Two adjacent electrodes will then form a capacitor. A way to compensate for this effect during the analysis can be found in [Zhen-Hua et al. (2008)]. Since the calibration of the position does not depend on the experimental settings of the spectrometer or the target species, it is usually done once by using a resolution mask in front of the detector. This is a simple plate with an grid of equidistant holes of known distance and diameter. In this way, the image can be precisely optimized. Figure 4.4 shows two exemplary cases for the ionization of neon, where for panel (a) cross-talk correction has been applied while for panel (b) it was turned off. Since cross-talk correction changes the (x, y) -position, the image in panel (b) was re-centered. The two position images visualize the effect of inter-electrode cross-talk which leads to an *egg-shaped* distortion with a slight tilt, despite the fact that the amplification of the position signals were carefully adjusted.

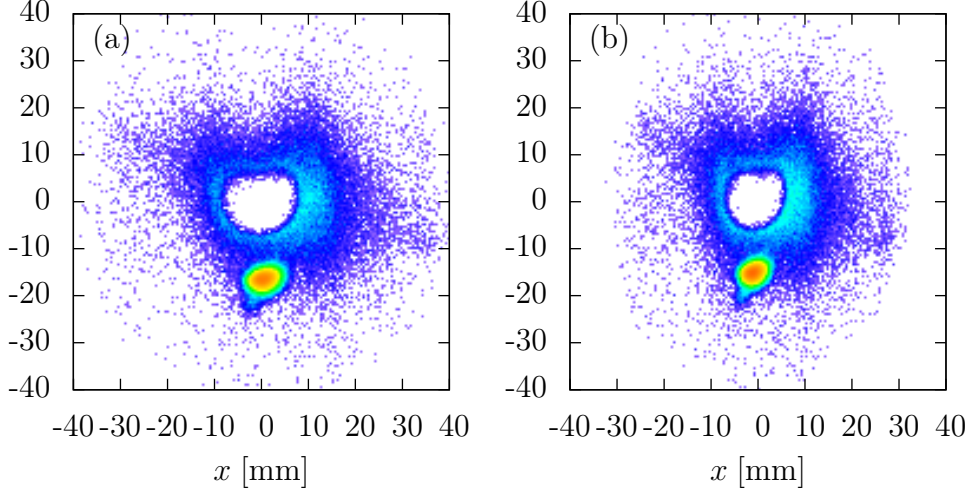


Figure 4.4.: Ion position images for neon. (a) with cross-talk correction, (b) without cross-talk correction.

4.3. Momentum Calculation

In the previous section it has been outlined how to retrieve the time and position information of a charged particle emerging from an ionization event in a REMI. To achieve the final goal – determining the 3DCS of a specific reaction – this information has to be used to calculate the particle’s momentum. The construction of the spectrometer (section 3.1) permits to split this task into two subsequent calculations: the longitudinal momentum p_z , which is a function of the particles TOF, and the transversal momentum p_r which, additionally, depends on the (xy) -position on the detector. In the wake of generalizing the analysis, the methods used to accomplish the calculations do not distinguish between species of particles such as electrons or ions.² In the end, the momenta for three particles in the case of single ionization are determined. These are the ion momentum \vec{p}_i and the two electron momenta \vec{p}_{e1} and \vec{p}_{e2} . They provide a kinematically complete picture of the ionization process.

²In principle, it is possible to find approximative solutions for the longitudinal momentum depending on the mass (e.g. [Pflüger (2008)]). Due to the robustness of the used method this distinction was dropped.

4.3.1. Longitudinal Momentum

The retrieval of the longitudinal component of the momentum p_z revolves around the fundamental formula for the time-of-flight of a charge that passes an acceleration region of the length a and an adjacent field-free drift region of the length d :

$$t(p_z) = m \left(\frac{2a}{\sqrt{p_z^2 + 2mqU} \pm p_z} + \frac{d}{\sqrt{p_z^2 + 2mqU}} \right). \quad (4.2)$$

Here, the acceleration potential is U , m is the particles mass and q its charge. Whether the \pm -sign is positive or negative depends on the direction with respect to the z -axis in which a particle is accelerated.

To obtain the momentum for a measured TOF, the inverse of (4.2) needs to be found. As general it may look like, no analytical expression for the inverse can be found for $p_z(t)$. Still, the longitudinal momentum can be retrieved by iteratively finding the root for the equation $f(p_z) := t(p_z) - t'$ using the Newton method.³ Here, $t(p_z)$ is the analytic expression (4.2) and t' the measured TOF of the particle. The algorithm varies p_z from a given starting value until the solution is found within a given precision. Assuming convergence and uniqueness, we will naturally obtain $p_z(t')$.

4.3.2. Transversal Momentum

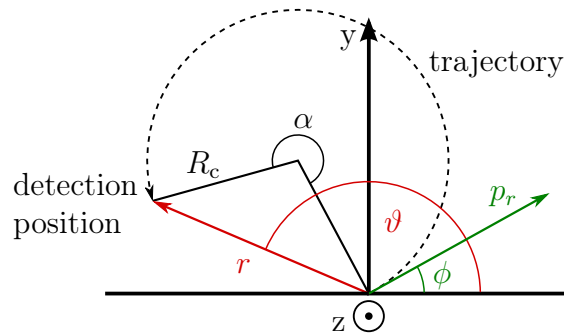


Figure 4.5.: Electron trajectory in the xy -plane.

The influence of the magnetic field on the particle's trajectory has been mentioned before. Here, this motion has to be considered in order to reconstruct the right

³The actual implementation can be found in [Senftleben (2009)], pp. 127.

transversal momentum and azimuthal angle. Figure 4.5 depicts the situation. A particle with a transversal momentum p_r emerges from the collision with an angle ϕ (depicted in green). The magnetic field – here in z -direction – forces it on a circular trajectory along the dashed line until it arrives at the detector. The center of this trajectory with the radius R_c does not coincide with the origin of the xy -plane (which is also the center of the detector). The measured (x, y) -position is then given by the distance to the origin r and the angle ϑ (red). The steps necessary to obtain the actual momentum are outlined in the following.

The connection of the cyclotron time T_c , which it takes the particle to complete a full revolution, and the magnetic field B_z is given by

$$\frac{2\pi}{T_c} = \frac{q}{m} B_z \equiv \omega_c . \quad (4.3)$$

Here, q/m is the charge-to-mass ratio of the particle. From Fig. 4.3, the value of T_c can be determined experimentally. Additionally, R_c can be expressed in terms of the particles momentum p_r

$$R_c = \frac{T_c}{2\pi m} p_r . \quad (4.4)$$

On the other hand, the angle $\alpha := \omega_c t'$ in Fig. 4.5, which is connected to the TOF of the particle t' , can be used to determine R_c with a simple textbook approach

$$R_c = \frac{r}{2|\sin(\alpha/2)|} . \quad (4.5)$$

Altogether, this leads to an expression for the transversal momentum containing only variables which are accessible experimentally

$$p_r = \frac{\omega_c m r}{2|\sin(\omega_c t'/2)|} , \quad (4.6)$$

Finally, the remaining coordinate to describe the transversal momentum is the azimuthal angle ϕ . Obviously, it can be expressed as

$$\phi = \vartheta \pm \frac{\omega_c t'}{2} \pmod{2\pi} \quad (4.7)$$

where the second term is positive for clockwise and negative for counterclockwise movement. Looking at Fig. 4.5 with the magnetic field parallel to z , the electrons

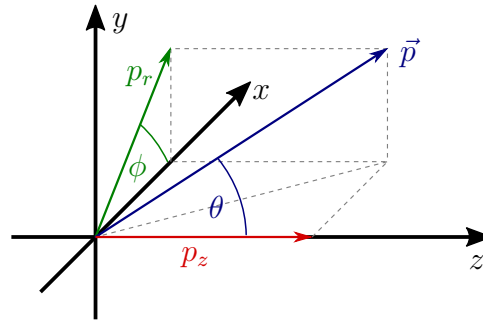


Figure 4.6.: Overview of the components of a momentum vector in cylindrical coordinates.

travel ccw, while positively charged fragments move cw.

In Fig. 4.6 an overview of the vectorial components in cylindrical coordinates of a momentum vector is shown. The transversal momentum p_r and the longitudinal momentum p_z with the respective azimuthal and polar angles ϕ and θ hold the necessary information of the particle.

4.4. Calibration Procedure

The situation in an electron collision is as such that ions and electrons gain a similar amount of momentum. Since the mass ratio – 1836 for a proton – is very large, the energy of the ions is usually negligible. The same holds in terms of momentum, where the electron's magnitude is usually exceeded by the ions. This leads to the following conclusion: for the electrons energy conservation should be very sensitive on the momentum calibration where as for the ions, the momentum conservation should be sensitive on the momentum calibration.

The need for a calibration procedure is due to the principle of the measurement. Since the particles are projected to the detector by means of fields, a precise knowledge of those fields as well as the geometries would be required to omit such a procedure. It is, however, impossible to know e.g. the *real* extension of the acceleration field precise enough. Consequently, knowledge of the physics involved are used to make up for this fact by using a well known reaction for the calibration. Usually, every experimental setting is additionally studied with helium as a target which proves to be well suited to provide the necessary parameters.

What is usually considered for the calibration of the electron's momentum is the so-called *energy sum* E_{sum} . It consists of the sum energy of all final state electrons which – in a $(e, 2e)$ -experiment – is $E_{\text{sum}} := E_{e1} + E_{e2} \equiv \frac{\vec{p}_{e1}^2}{2m_e} + \frac{\vec{p}_{e2}^2}{2m_e}$. For a known reaction the energy sum is connected with the projectile energy E_0 by energy conservation $Q = E_0 - E_{\text{sum}}$. The internal energy Q is the difference of the initial and final state energy of the target. Here, the energy of the ion is neglected as indicated above. To justify, a quick comparison can be presented: 1 a.u. of momentum for argon with a mass of 40 amu is equivalent to a kinetic energy of 0.2 meV while it is 13.6 eV for an electron.

In Fig. 4.7 an exemplary energy sum plot is shown for single ionization of neon with a projectile energy of $E_0 = 61$ eV. Here, information of the longitudinal momentum sum $p_{z,\text{sum}} = p_0 - (p_{e1} + p_{e2} + p_i)$ has been used for the selection of triple-coincident events. The whole spectrum consists of only one contribution at 39.68(1) eV which corresponds to the first ionization potential $\text{Ne}^+(2s^22p^5)$ of 21.56 eV. No contribution of the second potential $\text{Ne}^+(2s2p^6)$ which lies 26.91 eV above the first can be observed. This is mostly due to the fact that the ionization cross-section for inner-shell ionization is in general low. At the same time the projectile energy is small which additionally reduces the probability of a $2s$ ionization.⁴

The possibility of calibrating the longitudinal momentum is based on two parameters: \mathcal{S}^{pz} and \mathcal{S}^t . The former allows to scale the momentum directly while the latter scales the TOF in (4.2), $p'_z = \mathcal{S}^{pz} \cdot p_z(\mathcal{S}^t \cdot t')$. Since the dependence of the longitudinal momentum on the TOF is non-linear, a way to choose this parameter involves a plot of the energy sum versus the individual electron's longitudinal momenta. Figure 4.8 shows an already calibrated example. The individual momenta $p_{z,ei}$ should, of course, be independent of the energy sum E_{sum} due to energy conservation. Consequently, as in Fig. 4.8, the data should resemble a vertical line. The parameter \mathcal{S}^t can be used to precisely account for that. The dashed lines represent the acceptance boundary which is created by the center hole of the MCP.⁵

As an example, Fig. 4.9 shows the same data as in Fig. 4.8 but with the time

⁴The $2s$ contribution is about an order of magnitude smaller [Bartlett and Stelbovics (2002)]. The total cross-section σ_T for electron impact ionization of neon has a maximum at 200 eV. At 60 eV it is already decreased by roughly half its maximum value [Rapp and Englander-Golden (1965)].

⁵Without a hole the gaps converge to horizontal lines where different transverse momenta have the same position and momentum information is lost as a consequence.

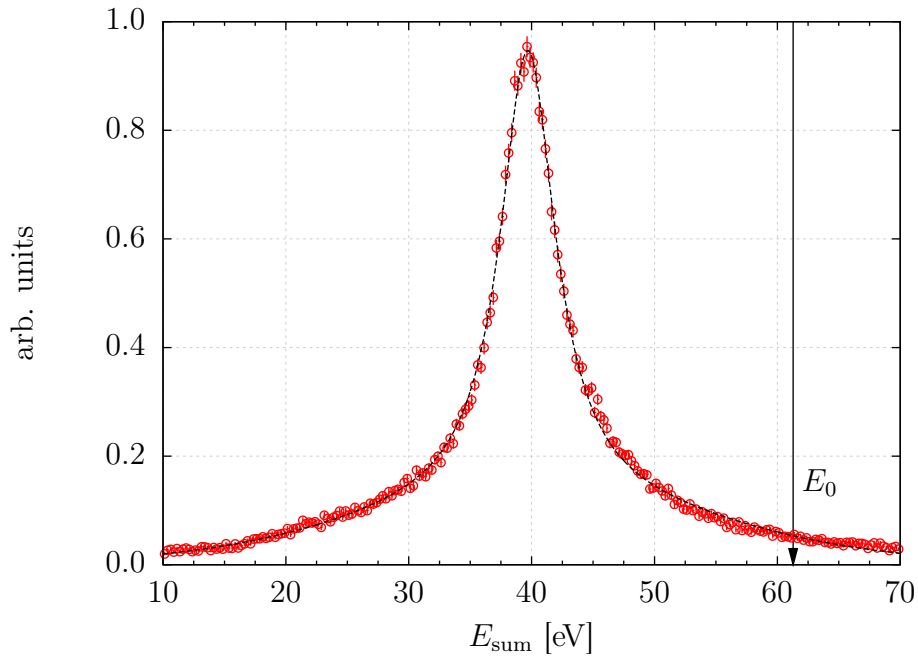


Figure 4.7.: Energy sum spectrum for single ionization of neon with a projectile energy $E_0 = 61$ eV. The fwhm of the fit is $\Gamma = 6.50(7)$ eV and its mean $E_p = 39.68(1)$ eV.

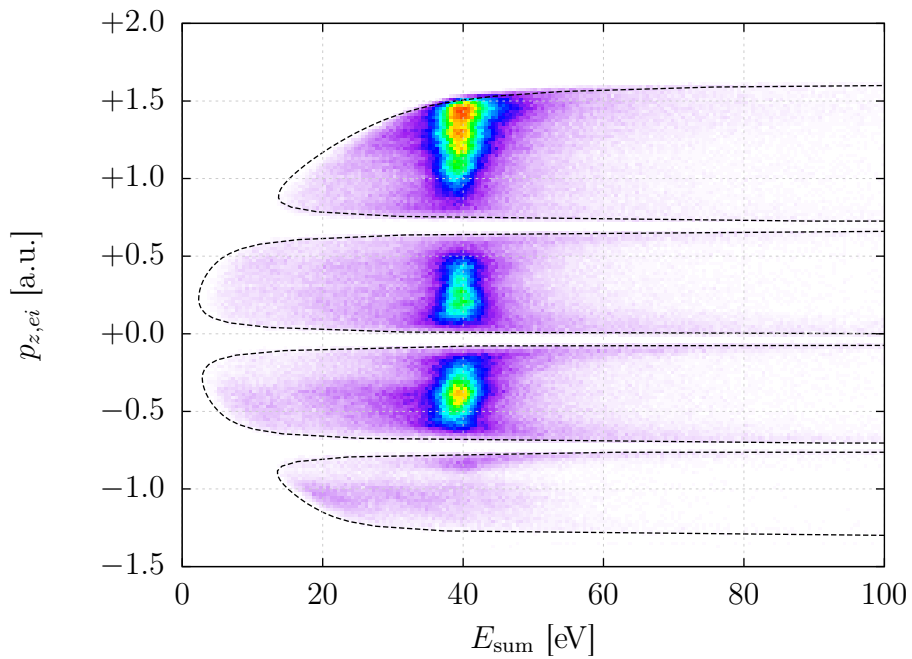


Figure 4.8.: Energy sum vs. $p_{z,e1}, p_{z,e2}$ for ionization of Ne at $E_0 = 61$ eV.

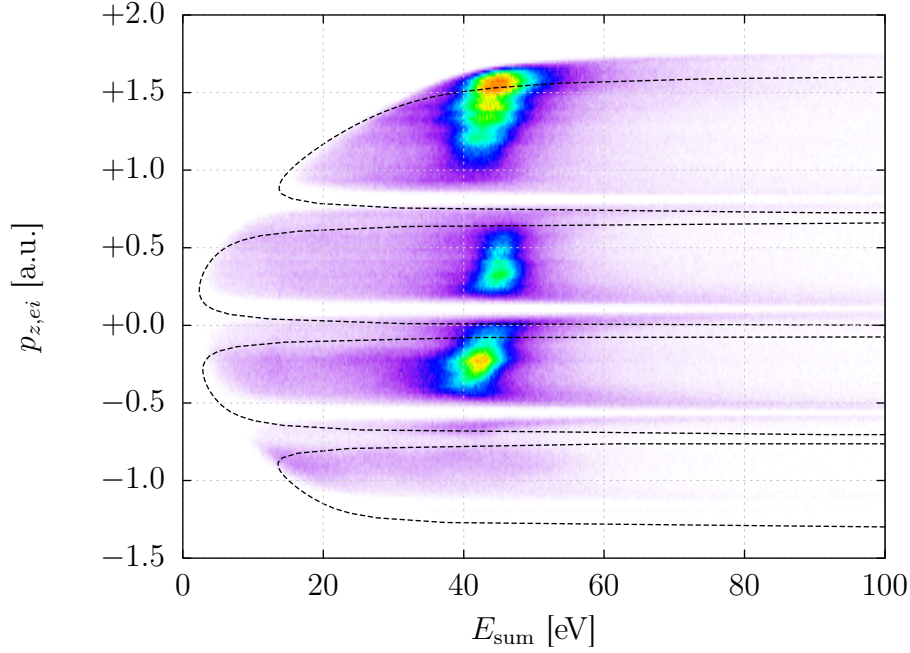


Figure 4.9.: Same plot as in Fig. 4.8 but with \mathcal{S}^t off by -5% . The dashed lines represent the minimum radius boundary.

scaling off by -5% . It is apparent that not only does a lower \mathcal{S}^t shift the distribution towards larger momenta but also does it shift the peak structure towards larger values of the energy sum but with a dependence on p_z which results in a tilt of the line structure. A vice versa effect can be observed for an increasing time scale parameter. In essence, \mathcal{S}^t is used to corrects for of the geometrical extensions of the spectrometer.

The effect of a precise value for the magnetic field B_z is of major importance. The connection of the determined time origin t_0 and the cyclotron time T_c is very sensitive. Consequently, a proper value for the magnetic field has to be found. A mis-calibration with respect to the value for Fig. 4.8 is shown in Fig. 4.10. The field value for B_z was chosen to be $+0.1$ Gs – about 1% – compared to the final calibration. The biggest impact is for electrons with small longitudinal momentum. For large momenta – even at intermediate energies such as 61 eV – the corresponding electron is most likely the scattered projectile. The transversal component is then small and so is the effect of the magnetic field. As one can see, the peak distribution

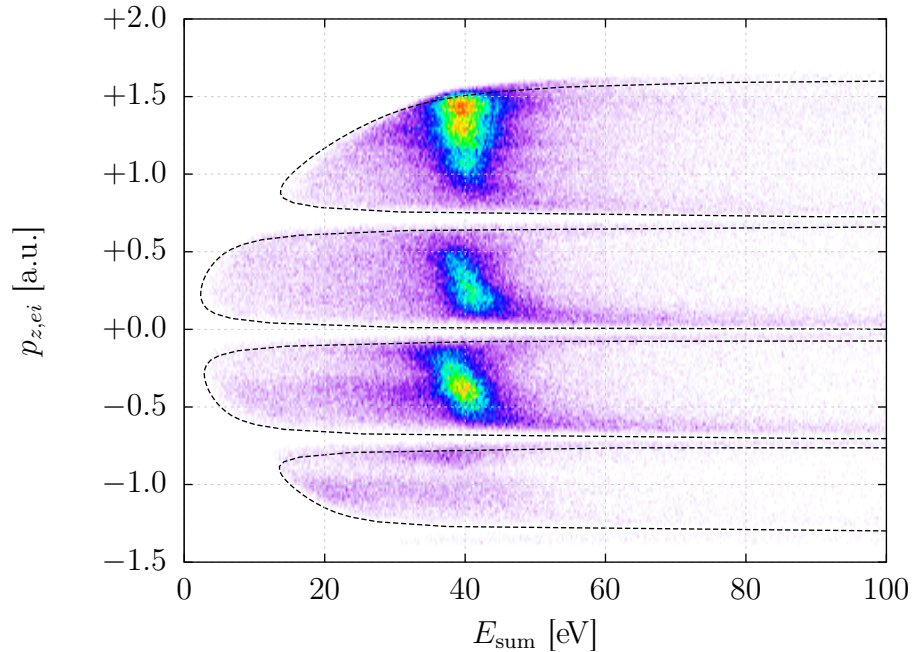


Figure 4.10.: Mis-calibration of the magnetic field B_z by +0.1 Gs. The dashed lines represent the minimum radius boundary.

is rotated with respect to the center of the wiggles counterclockwise .⁶

Calibration of the ion momentum is of lesser importance if only the $(e, 2e)$ cross-section is studied. There are, however, two exceptions where the ion momentum is needed. These are

low projectile energies Here, the final state electrons have comparable energies and for a good deal of instances comparable TOFs. This can lead to difficulties in isolating the two detector hits due to its dead-time. In these case the ion momentum could be used to calculate one electron.

molecular alignment If, additionally to the $(e, 2e)$ cross-section, information of a particular molecular alignment or dissociation channel is to be acquired, the ion momentum information has to be used.

In all other cases, the ion is mostly used as a trigger to reduced the background further and a precise calibration can be disregarded.

⁶If the field value were reduced the corresponding rotation is clockwise .

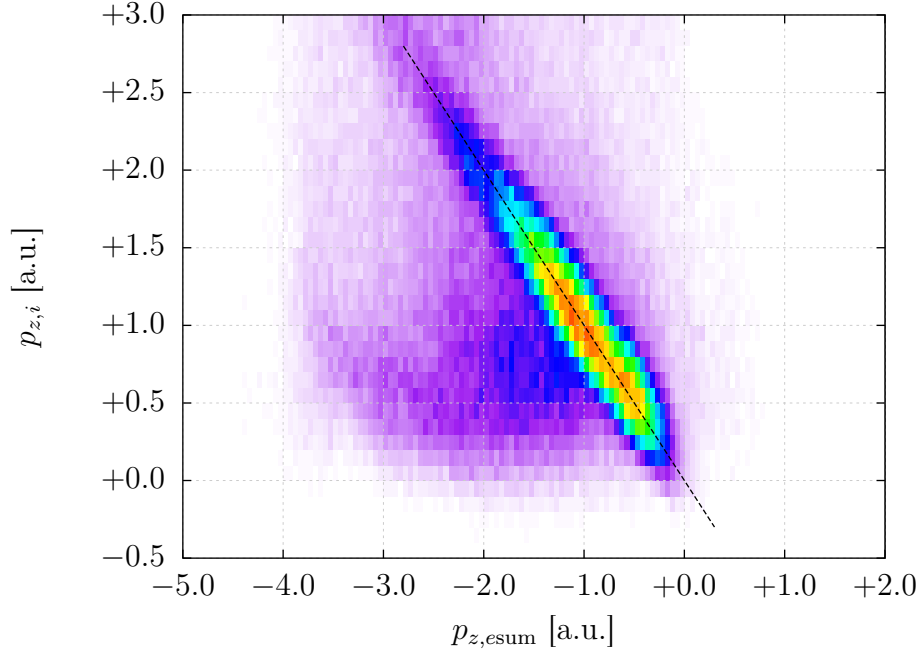


Figure 4.11.: Electron longitudinal momentum sum $p_{z,\text{sum}}$ vs. ion longitudinal momentum $p_{z,i}$ for ionization of Ne at $E_0 = 61$ eV.

Since the calculation of the momentum is identical for electrons and ions, the parameters for calibration are the same. The associated histograms to find precise values are, however, the longitudinal momentum sum $p_{z,\text{sum}} = p_{z,e1} + p_{z,e2} + p_{z,i}$ and the electron longitudinal momentum sum $p_{z,\text{esum}} = p_{z,e1} + p_{z,e2} - p_{z,e0}$ against $p_{z,i}$. The same is done for the transversal components x and y . Due to momentum conservation, a representation like the latter should give a negative 45° slope as shown in Fig. 4.11. The same calibration is repeated for the transversal momentum components ($p_{x,i}$ and $p_{y,i}$). These depend strongly on the on the position resolution and the mass of the ion. A general rule of thumb is that the larger the mass is the lower is the transversal momentum resolution (see next section).

4.5. Experimental Resolution

In the following section it is examined how the calibration of the spectrometer can be quantified in terms of experimental resolution and acceptance. First, section 4.5.1 will give an overview of the expected acceptance for electrons and ions. Additionally,

the acceptance for dissociative ionization will be discussed. Finally, in section 4.5.2 the experimental resolution for the given experimental settings will be explored.

4.5.1. Acceptance

In a REMI the detection acceptance depends on the particle. In general, a single ionization event leaves the ion and the ionized electron with comparable momenta, but because of the tremendous difference in mass, the ions obtain only negligible kinetic energy. The electron, however, gains considerable kinetic energy, which makes it necessary to apply a magnetic field to increase the acceptance greatly (cf. section 3.1). The ion acceptance depends on the type of reaction that is to be studied. For an ordinary ($e, 2e$) or (e, ne)-experiment, the initial momentum of the supersonic expansion in the $-y$ -direction by far exceeds the momentum gained in the collision. Then, it is only a matter of the acceleration field being sufficiently high so the ions still are able to hit the detector (see Fig. 3.1). A list of acceptance values for the experimental conditions of this type of experiment is collected in table 4.1.

If the process involves dissociation into two charged fragments the situation changes. Depending on the KER and the mass of the fragments of the molecule, this momentum can exceed the initial momentum by two orders of magnitude, imposing severe constraints on the acceptance and the overall resolution (see table 4.2). The other important issue concerning the ion acceptance is the longitudinal direction. Especially for heavy clusters, with a given acceleration field, the TOF can exceed the total range of the TDC.

Electron Acceptance

The transversal acceptance for the electrons depends on the magnetic field. From (4.4) one can extract an equation for the diameter as a function of the transversal momentum of the helicoid of the electron trajectory, scaled to applicable units:

$$D_c [\text{mm}] = 248 \cdot \frac{p_r [\text{a.u.}]}{B_z [\text{Gs}]} . \quad (4.8)$$

In the experiment the dimensions of the MCP used are 80 mm in diameter and a 6 mm hole in the center (cf. section 3.2). The active area of the MCP is slightly

smaller. The maximum transversal momentum that can still be detected is

$$p_{r,\max} [\text{a.u.}] = 0.16 B_z [\text{Gs}] , \quad (4.9)$$

where the maximum diameter has been accounted for as 40 mm. For a typical magnetic field value of 10 Gs this computes to $p_{r,\max} = 1.6$ a.u. which corresponds to a maximum energy for the ejected electrons of $E_{e2,\max} = 35$ eV. In the same fashion, the minimum transversal momentum can be determined. The lower boundary for the active area created by the hole will be accounted for by a 8 mm diameter, since the channels do not extend to the hole. In this case, (4.9) gives a momentum of $p_{r,\min} = 0.16$ a.u. which corresponds to $E_{e2,\min} = 0.35$ eV. Actual experimental values can be found in table 4.1.

In the longitudinal direction, the acceptance of the electrons is restrained by the cyclotron motion as well (see section 4.2). As mentioned before, for integer numbers of the cyclotron time T_c , all transverse momenta are projected on the spectrometer axis, hence, the momentum information is lost. Due to the center hole of the electron detector the longitudinal momentum component $p_{z,e}$ experiences dead regions where no momentum information and, hence, no cross-section could be acquired. A better idea of the situation can be gained from Fig. 4.12. Here, the momentum space of the second electron for a single value of the acceleration field and magnetic field is plotted. The dotted line represents a constant energy E_{e2} for all polar angles θ_{e2} . Depending on the energy of the ejected electron (dotted-line), the area of no acceptance can be quite large and demands a method to fill these gaps. In its most simplistic form, a solution is to repeat the measurement at either a different magnetic field value B_z or a different field value U for the particle acceleration. Both alterations can shift the nodes along the p_z -axis and move them to cover regions that have had no acceptance in the previous setup. Since the projectiles are influenced by the magnetic field already on the way from the gun to the interaction volume and alteration would require a higher effort in refocusing the projectile beam the adopted method is to readjust the acceleration field. The combination of several measurements basically leads to total longitudinal acceptance of $-0.19\sqrt{2 E_z a_i} \lesssim p_{z,e} \leq p_0$ (in a.u.), where E_z is the acceleration field and a_i the ion's acceleration length.

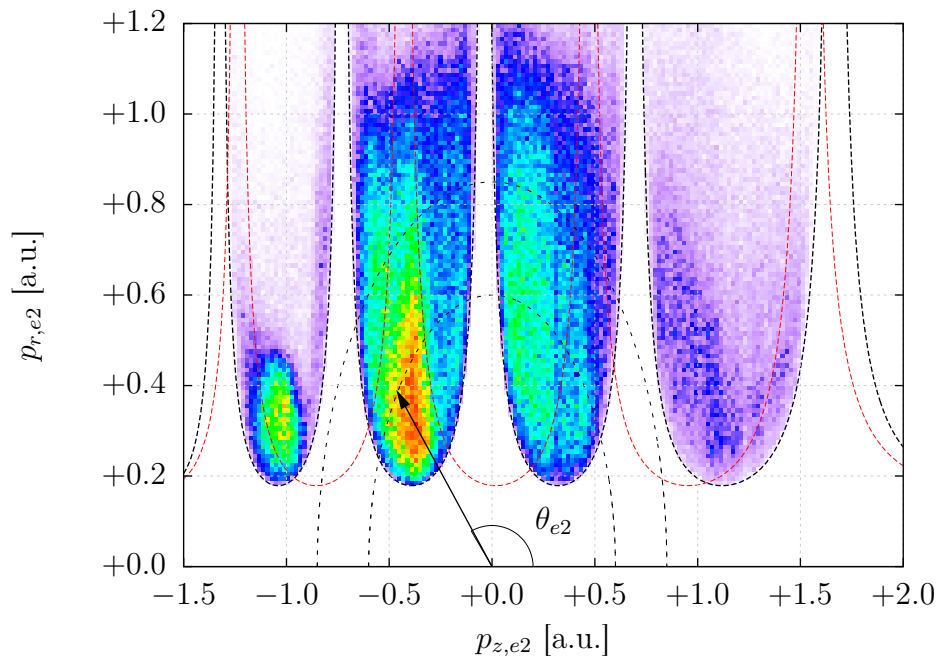


Figure 4.12.: Longitudinal vs. transversal momentum distribution of the ejected electron for a single value of the acceleration voltage. The dotted lines represent constant energies E_{e2} . The black and red-dashed lines depict the boundaries for detection acceptance for U_1 and $U_2 = U_1 + 7\text{V}$, respectively.

Ion Acceptance

The acceptance for ions it has to be distinguished, whether the target underwent only a single (or multiple) ionization event without further fragmentation (i.e., pure ionization) or whether the target subsequently coulomb explodes. In the latter case the fragments gain a significant amount momentum while the emission direction is isotropic, therefore, special measures have to be taken in such a reaction. First discussed will be the pure ionization case without coulomb explosion, afterwards the dissociative case will be considered.

To extend the acceptance in the longitudinal direction, the ion side of the spectrometer has been shortened with respect to older measurements (e.g. [Pflüger (2008)]) to a total length of 12 cm. With a maximum range of 50 μs for the TDC, the longitudinal acceptance can be expressed in terms of the maximum singly charged ion mass that is still detectable within this range. For the distances given in section 3.1 this leads to

$$m_{i,\text{max.}} [\text{amu}] = 75.4 \cdot E_z [\text{V/cm}] , \quad (4.10)$$

where $m_{i,\text{max.}}$ is the mass in atomic mass units and E_z is the acceleration field. Hence, for a field of $E_z = 1 \text{ V/cm}$ a theoretical mass of 75 amu could be detected.

For the radial acceptance the influence of the magnetic field can be safely neglected due to the large difference in mass with respect to the electrons. A simple calculation for a common experimental setting reveals a cyclotron time for singly-charged argon ions of $T_c = 2.9 \text{ ms}$. This value is four orders of magnitude larger than the respective electron T_c and at the same time close to 60-times larger than the range of the TDC. Hence, the transversal momentum acceptance is then given by

$$p_r \cdot \frac{t}{m} = r , \quad (4.11)$$

where t is the TOF. The maximum transversal momentum is acquired for $t = t(p_z = 0)$, which can be derived from (4.2) as

$$t(p_z = 0) = m \frac{2a + d}{\sqrt{2mqU}} \quad (4.12)$$

Hence,

$$p_{r,\text{max}} = r_{\text{Det.}} \frac{\sqrt{2mqU}}{2a + d} , \quad (4.13)$$

4. Data Processing and Analysis

species	E_z [V/cm]	$2a + d$ [m]	$p_{r,i}^{\max}$	$p_{r,i}^{\min}$	$p_{r,e}^{\max}$	$p_{r,e}^{\min}$	B_z [Gs]
Ar ⁺	1.36	0.44	25.8	3.2	1.32	0.17	8.21
	1.64	0.44	28.3	3.5			
	2.09	0.44	32.0	4.0			
Ne ⁺	3.08	0.16	46.4	5.8	1.46	0.18	9.07
	3.83	0.16	50.7	6.3			

Table 4.1.: Acceptance for pure ionization conditions. Minimum and maximum transversal momenta for different experimental conditions. The spectrometer length is $(2a + d)$, acceleration field E_z and magnetic field B_z . Empty cells hold same values as above. All momenta in a.u.

with $r_{\text{Det.}} = 40$ mm as the active MCP radius. Consequently, the maximum (minimum) transversal momenta are accumulated in table 4.1. Since (4.13) scales with \sqrt{m} , the corresponding maximum dimer ion acceptance is by a factor of 1.41 larger.

As indicated above, for the dissociation of a dimer into two charged fragments, considerable momentum can be transferred to the resulting fragments due to their large mass. For example, assuming a breakup at the equilibrium distance of $r_{\text{int.}} = 3.8$ Å for Ar₂ into two singly-charged argon ions, a momentum of $p_{\text{KER}} = 100.8$ a.u. for each ion is reached. This is considerably larger than what is expected for non-dissociative reactions and the corresponding spectrometer setting in table 4.1. Therefore, to gain full angular acceptance of the ionic fragments – even for an emission in the y -direction – the acceleration field has to be increased greatly. In this experiment one field value of $E_z = 17$ V/cm has been used. The downside of this procedure is that the increase of the acceleration field influences the resolution severely. Particularly, the electron resolution suffers under these high field values. A quantitative coverage will be given in the next section.

In general, for Coulomb explosion, the momentum of each fragment can be expressed as

$$p_{\text{KER}} = \sqrt{2 \frac{m_1 m_2}{m_1 + m_2} E_{\text{KER}}} . \quad (4.14)$$

The variables m_1 and m_2 correspond to the masses of the ionic fragments, while E_{KER} is the Coulombic energy of the two ions at the distance of the breakup which will be transformed into kinetic energy and a back-to-back emission of the ions along

their internuclear axis.

What follows is that the radial extension for an emission of the fragments under 90° as a function of the KER is

$$r(E_{\text{KER}}) = (2a + d) \sqrt{\frac{1}{q_1 U} \frac{m_2}{m_1 + m_2} E_{\text{KER}}}, \quad (4.15)$$

where E_{KER} is proportional to $R_{\text{int.}}^{-1}$, the inverse of the internuclear distance and the acceleration voltage is $U = E_z a$. The emission in the direction perpendicular to the spectrometer axis is considered here, since it illustrates the extreme case where all the energy goes to the transversal direction. Any other orientation of the dimer gives a better acceptance. Since (4.15) depends only on the charge of the fragment in mass-symmetric explosions, Fig. 4.13 shows the KER as a function of the radial acceptance for three exemplary acceleration fields: 17 V/cm (red), 15 V/cm (green) and 20 V/cm (blue). Therein, the continuous curves depict singly-charged fragments, while the dashed-curves doubly-charged ones. The horizontal arrows indicate the respective KER at the neutral internuclear distance of the argon dimer for the doubly-charged final state (labeled Ar_2^{2+}) and the triply-charged final state (labeled Ar_2^{3+}). For the breakup into two singly-charged ions (Ar_2^{2+}), both have an identical acceptance that is indicated by the vertical arrow that intersects the continuous curve at the respective KER. For the experimental value of $E_z = 17 \text{ V/cm}$, this is $r_{\text{max}} = 26.9 \text{ mm}$. For the triply-charged final state (Ar_2^{3+}) the charge is, of course, not distributed equally among the two fragments. As a consequence, they have different acceptances according to their charges. The corresponding KER at 7.7 eV intersects with the continuous red curve at $r_{\text{max}} = 37.9 \text{ mm}$, which gives the maximum radius for the singly-charged fragments. The intersection with dashed-red curve, i.e., for the doubly-charged fragments, is at exactly the same position as for the fragments of the doubly-charged final state (26.9 mm). Therefore, it can be inferred that the higher charged fragments in a non-symmetrical explosion have always the same acceptance, whereas the fragments with the lower charge have an increasingly worse acceptance.

Compared to the values for the acceleration field in table 4.1, those for dissociation need to be considerably larger. With the value chosen for this experiment, it is possible to get full acceptance for the triply-charged final state. Table 4.2 gives an overview of the maximum and minimum momentum values in the transverse

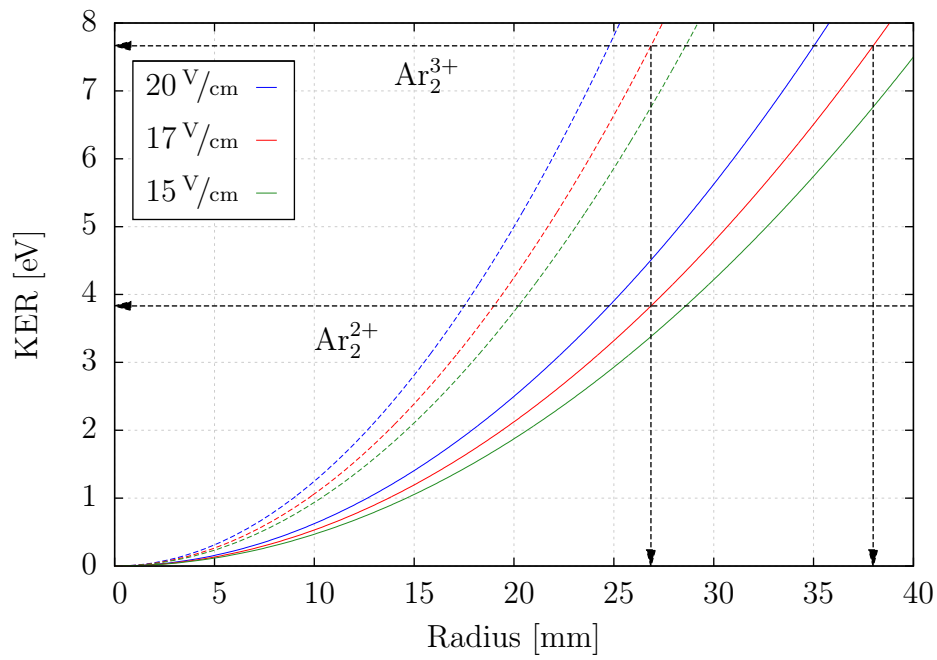


Figure 4.13.: KER as a function of the radial detection position for argon dimer breakup. The color coding denotes different acceleration fields. The continuous curves are singly-charged fragments, the dashed-curves doubly-charged fragments. The arrow Ar_2^{2+} indicates the KER for a doubly-charged final state, Ar_2^{3+} for a triply-charged final state. The vertical arrows denote the radial position at the respective intersection with the KER function.

species	E_z [V/cm]	$2a + d$ [m]	$p_{r,i}^{\max}$	$p_{r,i}^{\min}$
Ar ⁺	17.0	0.16	151.1	15.1
Ar ²⁺			213.7	21.4

Table 4.2.: Momentum acceptance for Coulomb exploding argon cluster fragments. The spectrometer length is $(2a + d)$, acceleration field E_z . All momenta in a.u.

direction for different charge states for an acceleration field of $E_z = 17$ V/cm. For the minimum value, resulting from the central hole in the detector, it has to be considered that the target jet creates a momentum offset in the $-y$ -direction (cf. section 3.3). Given the determined velocity, for argon this amounts to 17 a.u. at the least. As a consequence, the distribution is shifted with respect to the hole, reducing the maximum acceptance and increasing the minimum acceptance.

4.5.2. Resolution

The momentum resolution of a particle in the spectrometer can be split into the longitudinal and transversal direction. Additionally, the error in the azimuthal angle has to be considered. While the error in the spectrometer geometry does not change throughout an experiment, the acceleration length is introduced to a statistical component due to the finite width of the target. This error can be minimized by applying time-focusing (see section 3.1) which is an analytical expression for the relation between the acceleration length a and the drift length d . In this work, time focusing is maintained for electrons and ions simultaneously. Hence, the uncertainty in the longitudinal direction depends only on the time

$$\Delta p_z = \sqrt{\left(\frac{\partial p_z}{\partial t} \Delta t\right)^2} = \frac{1}{\frac{\partial t}{\partial p_z}} \Delta t. \quad (4.16)$$

For the transversal direction, equations (4.6) and (4.7) give the remaining errors

$$\Delta p_r = \frac{\omega_c m}{2|\sin(\omega_c t/2)|} \sqrt{\Delta r^2 + \left(\frac{\omega_c r}{2 \tan(\omega_c t/2)} \Delta t\right)^2} \quad (4.17)$$

and

$$\Delta\phi = \sqrt{\left(\frac{\Delta r}{r}\right)^2 + \left(\frac{\omega_c}{2}\Delta t\right)^2}, \quad (4.18)$$

for the transversal momentum and the azimuthal angle, respectively. Finally, the error for the polar angle θ and the energy E can be derived from p_z and p_r :

$$\Delta\theta = \frac{1}{p_r^2 + p_z^2} \sqrt{(p_z \Delta p_r)^2 + (p_r \Delta p_z)^2}, \quad (4.19)$$

$$\Delta E = \frac{1}{m} \sqrt{(p_r \Delta p_r)^2 + (p_z \Delta p_z)^2}. \quad (4.20)$$

Here, ω_c is the cyclotron frequency introduced in (4.3). In Fig. 4.14, these errors are plotted as a function of the electron momentum. In this plot only those momenta are accounted for, where the acceptance is given under the specific experimental settings. In particular, the acceleration field is $E_z = 1.63 \text{ V/cm}$ and the cyclotron time is $T_c = 43.5 \text{ ns}$. From panel (a) it is apparent, that the error in the transversal momentum component increases rapidly at the edges of the acceptance region and, on top of that, with increasing magnitude of $p_{r,e}$. The error in the azimuth in panel (b) shows an increasing error with decreasing transversal momentum. This behavior, to some extent, affects the scattered projectile which is used to define the scattering plane.

The error of the polar angle – plotted in Fig. 4.15 – and the energy are of particular importance. In the common representation, the triply-differential cross-section is represented as a function of θ_{e2} with fixed E_{e2} (see section 4.6). It is, however apparent, that – for this spectrometer setting – the largest error is again confined to the edges of the wiggles. For the acquisition of the 3DCS, conditions are used that omit these border regions. This can be conveniently done reducing the statistics or the acceptance significantly since several measurements are overlapped (see Fig. 4.19). In Fig. 4.7 a energy sum spectrum ($E_{\text{sum}} = E_{e1} + E_{e2} = E_0 - Q$) is presented for the electron impact ionization of neon with a projectile energy of 61 eV. The fit performed gives a fwhm of 6.50(7) eV. The width of the energy sum is a good measure for energy resolution of the setup and in this case reaches a satisfactory value. For the second experiment reported here, the ionization of argon at 100 eV, the fwhm of the energy sum is 8.54(23) eV. The higher value is mainly due to the higher projectile energy. A plot of the corresponding spectra is shown in section 5.1.1 for the

various cluster targets.

The measured momentum resolution for the ions can be presented in terms of the momentum sum $p_{k,\text{sum}} = p_{k,e1} + p_{k,e2} + p_{k,r}$ of all three charged fragments in a single ionization event. In Fig. 4.16 these components are plotted for ionization of neon with a projectile energy of $E_0 = 61$ eV. Additionally, the data are fitted to access the fwhm of the respective distributions. As expected, the y -direction has the worst resolution since it coincides with the propagation direction of the target expansion. Perpendicular to this direction, the momentum distribution is additionally confined by skimmers (cf. section 3.3). The longitudinal direction experiences the best resolution with a fwhm of 0.42 a.u. which is mainly due to the fact that, according to (4.16), the error depends only on the precision of the TOF measurement and because for this work, time-focusing was maintained for ion side of the spectrometer.

Overall, the resolution is limited mainly because of the large mass of (in this case) neon. The general behavior of the spectrometer's momentum resolution is depicted in Fig 4.17. It shows the transversal resolution is plotted as a function of the mass showing a dependence like $\Delta p_{r,i} \propto \sqrt{m}$. The momentum was chosen to be $\vec{p}_i = 0$. While in general, (4.17) is a function of the momentum components p_z and p_r , for ions from pure single ionization the dependence on a typical scale is, however, very small compared to the total value. Apparently, going from H_2 with a mass of 2 amu to atomic argon with 40 amu $\Delta p_{r,i}$ increases by roughly 40 % while in the longitudinal direction hardly any dependence is observable.

Table 4.3 presents the Cartesian momentum resolution components of all fragments for the pure single ionization experiments are collected. In it are the values for the single ionization experiment on argon with a projectile energy of 100 eV (denoted Ar^+) and on neon at a lower projectile energy of 61 eV (denoted Ne^+) for one exemplary acceleration field, respectively. The spectrometer resolution for the electron and the ion are calculated (Δp^{sp}) while $\Delta p_{k,\text{sum}}$ is the measured momentum sum distribution, according to Fig. 4.16. Since the momentum sum incorporates the errors of the particles, the thermal momentum resolution of the ions can be extracted ($\Delta p_{k,i}^{\text{th}}$). It shows that the momentum sum widths to the most extent are due to thermal resolution and by that to the initial temperature. Furthermore, this point has been stressed before, it shows that, consequently, the resolution in the direction of the jet (i.e., the y -direction) is the lowest, while the in the TOF

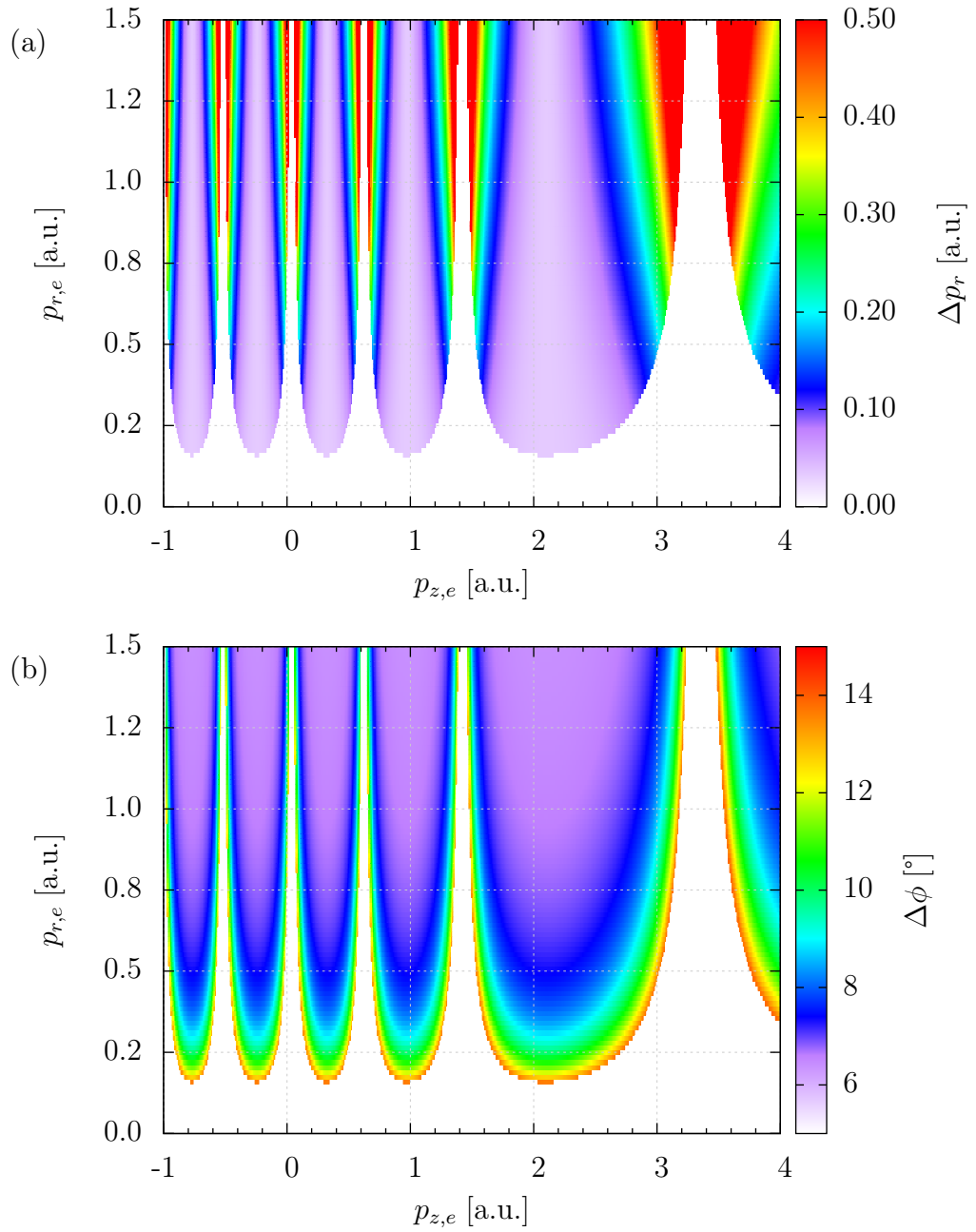


Figure 4.14.: Momentum acceptance and resolution for electrons with an acceleration field of $E_z = 1.63 \text{ V/cm}$ and a cyclotron time $T_c = 43.5 \text{ ns}$. (a) Radial momentum resolution as a function of the electron momentum. (b) Angular resolution for the azimuth ϕ as a function of the electron momentum.

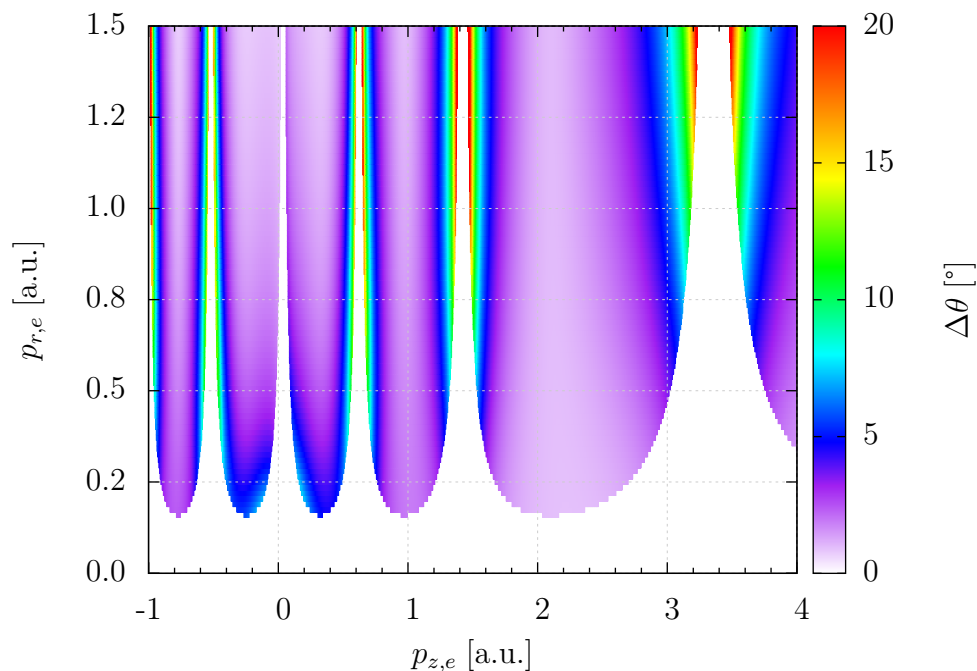


Figure 4.15.: Resolution for the polar angle θ as a function of the electron momentum. Conditions are identical to those in Fig. 4.14.

direction (i.e., the z -direction) it is the highest due to the high precision of the time measurement.

Additionally, the temperature of the jet can be determined. In section 3.3, particularly low values for the temperature in the propagation direction have been determined. The thermal resolution in jet direction $\Delta p_{y,i}^{\text{th}}$ is connected with temperature by (3.9) in section 3.3. The determined temperatures, with 2.79 K for argon and 3.43 K for neon are, in some sense, expectedly higher than the values in table 3.1. The optimal conditions assumed by the calculation are obviously not met in the experiment, however, the temperatures reached are sufficiently low.

As mentioned before, the high acceleration field needed to detect Coulomb exploding clusters need to be much higher and, consequently, the resolution gets worse. This effects the electrons to a great deal and the resulting resolution is summarized in table 4.4.

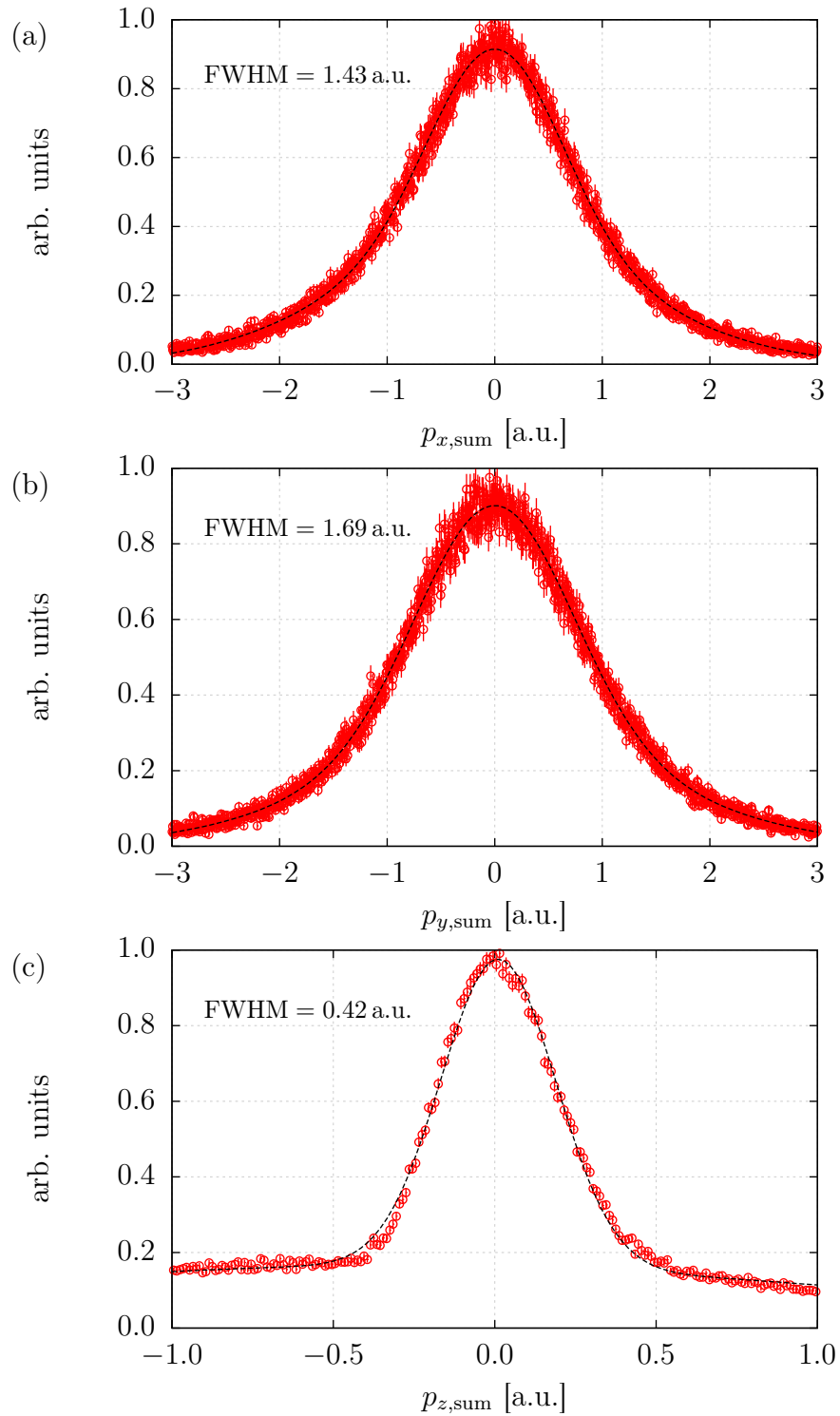


Figure 4.16.: Sum momentum distributions for single ionization of neon with a projectile energy of $E_0 = 61$ eV for all Cartesian components.

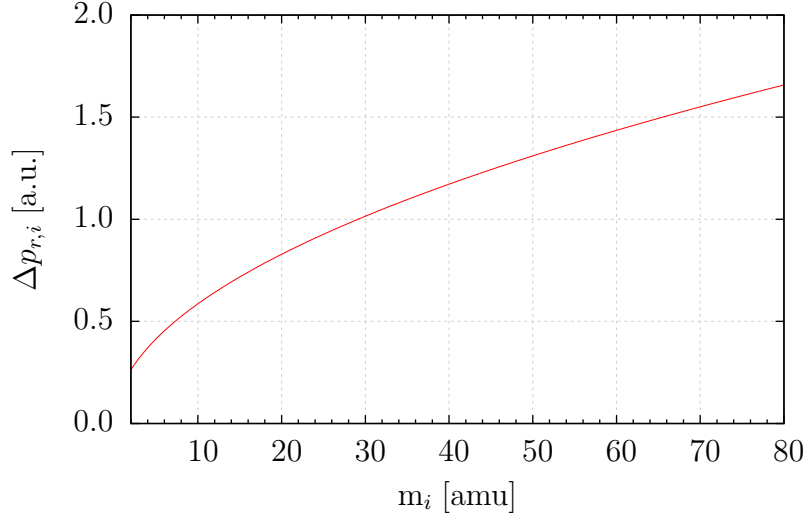


Figure 4.17.: Transversal momentum error $\Delta p_{r,i}$ as a function of the fragment mass plotted for $\vec{p}_i = 0$.

species	E_z [V/cm]	k	$\Delta p_{k,\text{sum}}$	$\Delta p_{k,e1}^{\text{sp}}$	$\Delta p_{k,e2}^{\text{sp}}$	$\Delta p_{k,i}^{\text{sp}}$	$\Delta p_{k,i}^{\text{th}}$	T_f [K]
Ar ⁺	1.64	x	1.36	0.03	0.25	0.50	1.24	2.79
		y	1.97	0.03	0.25	0.50	1.89	
		z	0.43	0.07	0.02	0.01	0.42	
Ne ⁺	3.08	x	1.43	0.13	0.03	0.80	1.18	3.43
		y	1.69	0.13	0.03	0.80	1.48	
		z	0.42	0.02	0.03	0.04	0.42	

Table 4.3.: Accumulated momentum resolution for the pure single ionization setup. Ar⁺ denotes the experiment with 100 eV projectile energy, while Ne⁺ the 61 eV. The column $\Delta p_{k,i}^{\text{th}}$ shows the thermal resolution resulting from the jet temperature T_f , Δp^{sp} denotes the calculated spectrometer resolution. All momenta in a.u.

E_z [V/cm]	k	$\Delta p_{k,e1}^{\text{sp}}$	$\Delta p_{k,e2}^{\text{sp}}$	$\Delta p_{k,i}^{\text{sp}}$
17	x	0.21	0.07	2.61
	y	0.21	0.07	2.61
	z	0.22	0.21	0.21

Table 4.4.: High field momentum resolution of the electrons for the dissociative ionization setup. The ion resolution has been determined for zero momentum. All momenta in a.u.

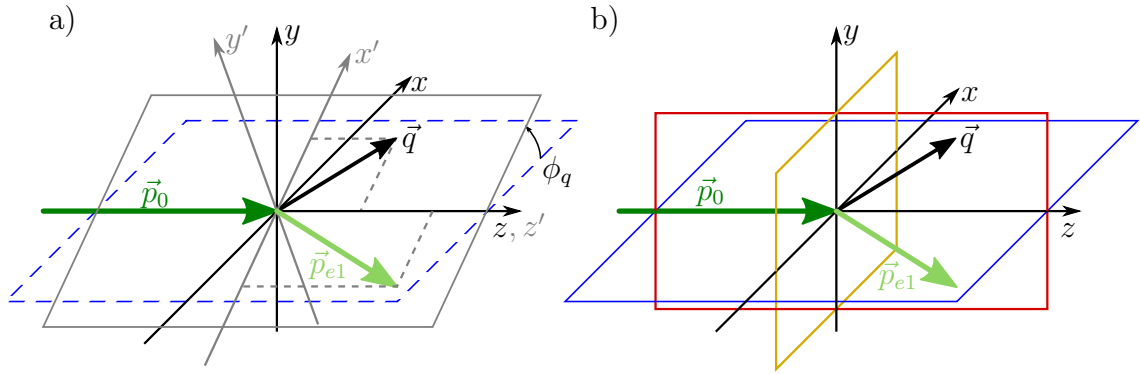


Figure 4.18.: Scattering geometry. (a) Each event defines a coordinate system (gray) different from the lab system (black). (b) Planes defined in the lab system: scattering plane (blue), perpendicular plane (red) and full-perpendicular plane (yellow).

4.6. Triply-Differential Cross-Section

After all momenta of an event have been calculated the complete information of this particular ionization reaction has been acquired. In the subsequent steps this information is used to find 3DCSs. First, due to the isotropy towards the ϕ -angle the scattering geometry has to be defined. Although the final state electrons are in principle indistinguishable, still a selection has to be made which of the two is the *first* and which the *second* electron. One way to do this is by selecting them by their TOF – this way the first is literally the first electron to reach the detector. For high energetic collision this is a valid selection since for the projectile is very unlikely to loose a significant amount of its energy and at the same time the most probable scattering angles are small. For intermediate to low energies, however, a situation can occur where the projectile does scatter at a large angle leaving it with a small longitudinal momentum. If the ejected electron is emitted towards the electron detector it can – even though it has a lower energy – have a larger longitudinal momentum and, hence, arrive earlier at the detector. As a consequence, the acceptance for emission in the direction of the electron detector is severely limited. The adopted method, therefore, makes use of the momentum information and orders the electrons by descending energy. In this way, the *first* electron is the one with the highest energy.

The basic coordinate system for a scattering event is depicted in Fig 4.18(a).

We define the primary plane – the *scattering plane* – as the one that is created by $(\vec{p}_0, \vec{p}_{e1})$ (depicted in gray). Since the distribution of electrons is isotropic with respect to the azimuthal angle ϕ_{e1} , each event defines a new scattering plane. The coordinate system, on the other hand, is fixed to the laboratory system. We define a fixed scattering plane – w.l.o.g. – to be the (x, z) -plane (depicted in blue). For every event, all momentum vectors are now rotated with respect to the z -axis, making the scattering plane $(x, z)'$ to coincide with the fixed laboratory plane (x, z) . This can be conveniently done in terms of the *momentum transfer* $\vec{q} = \vec{p}_0 - \vec{p}_{e1}$ – which lies in the $(x, z)'$ -plane, too – rotating by $-\phi_q$. That this can be done is one advantage, making the REMI significantly more efficient than a conventional $(e, 2e)$ -spectrometer, where the setup already defines a fixed scattering plane.

Additionally, we define the plane with $\phi = 90^\circ$, which is perpendicular to the scattering plane but contains \vec{p}_0 , to be the *perpendicular plane* (red in Fig. 4.18(b)) and the plane perpendicular to \vec{p}_0 to be the *full-perpendicular plane* (yellow).⁷

The general procedure for acquiring 3DCSs is as follows: after an event the coordinate system defined by \vec{p}_{e1} is rotated to the laboratory system. The event is then sorted with respect to the scattering angle of the first electron θ_{e1} and the energy of the second, E_{e2} . This is done because the 3DCS is a function of the final state solid angles Ω_{e1}, Ω_{e2} and E_{e2} . These, however, are not independent of each other due to energy and momentum conservation. For a fixed projectile momentum, ϕ_{e1} is always fixed to 180° . Still left are the scattering angle θ_{e1} and the ejection energy E_{e2} that can be independently chosen. Under these premises, the angular distribution ϕ_{e2}, θ_{e2} represents the 3DCS. Since this is a three-dimensional distribution, ϕ_{e2} or θ_{e2} can be fixed with respect to the previously defined planes and the two-dimensional distributions can be extracted. Although, in the experiment the complete solid angle is detected and thereby all possible planes, cutting through a 3D cross-section is important to gain the possibility for a quantitative comparison between data sets and theory.

What is finally presented as 3DCS is either the number of counts as a function ϕ_{e2}, θ_{e2} for fixed E_{e2} and Ω_{e1} in the 3D case or with an additionally fixed ϕ_{e2} to any of the previously introduced planes in the 2D case.

A crucial point in the construction of the differential cross-sections is related to

⁷The full-perpendicular plane could, of course, be dubbed azimuthal plane since it effectively contains the information ϕ_{e2} .

the acceptance as explained before (section 4.5). Figure 4.12 shows the calculated acceptance for the current acceleration voltage U_1 (black-dashed) and the acceptance for $U_2 = U_1 + 7\text{ V}$ (red-dashed). While a large part of the previously undetectable area can now be covered, a problem arises in terms of statistical significance. For the second measurement, in principle, the same total time is needed to gain the same amount of total counts. If, however, only the gaps are filled, less than 10 % are actually used, while the rest of the data is thrown away. Therefore, a more efficient method was invented to combine different measurements to maximize the area of acceptance. Instead of only taking data points where there was no acceptance for the previous setup, all data points are used. For a measurement with three different acceleration voltages this results in regions of the momentum space where only the current setup has acceptance, regions where two areas of acceptance overlap and, of course, regions where all three measurements overlap. It is now required to normalize all areas to account for the number of counts. Therefore, seven parameters are needed: three for single acceptance, three for double acceptance and one for triple acceptance.⁸ Finding the parameters can be done by projection of horizontal (i.e. parallel to the x -axis) and/or radial cuts of the momentum space. Radial cuts have the advantage that they represent constant energies of the second electron and are therefore closer to the actual 3DCSs. Since, for the most part, the boundaries between the areas are vertical (i.e. parallel to the y -axis), horizontal cuts are easier to create smooth transitions.

In order to simplify this problem Fig. 4.19 depicts the situation for two different measurements with the respective acceleration voltages U_1 in blue and U_2 in red. The area where both settings have acceptance is depicted in green. As one can see, the largest area is covered by both measurements and yields the highest statistical significance.

⁸For three measurements 1,2 and 3 these are: $(\mathcal{S}^1, \mathcal{S}^2, \mathcal{S}^3), (\mathcal{S}^{12}, \mathcal{S}^{13}, \mathcal{S}^{23}), (\mathcal{S}^{123})$.

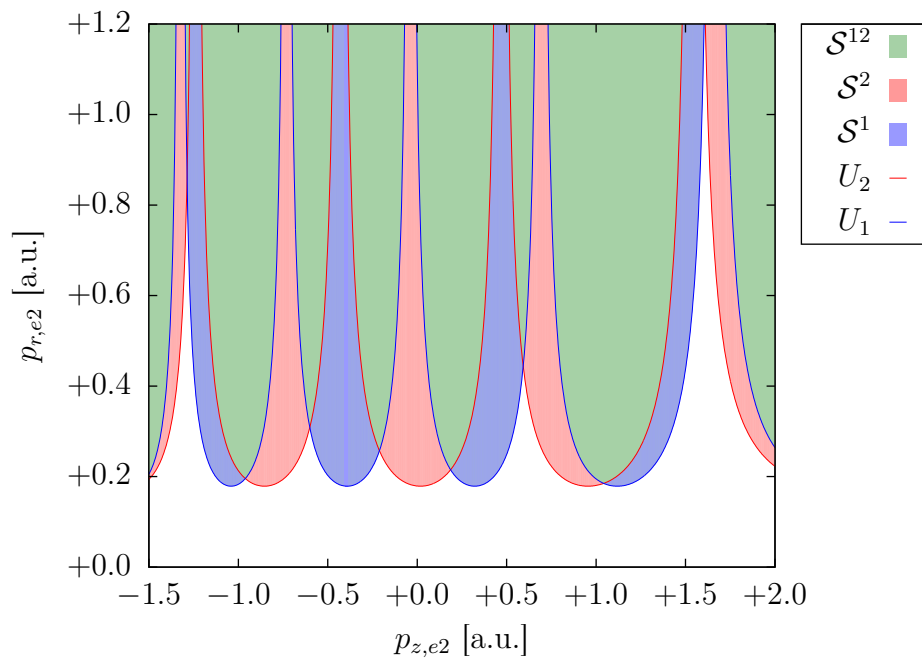


Figure 4.19.: Acceptance regions for two different measurements with the respective acceleration voltages U_1 and U_2 . The green-shaded areas mark the regions where the two overlap.

5. Results

In the following sections two different kinds of experiments will be reported. On one hand, classical $(e, 2e)$ measurements were performed on argon dimers at a projectile energy of 100 eV (section 5.1.1) and on neon dimers at 61 eV. As it has been described in section 2.1, this type of experiment involves the coincident detection of two electrons. Additionally, it is of crucial importance to detect the ionic fragment. Because of the technique used to prepare the target (section 3.3), the interaction volume is contaminated with – depending on the properties of the expansion – a variety of cluster sizes of the used gaseous species. While the ion created in a collision usually serves as a trigger and for reduction of background noise, it was used here also to identify the target species of interest. By doing so it was made possible to perform measurements on different cluster sizes of the same target in the same run of the experiment. Additionally, it was possible distinguish between the creation of a dimer ion by ionization of a neutral dimer and by dissociation of a small cluster. As a result, single ionization of the atomic as well as the dimer species could be acquired under identical experimental conditions and, hence, under identical systematical uncertainties. Throughout this section, ionization processes where the target does not dissociate will be referred to as *pure* ionization.

The other type of experiment involved ionization of the rare gas dimer into two charged fragments by electron impact ionization, followed by Coulomb explosion (section 5.2). Here, the two resulting ionic fragments are recorded in coincidence with one electron. Since, depending on the final charge state, at least three final state electrons are associated with the ions combined with low cross-sections, a kinematically complete measurement is not feasible due to the enormously increased runtime to gather enough data. However, insightful information about the ionization process can be obtained by studying the Coulombic energy distribution of the dissociation also known as the kinetic energy release (KER). From the momentum information of the ions, the alignment of the dimer at the moment of ionization

could be retrieved and set in relation with the KER.

5.1. Single Ionization of Rare Gas Dimers

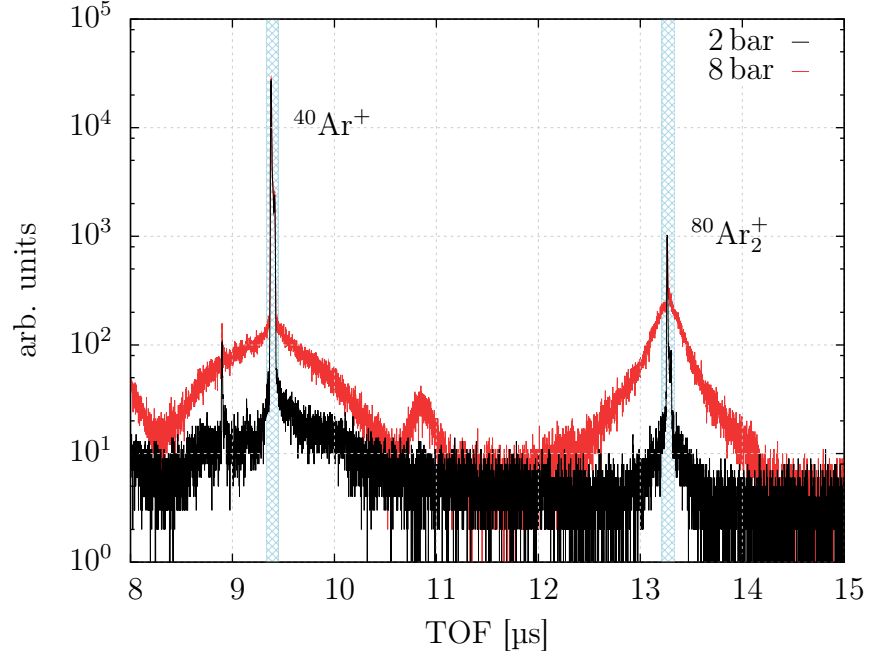


Figure 5.1.: TOF spectrum for argon ions. The stagnation pressure of the gas jet was $p_0 = 2$ bar (—, black) and $p_0 = 8$ bar (—, red) at $T_0 = 300$ K. The blue-hatched regions depict the pure ionization of the respective neutral species.

Two TOF spectra for electron impact ionization of argon are shown Fig. 5.1. The stagnation pressure of the supersonic jet was $p_0 = 2$ bar (black) and $p_0 = 8$ bar (red) at room temperature. The narrow peak structures (blue-hatched regions) indicate the pure single ionization the respective neutral target species. Meaning, the peak on the right marked $^{80}\text{Ar}_2^+$ results from the single ionization of a neutral $^{80}\text{Ar}_2$ dimer, while the peak on the left marked $^{40}\text{Ar}^+$ is from ionization of argon atoms. Focusing on this dimer ion peak, apart from the narrow line shape a broad structure is superimposed. This structured background originates from the amount of small clusters contained in the jet. As was described before in section 2.3, the size distribution of the clusters created in during the expansion is log-normal and has a

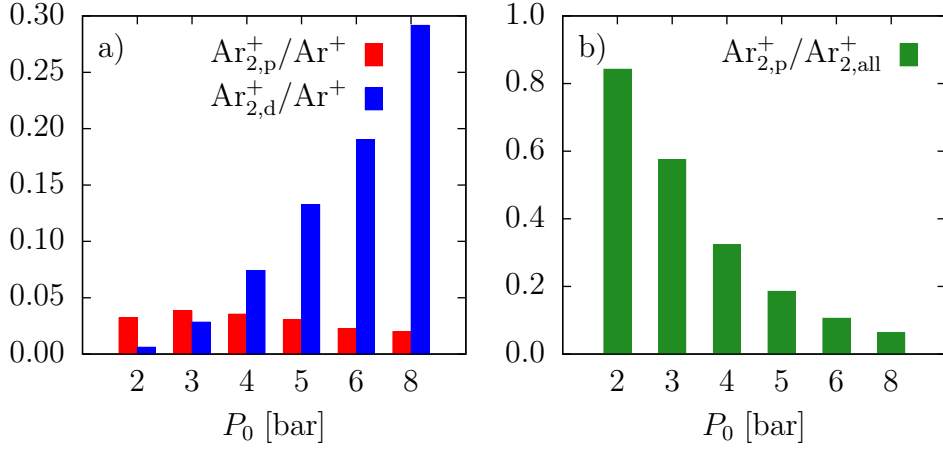


Figure 5.2.: a) Relative abundance of dimer ions from pure ionization $\text{Ar}_{2,p}^+$ and dimer ions originating from small cluster dissociation $\text{Ar}_{2,d}^+$ compared to pure monomers Ar^+ for varying stagnation pressures p_0 . b) Relative abundance of dimer ions from pure ionization compared to all dimer ions.

considerable width. Consequently, the more clusters that are contained in the gas target the more dissociative products emerge from their ionization. This is due to the fact that rare gas clusters are highly unstable upon ionization and dissociate almost exclusively. Since, for argon, the most abundant ionic fragmentation product is the dimer ion, the amount of small clusters that are contained in the jet can be observed directly by the ratio of pure ionization to structured background. The reason for the broadening of the peak for the ions emerging from dissociation lies in the fact that they are created in a vibrationally excited state of the respective ion and gain considerable kinetic energy upon dissociation. In the additionally plotted data set with a stagnation pressure of $p_0 = 8$ bar (red), the broad background underneath the pure ionization peak has grown to approximately 75 % in height relative to the total intensity, indicating an increase of the size distribution in favor of small clusters of various sizes with respect to dimers.

To quantify this behavior, a series of measurements between 2 bar and 8 bar stagnation pressure for argon were performed at an initial temperature of $T_0 = 300$ K. The ratios of the pure dimer ion yield $\text{Ar}_{2,p}^+$ and the dissociative dimer ion yield $\text{Ar}_{2,d}^+$ to the pure atomic ion yield for the respective stagnation pressures were calculated

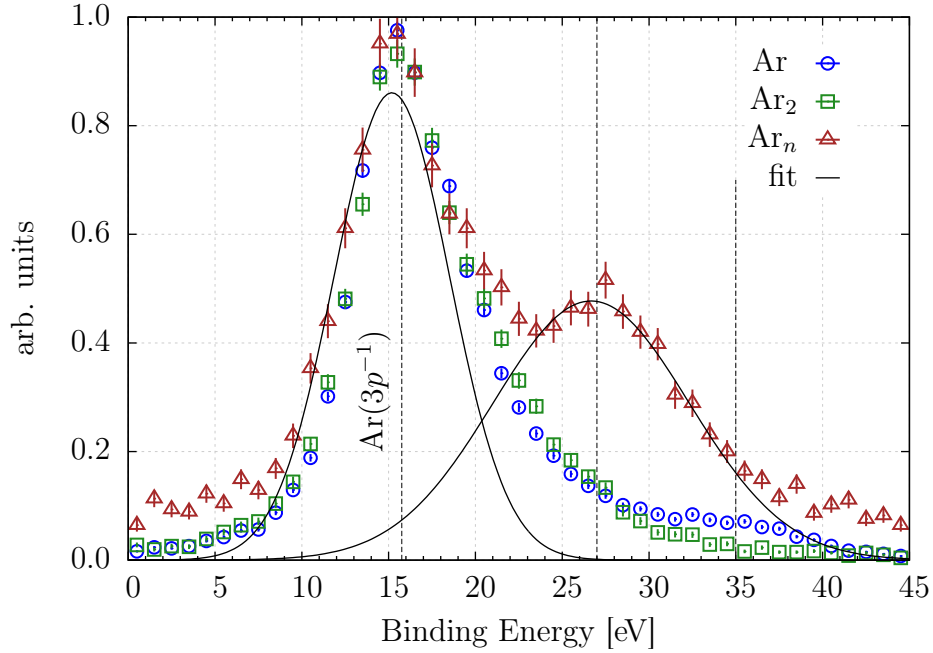


Figure 5.3.: Binding energy spectrum E_b for pure ionization of argon monomers (\circ , blue) and dimers (\square , green) as well as for the ionization of small argon clusters that dissociate into dimer ions (\triangle , red).

and are shown in Fig. 5.2(a). While a step increase in the relative yield for dimer ions from dissociation with the stagnation pressure can be seen, the dimer ion yield from pure ionization actually decreases. This indicates that the amount of neutral dimers in the jet decreases with increasing pressure in favor of small clusters, which – in turn – dissociate mostly into dimer ions. The abundance of pure dimer ions $\text{Ar}_{2,p}^+$ relative to all dimer ions $\text{Ar}_{2,\text{all}}^+$ as a function of p_0 is depicted in Fig. 5.2(b). It shows a very step decrease with increasing pressure again indicating the increasing amount of ions resulting from dissociation. From 2 bar to 4 bar the pure dimer abundance already dropped by more than 50%. Consequently, the adopted pressure in the experiment was kept as low as possible to maximize the pure dimer ion count rate while still maintaining a reasonable total count rate.

5.1.1. Argon

Single ionization on argon atoms, dimers and clusters at a projectile energy of 100 eV was performed [Pflüger et al. (2011)]. The corresponding binding energy spectra can

be seen in Fig. 5.3. They show – in contrast to the energy sum spectrum (e.g. Fig. 4.7) – the difference of the projectile energy and the energy sum of the outgoing electrons $E_b = E_0 - E_{\text{sum}}$ for all accessible target species. These were in the following: pure ionization of atomic argon (blue), pure ionization of argon dimers (green) and ionization of small clusters (red). As explained above, the detected ions for the two latter reactions are both dimer ions.

All data show the same peak at ~ 15.8 eV which corresponds to the $3p$ ionization of atomic argon.¹ An indication for $3s$ ionization, which lies 13.48 eV above the the first ionization potential of 15.76 eV, can not conclusively be identified.² It should, however, be noted that at the stated projectile energy, the partial cross-section for $3s$ ionization in argon is roughly an order of magnitude smaller than for $3p$ ionization [Bartlett and Stelbovics (2002)]. Furthermore, both the data for monomers and small clusters show additional features whereas non could be found for the dimer data. An additional peak structure for the monomers is located at 35 eV and corresponds to an additional excitation in the monomer ion $Ar^{+*}(3p^{-2}nl)$, where one valence electron is removed and another one is excited to a Rydberg state. Possible states include $3s^23p^44s$, $3s^23p^43d$ and $3s^23p^44p$ which, effectively, form a band of target states. The same band should also exist in the dimer given its weak binding energy and large internuclear distance (see Fig. 2.5). The absence of a similar structure for the dimer indicates, however, that the corresponding state is either repulsive or leads to predissociation of the excited dimer ion. This presents an indication, as was discussed in section 2.3.1, that such a process might also be subject of ICD that proceeds through an excited state of the argon dimer. From the data alone no distinctive proof can be given. However, following the potential curves of the excited states, a number of states exist above the Ar_2^+ IP that are prone to ICD leading to two singly charged argon ions (see Fig. 2.7).

In small clusters, on the other hand, a dissociative process is needed to create the observed dimer ions in the first place. Their binding energy spectrum in Fig. 5.3 shows a strong contribution of additional energy loss in the order of 50 % of the main peak and about 12 eV above the first ionization potential. In a small cluster, given the number of constituents, the possibility for an additional arbitrary scattering process is greatly enhanced compared to a dimer. As such, the peak coincides with

¹The configuration of argon is $[Ne]3s^23p^6$.

²All values from [Ralchenko et al. (2011)].

the excitation of a neutral argon atom to $3s^23p^54s$. A process like that would involve either the scattered projectile or the ejected electron to scatter at another constituent of the cluster and effectively break the angular correlation between the two final state electrons leading to an isotropic differential cross-section. Hergenbahn et al. conducted a photoionization experiment with neon and argon, where in contrast to the work reported here, not the final ionic state was fixed but the initial target state was distinguished in terms of “gas phase” for atoms or “cluster” [Hergenbahn et al. (2002)]. Their photoelectron spectra reveal increasing energy loss to the target starting, in the case of argon, slightly below 30 eV and is attributed to the excitation of a neutral constituent of the cluster by an outgoing electron. Similar experiments involving electron impact studying these excitonic states have been carried out by Foltin et al. [Foltin and Märk (1991)].

Due to significantly reduced target density for the small clusters, differential cross-sections which examine the dynamical properties of the respective ionization process had to be integrated over a certain range in ejection energy and scattering angle to obtain statistically significant datasets. Specifically, the scattering angle was integrated from $\theta_{e1} = -4^\circ$ to -20° , while the ejection energy from $E_{e2} = 1.5$ eV to 20 eV. In Fig. 5.4(a)-(c) the differential cross-sections for all planes introduced in Fig. 2.4(b) are depicted, where (a) represents the scattering plane, (b) the perpendicular plane and (c) the full-perpendicular plane. The compared reactions are the pure ionization of monomers (\circ , blue), small clusters (\triangle , red) and ionization plus excitation in small clusters (∇ , green). In addition to the cuts, the 3D cross-sections are depicted for (f) monomers, (e) small clusters and (d) excited clusters. Discussing the cross-section cuts (a)-(c) first, to make the data comparable, a normalization procedure had to be adopted to compensate for the difference in target density and the consequential difference in total counts. Other than the common practice³, it has been chosen to normalize the total number of counts of the respective 3D cross section of each data set to the same value, meaning, the integrated number of counts over the complete 4π solid angle for the respective kinematical condition. The normalization between the cuts is fixed by the experiment in the sense that all possible planes are detected simultaneously. This relation is not changed by the normalization procedure since the acquired factors are applied to all cuts.

³A common practice in the field of ($e, 2e$) experiments to make data comparable with calculations is to normalize the data to the maximum of the binary peak.

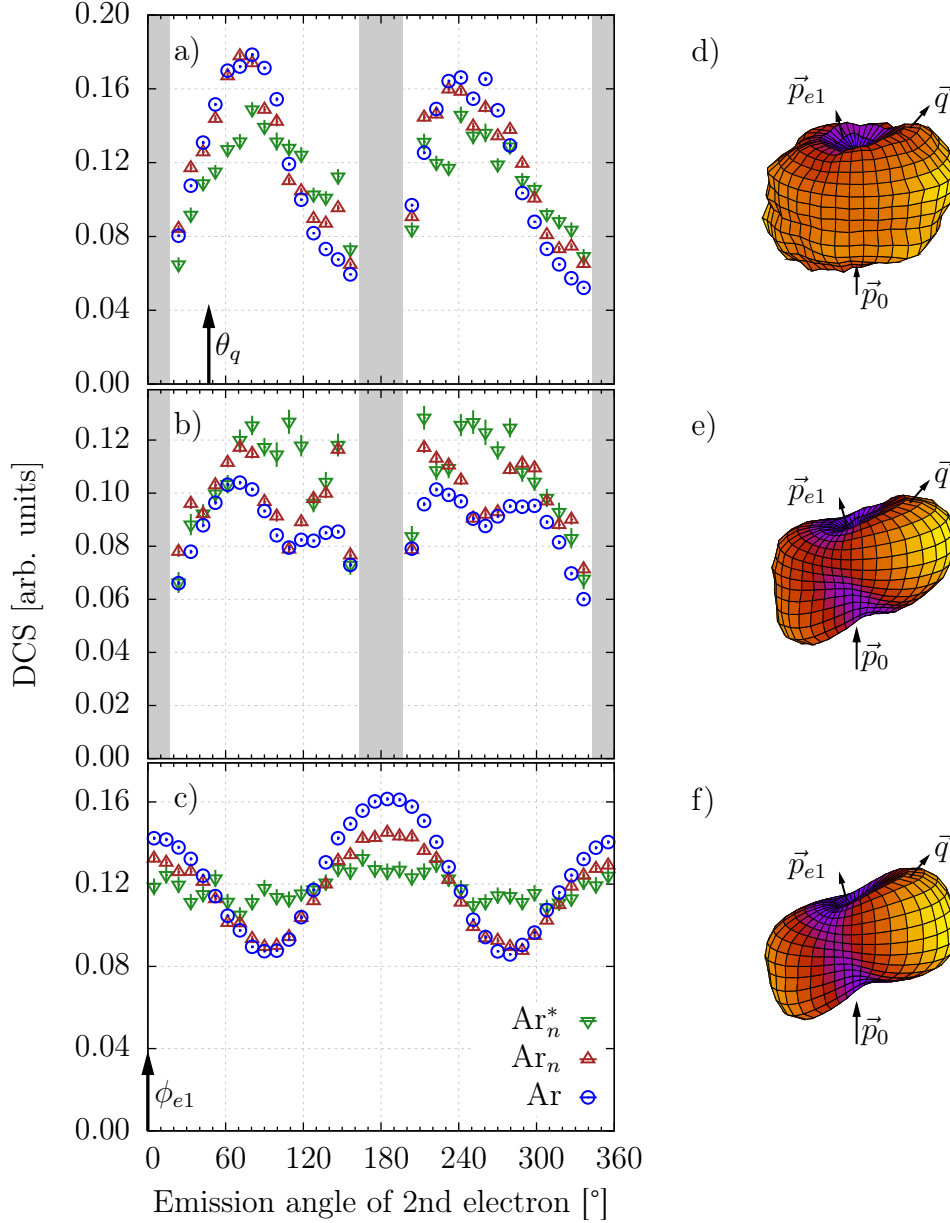


Figure 5.4.: Differential cross-section for pure ionization of argon monomers (\circ , blue) and small clusters (Δ , red) as well as for the ionization plus excitation of small argon clusters that dissociate into dimer ions (∇ , green). The projectile energy is 100 eV. The scattering angle was $\theta_{e1} = -4^\circ$ to -20° , the ejection energy $E_{e2} = 1.5$ eV to 20 eV. (a) shows the scattering plane, (b) the perpendicular plane and (c) the full-perpendicular plane. (d)-(f) shows the respective 3D cross-section for (f) monomers, (e) small clusters and (d) ionization plus excitation of small clusters.

The obvious advantage of the adopted procedure is that differences between data sets can be directly assigned a quantitative preference of ejection direction since it implies that additional neighboring atoms in dimers or small clusters only change the directions of the outgoing electrons.⁴ Fig. 5.4(a) now shows an increasing intensity in the direction of the scattered projectile (i.e. 340° to 356°) for small clusters compared to monomers. The reason for the suppression in monomers – even at this moderate projectile energy – is largely due to PCI, which is partly screened by the cluster. For the channel where additional excitation takes place, a strong broadening of the peak structures can be observed. This is a further indication to the previously stated assumption of a strongly isotropic distribution in this case. A better way of examining the effects of additional scatterers is, of course, to probe for higher-order effects that effectively enhance the probability of out-of-plane emittance of the ejected electron (see section 2.1). Therefore, in (b) the differential cross-section for perpendicular plane is depicted. Here, the ionization plus excitation channel shows a strong enhancement over the pure monomer channel. Interestingly, even the pure small cluster data shows a significant increase over the monomer indicating the effect of the cluster elastically scattering electrons to planes other than the scattering plane. The most apparent feature of the rescattering process, however, can be seen in (c), the full-perpendicular plane. The ionization plus excitation channel exhibits a nearly perfect isotropic distribution while the pure channel still maintains – though reduced – the binary/recoil structure.

For a better qualitative understanding Fig. 5.4(d)-(f) illustrate the three-dimensional cross-sections. The projectile direction is upwards, indicated by \vec{p}_0 . The general direction of the scattered projectile is labeled \vec{p}_{e1} while the momentum transfer is labeled \vec{q} . Here, the isotropic nature of the additional inelastic scattering process (d) is clearly visible while for the pure ionization (e), the minimum that separates the binary from the recoil lobe is starting to be filled-up compared to the monomer.

To investigate the differences of pure ionization between the monomer and the dimer a sufficient amount of data was acquired to present 3DCSs. In Fig. 5.5(a)-(c) and (e)-(f) the scattering plane, perpendicular plane and full-perpendicular plane are shown, respectively, for a scattering angle of $\theta_{e1} = -15 \pm 4^\circ$ and an ejection

⁴The constant factor that accounts for the difference in the number of constituents is neglected w.l.o.g.

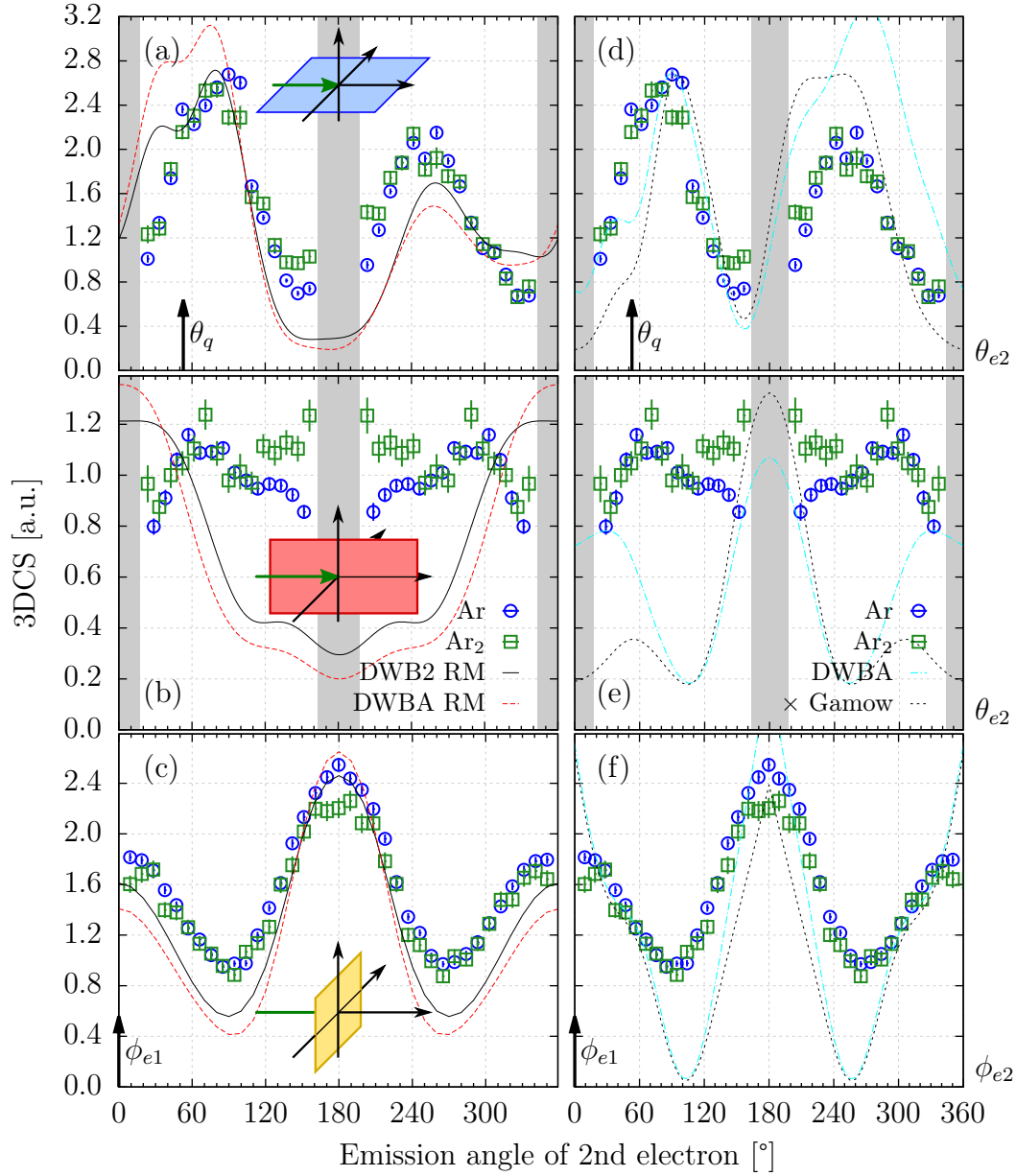


Figure 5.5.: 3DCS for $\theta_{e1} = -15 \pm 4^\circ$ and $E_{e2} = 10 \pm 2$ eV argon monomers (\circ , blue) and argon dimers (\square , green). Panels (a)-(c) show scattering plane, perpendicular plane and full-perpendicular plane, respectively, as do (d)-(f). The dashed red and solid black lines represent 1st and 2nd order DWBA RM calculation for atomic argon [Bartschat (2009)], the magenta dash-dotted line and the black dotted line show plain DWBA and DWBA with Gamow factor calculations, respectively.

energy of $E_{e2} = 10 \pm 2$ eV. Additionally, the detection planes are depicted by the small insets, where the green arrow represents the incoming projectile. The color coding is kept identical to Fig. 4.18(b). This energy was chosen in accordance with elastic electron scattering experiments on atomic argon [Mielewska et al. (2004); Stepanek (2003)]. For 10 eV electrons the integrated elastic scattering cross-section has a maximum of $\sigma_E \simeq 2 \times 10^{-15}$ cm². Additionally, the double-differential cross-section for this energy possesses isolated maxima for small angles ($< 20^\circ$) and large angles ($> 160^\circ$). For the dimer, this projects to a rescattering probability of 11%, while with a simple geometrical consideration one can derive a probability for either electron to scatter off the second atom of only 6.7%. A hybrid distorted-wave R-matrix calculation in first and second order of perturbation theory for atomic argon is plotted in Fig. 5.5(a)-(c) (cf. section 2.2.2). The normalization procedure is identical to the one applied in Fig. 5.4, except that while maintaining the relative normalization between the datasets, they are scaled such that the magnitude of the binary maximum for the monomer data coincides with that for the second-order calculation. While both calculations can reproduce the dominant features in the scattering plane (a), there are distinct deviations to the experimental data. Firstly, both the position of the binary and the recoil peak seem to be shifted in the calculation to the forward direction (i.e., 0° , 360°). Secondly, and this is a much more prominent effect, the intensity in the direction of the scattered projectile exceeds the data by as much as 40%. Combined, this points towards an underestimated treatment of PCI, which tends to shift the binary and recoil peaks to the backwards direction as well as suppressing the intensity in the direction of the projectile. The full-perpendicular plane (c), which is also governed by 1st-order interactions reproduces the shape qualitatively. Here, the intensity in the 180° -direction matches well as was expected from the scattering plane: both planes have common points for $(180^\circ, 90^\circ)$ and $(0^\circ, 270^\circ)$, respectively. The perpendicular plane (b), on the other hand, does not experience any agreement. While towards the backwards direction the shape appears similar, overall the predictions is quite off. Disagreement in this particular geometry, while achieving sound agreement in others (esp. coplanar), is a long standing problem not only for $(e, 2e)$ but also for ion impact experiments [Dürr et al. (2007); Schulz et al. (2003)]. Expectedly, the agreement between theory and experiment is worse for the 1st-order calculation, given that the projectile energy is far from high. By evaluating the theoretical prediction, it should, however, be noted

that at the current energy this model is known to deliver only mediocre results (cf. section 2.2.2).

The second set of calculations is plotted in Fig. 5.5(d)-(f) and compared to the same experimental data. While the model is still based on distorted-waves, the approach to account for PCI is performed in terms of the Gamow factor. Therefore, the (plain) DWBA 3DCS is multiplied by this factor. Since this procedure destroys the absolute scale of the calculation, it was kept identical to panels (a)-(c). The (plain) DWBA and the DWBA with Gamow factor were then scaled to the binary maximum of the experimental data (i.e., panel (d)). As for the procedure discussed above, scaling factors are always applied to all planes simultaneously, thus maintaining relative scale.

It seems remarkable that the, in principle, inferior plain DWBA, as compared to the R-matrix hybrid, seems to do a much better job predicting the binary maximum. However, at the same time the recoil peak is greatly over estimated in height and concerning its width, which increases the intensity in the direction of the projectile substantially. With the Gamow factor, small angles are underestimated whereas in the direction of the projectile satisfactory agreement is reached. The full-perpendicular plane (panel (f)) experiences worse agreement as compared to the DWBA RM calculation. Noteworthy is, however, how the edges of the recoil peak are predicted (i.e., 20° to 60° and 300° to 340°). At the same time, the predicted spikes of both calculations in the direction of the projectile seem counterintuitive. Lastly, the perpendicular plane (e) – though the shape is completely different from the DWBA RM – again experiences no agreement.

For the dimer data it is apparent, that the differences in the scattering plane are subtle and mostly in the backwards direction (i.e. 180°). The perpendicular plane, however, shows a significant enhancement for the dimers, indicating a redistribution of ejection directions due to additional elastic scattering processes. Although subtle, the differences observed are remarkable in respect to the fact that, compared to small clusters, only one single additional atom is located in the vicinity with a distance of 3.8 \AA . The possibility to study this geometry opens a particular sensitive case to higher-order contributions and/or multi-scattering events.⁵ For a very simplistic way of explaining differences between atom and dimer ionization, one

⁵Technically speaking, the rescattering of the ejected electron is still a first-order process.

possibility is to consider the interference of the electron scattering from either one of the two scattering center in analogy to Young’s double-slit experiment (cf. section 2.3.2). From looking at the calculated interference factor for randomly aligned argon dimers in Fig. 2.9(a), one can see immediately that the observed differences of the experimental data in Fig. 5.5 cannot be explained by this simple model. The Interference factor predicts very little deviation from 1 for the largest part of the angular range with the largest difference in the direction of the momentum transfer \vec{q} . The data, on the other hand, shows differences mostly in the backwards direction. The full-perpendicular plane in Fig. 5.5(c), however, shows that the dimer cross-section is slightly suppressed in the $\phi_{e2} = 0^\circ$ and the 180° -direction. Looking again at the interference factor in Fig. 2.9(a), this plane corresponds to a cut along the $\theta_{e2} = 90^\circ$ -direction. It is here where the interference factor actually predicts a reduction in the direction of \vec{q} (i.e., 180° in Fig. 5.5(c)) and the direction of the scattered projectile (i.e., 0° in Fig. 5.5(c)). On top of that, it seems that the relative trend does match as well. In the 180° -direction the dimer cross-section is suppressed stronger than in the opposite direction.

5.1.2. Neon

Similar to section 5.1.1, a single ionization experiment on neon atoms and dimers were performed at a lower projectile energy of $E_0 = 61$ eV. This energy holds a particular interesting feature. Compared to argon, the first ionization potential of neon for the removal of a $2p$ valence electron is, with 21.56 eV, larger [Ralchenko et al. (2011)]. Lowering of the projectile energy increases the possibility for symmetric energy sharing in the final state. Here, this situation is reached for an ejection energy of ~ 20 eV. For symmetric energy sharing it is in principle impossible to distinguish the final state electrons. Kinematically, on the other hand, the energy is still high enough that the projectile is most likely to be scattered to small scattering angles and, hence, enables the possibility of distinction.

To create dimers (or small clusters) from gaseous neon it was not sufficient to expand the gaseous neon through a nozzle at room temperature. Doing so creates hardly enough dimers to be distinguishable from background. Therefore, the nozzle was cooled to a temperature of $T_0 \approx 77$ K, by filling the attached dewar with liquid nitrogen (see Fig. 3.9). Compared to argon, the neon dimer has a smaller inter-

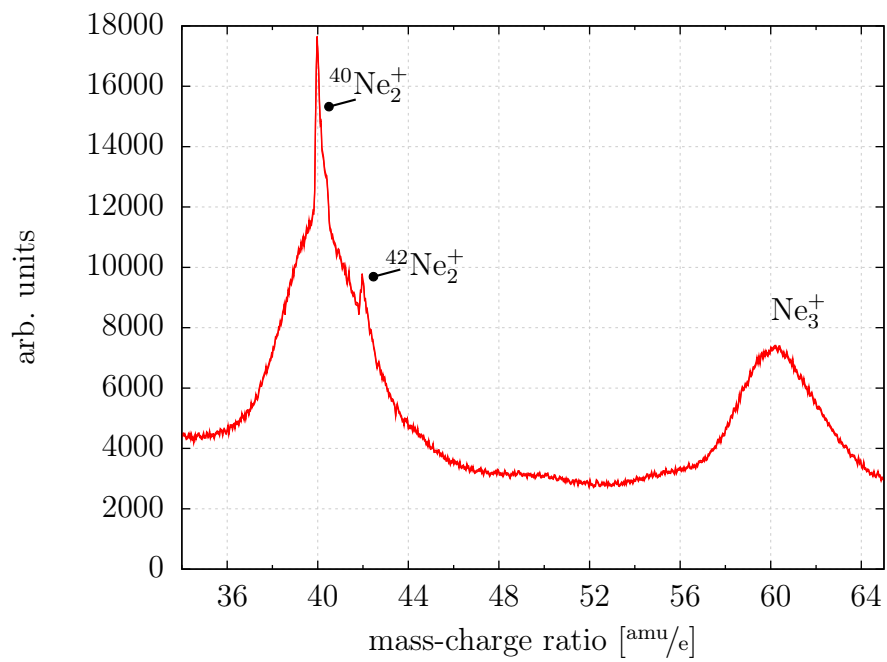


Figure 5.6.: Mass-by-charge representation of the TOF signal for neon at $E_0 = 61$ eV. Labels indicate the pure single ionization of Ne_2 with a mass of 40 amu, the isotope with mass $(20 + 22)$ amu and the trimers.

5. Results

nuclear distance of 3.1 Å. The corresponding TOF signal can be seen in Fig. 5.6. The time-axis is calibrated to the charge-by-mass ratio of the ions. Clearly visible is the singly-charged neon dimer from pure ionization on top of a broader peak of dimer ions that originate from the dissociation of small neon clusters. Additionally, at 42 amu/e, an isotope of the dimer ion could be observed, where one constituent is ^{20}Ne and the other is the isotope ^{22}Ne , which has a natural abundance of 9.25%. Around 60 amu/e stable trimer ions are detected. Judging from the shape of the distribution, particularly the absence of a narrow peak structure from a pure ionization, all detected trimer ions result from dissociation of small clusters with a size > 3 . Coincidentally, the mean cluster size can be assumed to be not significantly larger than 5. This is in accordance with fragmentation studies by e.g. Buck and theoretical models by Haberland and Halberstadt that stable trimer ions are created only by ionization of larger sized parent clusters (cf. section 2.3). Simulated fragmentations studies show an appearance of stable trimer ions for a parent cluster size of > 5 with an intensity of a few percent [Bonhommeau et al. (2006)].

A detailed picture of the ionization process can be obtained from Fig. 5.7 and Fig. 5.8, where 3DCSs for single ionization of atomic neon and neon dimers are presented. Figure 5.7(a)-(c) is plotted for a scattering angle of $\theta_{e1} = -20 \pm 3^\circ$ and an ejection energy of $E_{e2} = 10 \pm 2$ eV. The scattering geometries are depicted by the small insets (cf. Fig. 4.18(b)), namely the 3DCS for the scattering plane is shown in the top row, for the perpendicular plane in the middle row and for the full-perpendicular plane in the bottom row. After cross-normalization between the data sets for atoms and dimers to the 3D integral of the respective kinematical condition, they are finally scaled so the maximum of the binary peak for the atomic cross-section matches binary peak of the absolute scale of the plain DWBA.⁶ The same is done for the DWBA with Gamow calculation. The kinematic is chosen such that the momentum of the ejected electron is $p_{e2} = 0.85$ a.u. and the momentum transfer is $q = 0.89$ a.u., hence, they are very close. For a $2p$ electron to be ejected in the direction of the momentum transfer, in its initial bound state it needs to have ~ 0 a.u. of momentum. However, the momentum distribution of a p electron experiences a node at 0 a.u. (cf. section 2.1). Furthermore, the momentum distribution of the $2p$ state in neon has a maximum at ~ 0.9 a.u. [Daoud et al. (1985)]. Consequently, the

⁶The normalization procedure is explained in more detail in section 5.1.1, pp. 100.

probability for the bound electron to be ejected in the direction of q will be greatly suppressed. Looking at the plain DWBA calculation in panel (a) (black curve), it shows a characteristic dip for θ_q , while the binary peak consists of the complete double peak structure, i.e., from 0° to 90° .

The actual shape of the cross-section in panel (a) is, on the other hand, strongly governed by the fact that the final state electrons have almost comparable energies. While the ejected electron is fixed at $E_{e2} = 10 \pm 2$ eV, the scattered projectile electron has an energy of only $E_{e1} = 29.4$ eV and, therefore, the final state repulsion is strong. Consequently, the cross-section in the principle direction of $e1$ – i.e. $\theta_{e1} \sim 340^\circ$ – is strongly suppressed and the binary and recoil peaks are shifted to the direction of 180° . The inclusion of PCI by means of the Gamow factor (red-dashed curve) reduces the magnitude of the cross-section almost completely in the 0° -direction and leaves only a small remainder of the double peak which reproduces the shape of the experimental data rather well in the scattering plane. The data shows, however, an additional dip in the recoil peak that is not predicted. In the perpendicular plane, the calculation has severe problems describing the backwards direction. Overall the discrepancy improves in the full-perpendicular plane, nevertheless, the shape for the 180° -direction cannot be reproduced. Looking at the comparison between atoms and dimers, the scattering plane experiences large similarities between the two. In fact, hardly any discrepancies in the cross-sections are observed that go beyond the statistical error of the data sets. The perpendicular plane in panel (b), on the other hand, shows small deviations particularly in the 90° and 270° -directions. While the atomic cross-section is increasing monotonously towards the $\theta_{e2} = 180^\circ$ backwards direction which matches with the Gamow calculation, the dimer cross-section, in the vicinity of these distinct directions, shows is slightly increased while the shape is decreasing. This point will become important later in this chapter when the 3D emission patterns are discussed. Lastly, panel (c) shows the full-perpendicular plane. While the enhancement in the dimer cross-section from panel (b) is not unambiguously identifiable, the backwards direction shows a dip for the dimer data where the atomic data experiences a broad peak. Additionally, the forward direction shows a slight modulation for the dimer: In the $(60^\circ, 300^\circ)$ -direction it is slightly below and starts to increase above the atomic cross-section towards 0° .

Figure 5.8 represents the 3DCS for identical scattering geometries and ejection

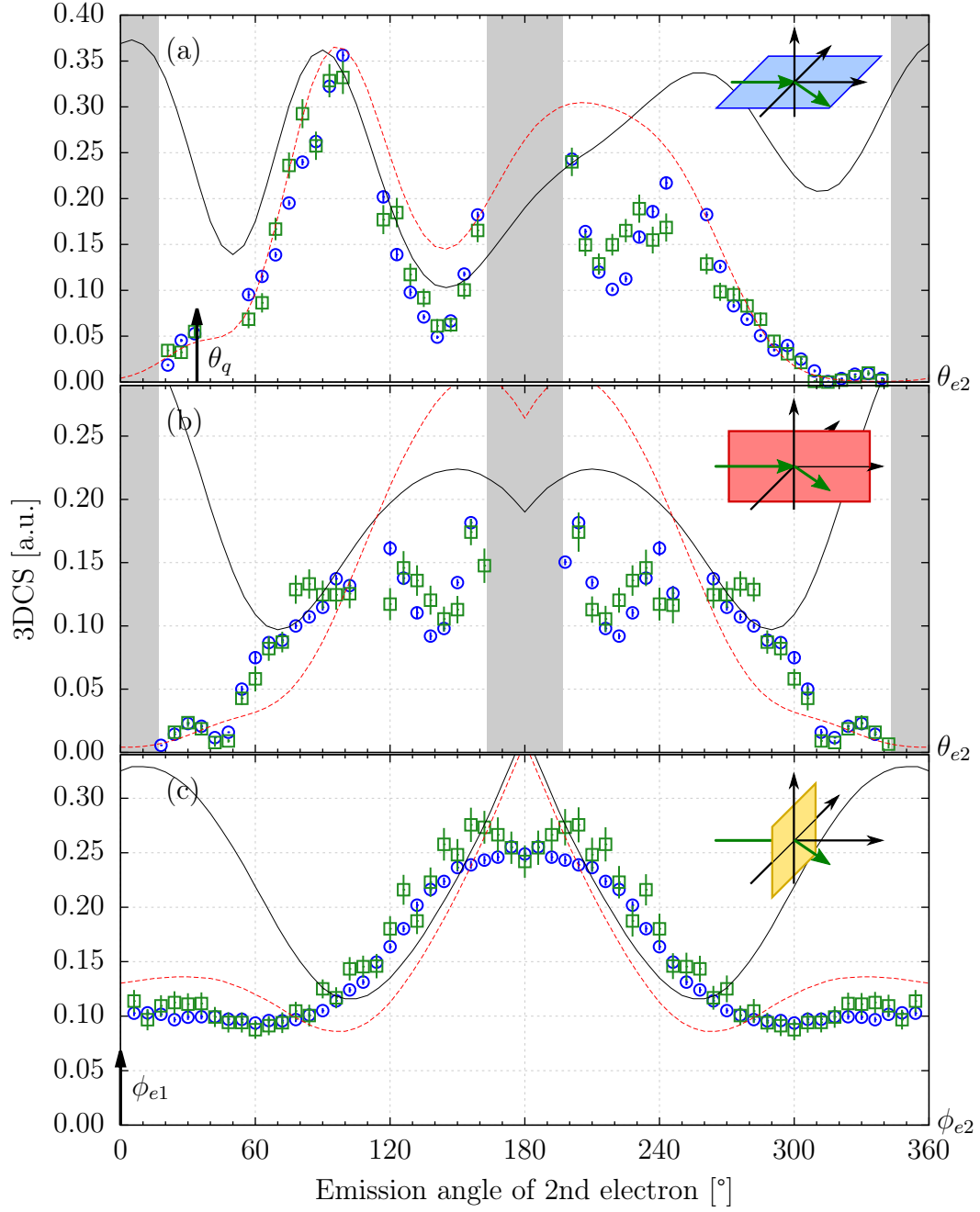


Figure 5.7.: 3DCS for neon monomers (\circ , blue) and neon dimers (\square , green) at 61 eV projectile energy. Panels (a)-(c) show scattering plane, perpendicular plane and full-perpendicular plane, respectively, for $\theta_{e1} = -20 \pm 3^\circ$ and $E_{e2} = 10 \pm 2$ eV. The solid black and red-dashed lines represent DWBA calculation DWBA with Gamow factor calculations, respectively [Amami and Madison (2011)].

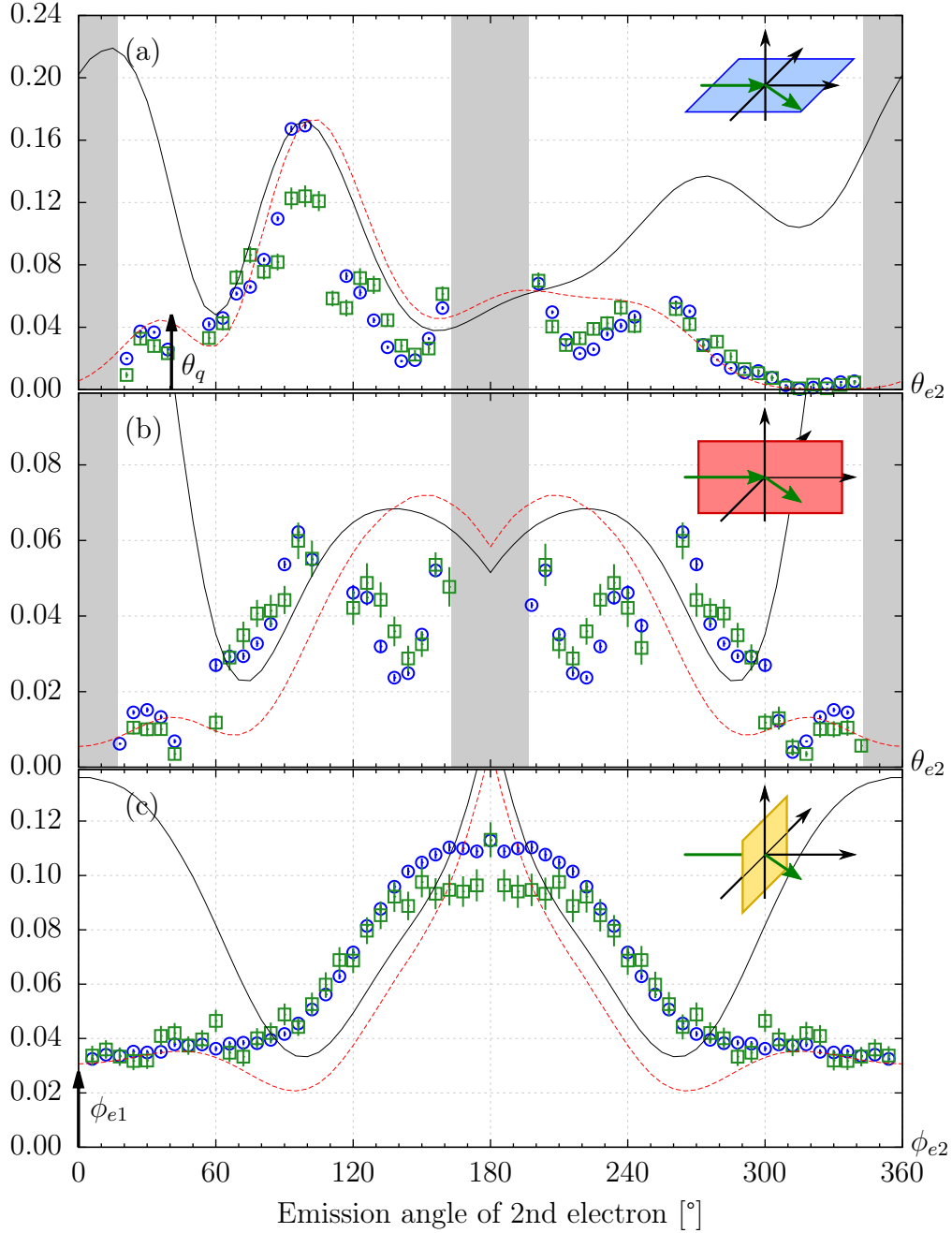


Figure 5.8.: 3DCS for neon monomers (\circ , blue) and neon dimers (\square , green) at 61 eV projectile energy. Panels (a)-(c) show scattering plane, perpendicular plane and full-perpendicular plane, respectively, for $\theta_{e1} = -30 \pm 3^\circ$ and $E_{e2} = 10 \pm 2$ eV. The solid black and red-dashed lines represent DWBA calculation DWBA with Gamow factor calculations, respectively [Amami and Madison (2011)].

energy of $E_{e2} = 10 \pm 2$ eV but for a larger scattering angle for the fast electron of $\theta_{e1} = -30 \pm 3^\circ$ as compared to Fig. 5.7. The momentum transfer for this condition is with $q = 1.12$ a.u. larger than the momentum of the ejected electron. A characteristic effect of an increased momentum transfer can be seen in terms of a reduced recoil peak intensity. Again, the DWBA with Gamow model does a good job describing the data in the scattering plane in panel (a). The perpendicular plane (b) shows a less pronounced, but still visible, enhancement for the dimer cross-section in the 90° -direction and 270° -direction, while the full-perpendicular plane (c) shows a quite different behavior for the dimer than for the smaller scattering angle. Here, the 180° -direction is suppressed by roughly 15% while the oscillations towards the direction of the $\phi_{e1} = 0^\circ$ have increased. The peak in the forward direction of the scattering plane has increased relative to the binary peak for an increased scattering angle θ_{e1} leading to a slightly weaker suppression due to PCI.

The ejection of the slow electron to the plane perpendicular to the incoming projectile for different scattering angles of the fast electron is shown in Fig. 5.10. The ejection energy is kept constant for all plots with a value of $E_{e2} = 20 \pm 3$ eV, which results in symmetric energy sharing between the final state electrons. In panels (a)-(d) the atomic distribution is compared to the dimer distribution in a Cartesian representation. Focusing on the atomic cross-sections, the general behavior is governed by the first-order dynamics, where the ejected electron scatters to the opposite direction with respect to the projectile electron with high probability (i.e., binary maximum peaking at $\phi_{e2} = 180^\circ$) and with a lower probability into the same half-plane of the projectile (i.e., the recoil maximum at 0°). With increasing scattering angle this behavior starts to change gradually. For $\theta_{e1} = -40 \pm 4^\circ$ it is apparent that the distribution in the 180° -direction starts to become broader while, at the same time, additional structures in the 60° - and 300° -direction start to emerge (marked gray in Fig. 5.10(c) and (d)). This indicates the onset of more complicated scattering dynamics when both electrons are forced in the full-perpendicular plane [Al-Hagan et al. (2009); Nixon et al. (2010)]. To have the two final state electron emerge under 90° with respect to the projectile direction has been described in the framework of the DWBA: By excluding interaction with the nucleus, the only possibility in a binary collision is for the active electron to cancel the momentum in the direction of the projectile. As a result, both electrons – when forced to the full-perpendicular plane – have to leave the target back-to-back, similar to the behavior close to ion-

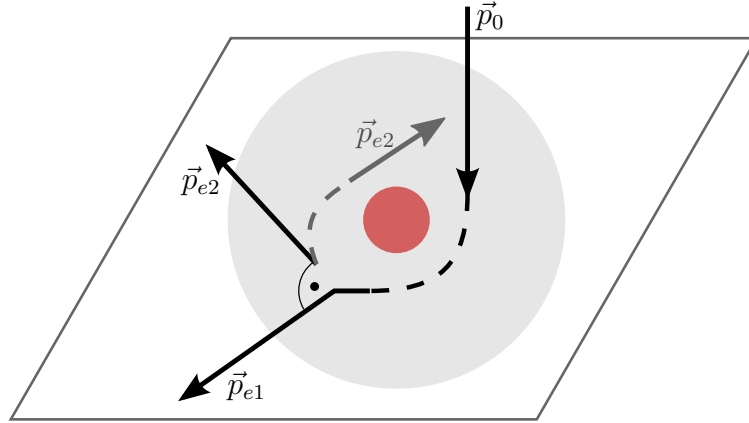


Figure 5.9.: Schematic mechanism for electrons being emitted to the full-perpendicular plane. The projectile \vec{p}_0 scatters elastically at the core potential (red) to the full-perpendicular plane (gray). After a subsequent binary collision the two final state electrons \vec{p}_{e1} and \vec{p}_{e2} are either emitted under mutual angles $90^\circ/270^\circ$ or one of the outgoing electrons scatters at the core which results in a 180° mutual angle.

ization threshold. This, however, turns out to be a very unlikely process due to the fact that the bound electron has to match the projectile momentum not only in magnitude but also in direction.

Later, Al-Hagan et al. conceived a – in actuality more complex – mechanism that was found to be able to describe the additional structure. This process, depicted in Fig. 5.9, demands an initial elastic scattering of the projectile to full-perpendicular plane, followed by an inelastic binary collision. The projectile, coming from above, with a momentum \vec{p}_0 and the final state electrons \vec{p}_{e1} and \vec{p}_{e2} are shown in the gray full-perpendicular plane. The outgoing electrons most likely constitute a mutual angle of 90° – as can be seen in coplanar cross-sections – which, due to the symmetry within the detection plane, is also mirrored to 270° . Following the binary collision one of the final state electrons might also elastically scatter from the nucleus. In this case the electrons appear with a mutual angle of 180° , thus forming a back-to-back emission feature.

As pointed out above, the 90° -features in Fig. 5.10(d) appear at smaller azimuthal angles (i.e., $\sim 60^\circ/300^\circ$) as explained. This effect is largely due to the fact that the projectile in Fig. 5.10 is not bound to the full-perpendicular plane, but is fixed at a scattering angle $< 90^\circ$. This shift can be predicted by contemporary theory and

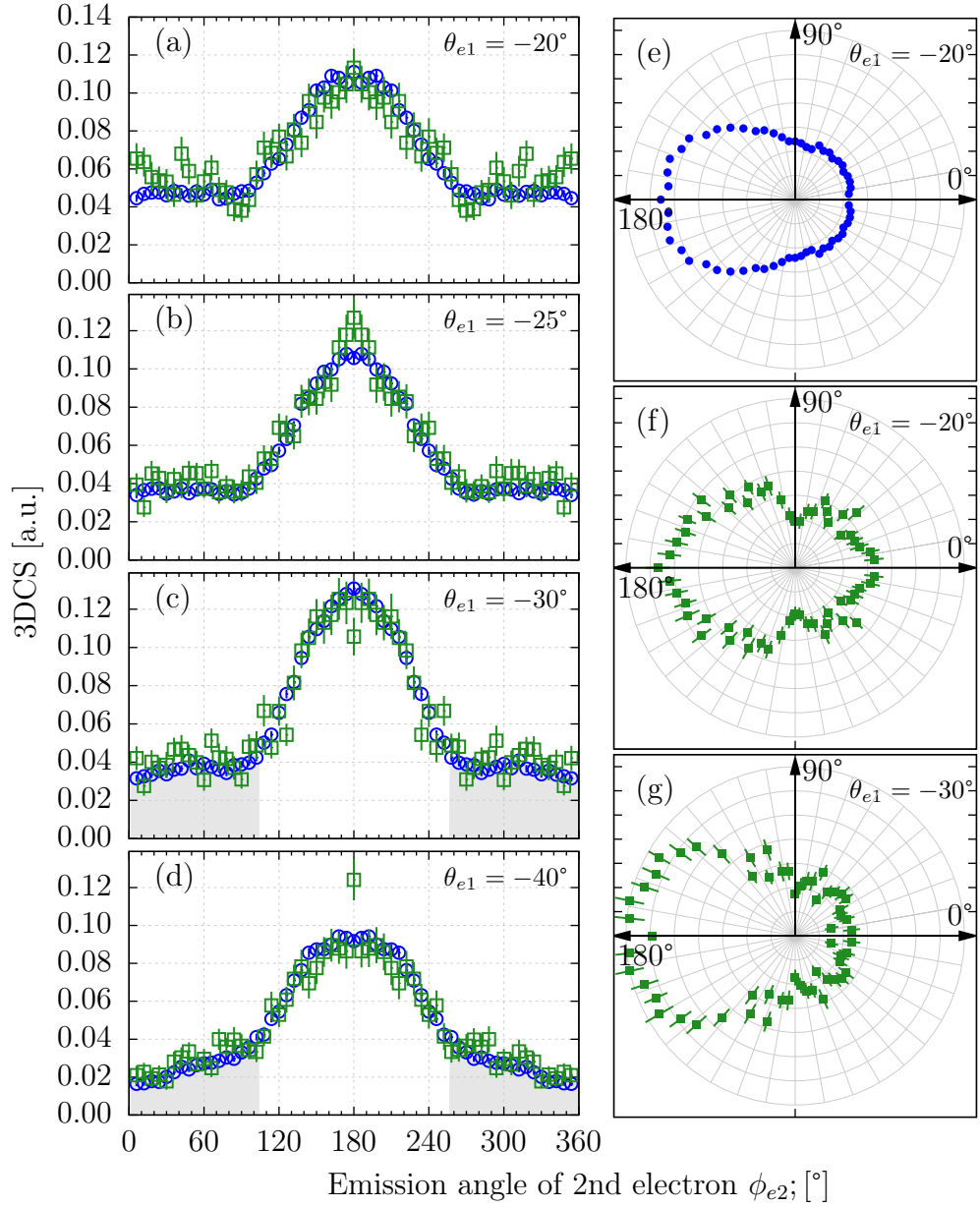


Figure 5.10.: 3DCS in the full-perpendicular plane. Neon atoms (\circ , blue) and neon dimers (\square , green) at 61 eV projectile energy. Panels (a)-(d): scattering angles $\theta_{e1} = -20 \pm 4^\circ$, $-25 \pm 4^\circ$, $-30 \pm 4^\circ$ and $-40 \pm 4^\circ$, respectively for an ejection energy of $E_{e2} = 20 \pm 3$ eV ($E_{e1} = 20$ eV). Panel (e): polar representation of panel (a) for atomic data. Panels (f) and (g): polar representation of panels (a) and (c), respectively, for dimer data.

has been shown e.g. for single ionization of helium [Ren et al. (2011)].

Looking at the cross-section for single ionization of the neon dimer in the full-perpendicular plane, it follows that for the atom, suggesting similar ionization dynamics for the final state electrons. Previous experiments for ionization of helium and H_2 exploiting this particular geometry observe a distinctive difference in the cross-sections (e.g., [Ren et al. (2010)]). The theoretical model used to describe these processes – the M3DW – assumes a random orientation of the H_2 molecule by assuming a spherical distribution of the nuclear charge. The *core* potential for helium, on the other hand, is strongly localized and therefore deeper than for the averaged hydrogen molecule. Consequently, the cross-sections for helium differ in the much higher probability for one of the two outgoing electrons to rescatter elastically, resulting in a back-to-back emission and a pronounced 180° peak. For the comparison of H_2 and He, this picture is apt since both have an equal core charge. For this work, a similar picture for the comparison between Ne and Ne_2 is not straight forward. First of all, the dimer has double the core charge than the atom and on top of that for neon it is five times, for argon nine times larger than for helium. And while hydrogen has a relatively small internuclear separation of $R_{\text{int.}}(\text{H}_2) = 1.4 \text{ a.u.}$, the neon dimer has a mean separation of $R_{\text{int.}}(\text{Ne}_2) = 5.9 \text{ a.u.}$ and $R_{\text{int.}}(\text{Ar}_2) = 7.1 \text{ a.u.}$ for the argon dimer [Patkowski et al. (2005); Tao and Pan (1992); Ulrich et al. (2011)]. This creates much more localized *atomic* core potentials for the randomly aligned dimers than in the case of hydrogen and therefore the assumption of a spherical nuclear charge distribution is certainly not as good.

However, a closer look at the distributions in Fig. 5.10 reveals interesting features. In panels (e) and (f) corresponding polar representations of the data for the smallest scattering angle $\theta_{e1} = -20 \pm 4^\circ$ from panel (a) are shown. Particularly, panel (e) shows the atomic data while in panel (f) the dimer data is depicted. Compared to the atoms, the dimer cross-section experiences a pronounced dip in the 90° -direction and peak structures in the $-x$ direction where the atomic cross-section is simply flat. A similar behavior can be observed in panel (g) – the polar representation for the dimer data from panel (c). The dimer cross-section appears to fluctuate around the atomic cross-section.

For further investigation it can be made use of the fact that the spectrometer enables access to all possible planes and therefore, 3D FDCSs can be presented. In Fig. 5.11 three different kinematics are chosen. The top row represents $\theta_{e1} = 25^\circ \pm 3^\circ$

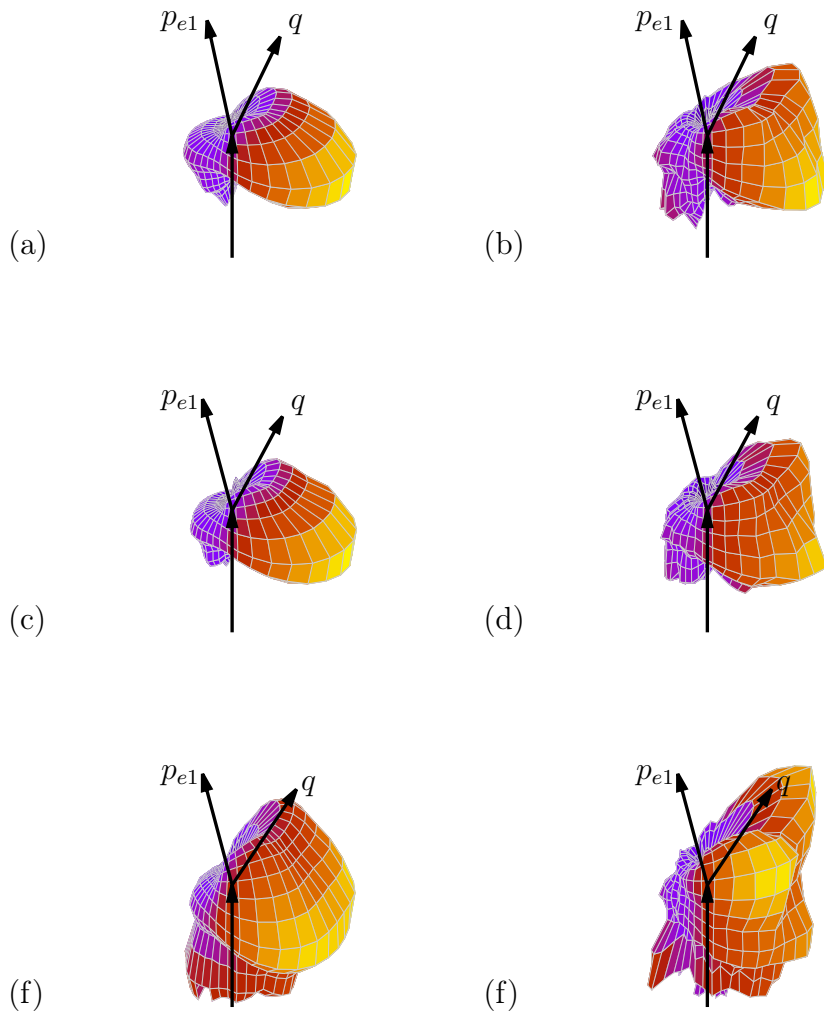


Figure 5.11.: 3D FDCS for electron impact single ionization of neon atoms and dimers. Left column (panels (a),(c),(e)) for atomic argon, right column (panels (b),(d),(f)) for dimers. Top row: $\theta_{e1} = 25^\circ \pm 3^\circ$, $E_{e2} = 10 \text{ eV} \pm 2 \text{ eV}$, middle row: $\theta_{e1} = 30^\circ \pm 4^\circ$, $E_{e2} = 10 \text{ eV} \pm 2 \text{ eV}$, bottom row: $\theta_{e1} = 30^\circ \pm 4^\circ$, $E_{e2} = 5.0 \text{ eV} \pm 1.5 \text{ eV}$.

and $E_{e2} = 10 \text{ eV} \pm 2 \text{ eV}$, the middle row $\theta_{e1} = 30^\circ \pm 4^\circ$, $E_{e2} = 10 \text{ eV} \pm 2 \text{ eV}$ and the bottom row $\theta_{e1} = 30^\circ \pm 4^\circ$, $E_{e2} = 5.0 \text{ eV} \pm 1.5 \text{ eV}$. The atomic cross-sections are plotted in the left column while the dimer cross-sections are on the right. Again, the arrows marked p_{e1} and q indicate the directions of the scattered projectile and the momentum transfer, respectively, both of which are in the scattering plane. The arrow coming from below indicates the incoming projectile.

Already from a quick overview it is obvious that the dimer cross-sections differs from the atomic cross-sections in a key aspect. All dimer cross-sections show two lobes on both sides of the scattering plane roughly in the direction of the momentum transfer. Their magnitude depends on the kinematics. In particular, it depends on how much the ejected electron is affected by PCI and, consequently, how strong the emission in the direction of these lobes is suppressed. For example, in panels (b) and (d), which both represent the same ejection energy of $E_{e2} = 10 \text{ eV}$ ($E_{e1} = 30 \text{ eV}$), the emission in the atomic case (panels (a) and (c)) is very low. As a result, this feature is small. For the more asymmetric case in the bottom row, where the ejection energy is only 5 eV ($E_{e1} = 35 \text{ eV}$) and the atomic intensity in the direction of q is increased, it turns out that the lobes of the dimer cross-section is also strongly increased. Interestingly, the appearance does not seem to affect the distribution in the scattering plane or in any of the geometries that have been chosen to present quantitative comparisons between the data and calculations. The only indications of this feature are visible in the perpendicular plane in Fig. 5.7(b) and (e), where an increase in the dimer cross-section, roughly in the $(90^\circ, 270^\circ)$ -direction, was observed.

Due to the lack of theoretical calculations for electron impact ionization of the neon dimer, it is hard to pinpoint the origin of the lobes. The obvious idea of a simple interference model could already be discarded, since it affects mostly the direction of the momentum transfer (see section 2.3.2). Another idea is to think of the different symmetry properties of atomic and molecular wave functions. Due to the additional degrees of freedom, a multitude of symmetries have to be considered if these systems are excited, which modifies the emission patterns dramatically. In a coarse approximation, the theoretical angular distributions for photoionization of atomic neon and neon dimers can be compared to the electron impact cross-sections. Electron impact can generally be linked to photoionization at high energies and small momentum transfer. Then \vec{q} corresponds to the polarization vector $\vec{\epsilon}$ of the laser field and the interaction is of first-order leading to dipole transitions (cf. section 2.1). If

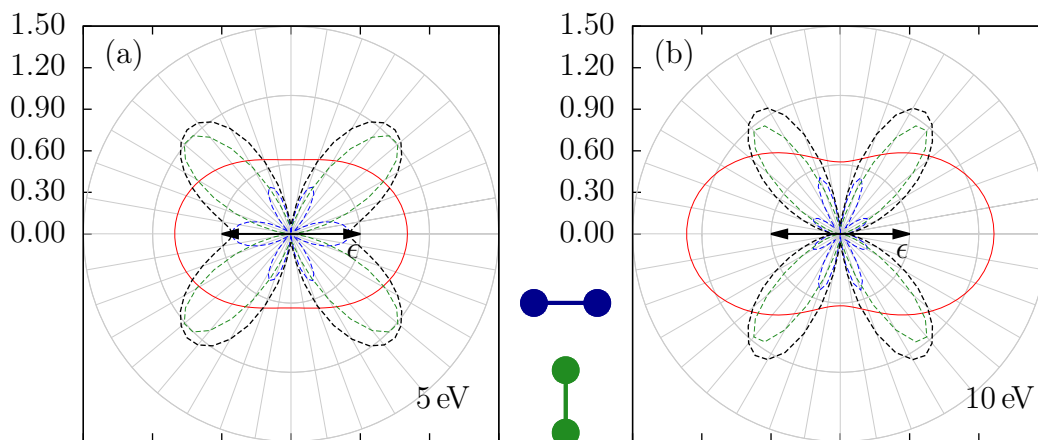


Figure 5.12.: Angular distribution from photoionization of atomic neon (red) for 5 eV electrons (a) and 10 eV electrons (b). The dashed lines indicate the distribution for ionization of Ne_2 . Blue-dashed: dimer axis parallel, green-dashed: dimer axis perpendicular. The black-dashed curve marks the sum of the former. The vector ϵ denotes the polarization direction [Cherepkov (2012)].

the magnitude of the momentum transfer $|\vec{q}|$ increases while the energy is still high, also multipole elements contribute to the transition. Lowering the impact energy leads to an increasing contribution of higher-order collision, increasing final state correlation (e.g., PCI). As a consequence, the symmetry of emission with respect to \vec{q} is broken.

In a first attempt, the angular distributions for electrons of 5 eV and 10 eV after photoionization with linear polarization are compared. The ionization of a $2p$ electron in atomic neon can be easily be calculated [Taylor (1977); Yeh and Lindau (1985)]. First, the distributions for ionization of atomic neon are presented in Fig. 5.12 in red. Here, in panel (a) the distribution for 5 eV is depicted, while in panel (b) the one for 10 eV is shown. Both distributions show an elongation along the polarization direction. Unlike a pure p -wave emission, the intensity does not reduce to zero for 90° emission, which is due to a superposition of s and d partial waves. Additionally, calculated distributions for photoionization of neon dimers for identical electron energies are presented [Cherepkov (2012)]. Here, the dumbbells indicate the orientation of the internuclear axis with respect to the polarization direction. Specifically, the blue-dashed curves represent the case where the dimer is

oriented in parallel to the polarization, while for the green-dashed curves the axis is perpendicular to the polarization. Since, for this experiment, the dimers were not oriented but randomly distributed, the black-dashed curves depict the sum of the former two.

It is quite apparent that, in the case of photoionization, even though the binding between the neon atoms is very weak, the transition from an atom to a dimer makes a tremendous difference. While the atomic distributions exhibit a broad maximum in the polarization direction, the dimer case shows strong suppression in and perpendicular to the direction of ϵ . While the two distributions are equally pronounced in their lobes, the distribution for the smaller energy exhibits less suppression along the polarization. If one tries to associate these findings to electron impact, the quantization axis that corresponds to the polarization, according to Dunn, is the direction of the momentum transfer q [Dunn (1962)]. Furthermore, the distributions in Fig. 5.12 are presented for a single plane because of the axial symmetry with respect to ϵ . What also has to be considered, is that still the ejected electron is subject to PCI. That means the strong emission in the forward direction, resulting from aligning the distribution along q , would be suppressed. Again looking at the 3D emission patterns in Fig. 5.11, the differences in the cross-sections for the dimer, which occur with respect to the momentum transfer can be due to effects of molecular orbitals in the dimer. On the other hand, as it appears, this effect seems to be an addition to the atomic cross-section. The strong effect of suppression perpendicular to the polarization direction is interesting with respect to the cross-sections for the full-perpendicular plane presented in Fig. 5.10. There, the dimer shows a suppression in the 90° -direction which coincides with the direction perpendicular to the momentum transfer. From this point of view, it is likely to attribute this deviation to an effect of molecular orbitals in the dimer.

5.2. Dissociative Ionization of Small Argon Clusters

Further investigation of charged particle ionization of small rare gas clusters was performed in an experiment studying the dissociation of the target into two charged fragments with a projectile energy of 130 eV. By detecting the ionic fragments,

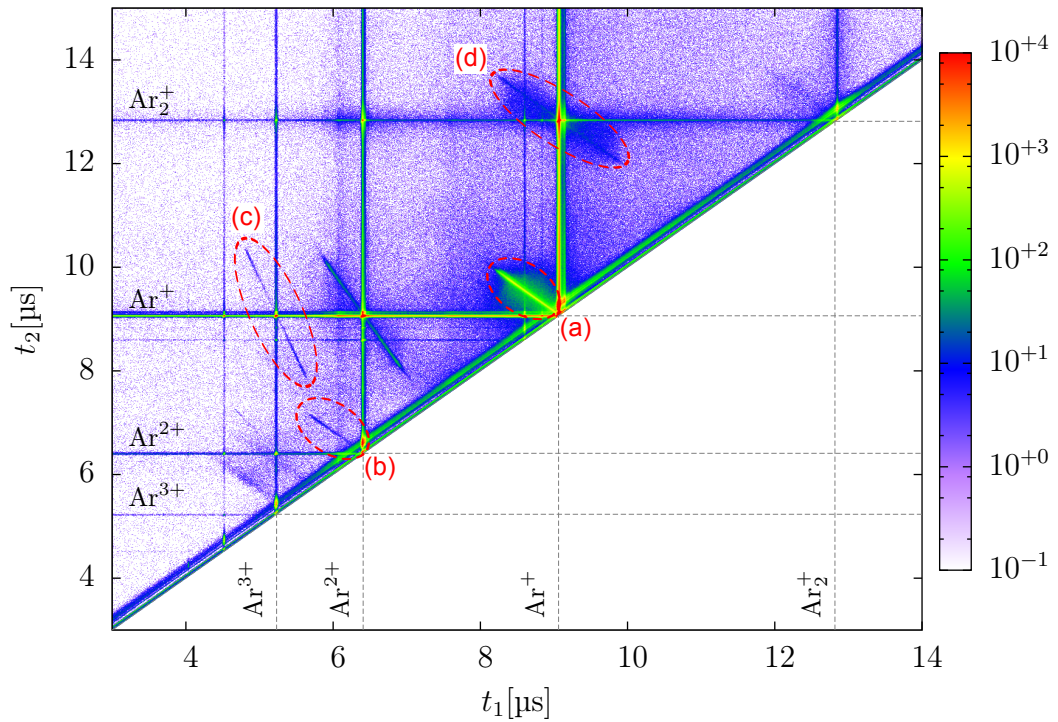


Figure 5.13.: Coincidence map for two ions t_1 and t_2 . The dashed lines indicate the pure ionization TOF for the corresponding species. The tilted lines represent the coincidence signature between two ions due to momentum conservation. In Particular, region (a) depicts Ar^+/Ar^+ coincidences, region (b) $\text{Ar}^{2+}/\text{Ar}^{2+}$, region (c) $\text{Ar}^{3+}/\text{Ar}^+$ and region (d) $\text{Ar}_2^+/\text{Ar}^+$.

e.g., from a Coulomb exploding dimer, additional information about the ionization process can be gathered. Foremost, in diatomic molecules Coulomb explosion takes place along the direction of the internuclear separation and the momenta of the fragments can then be used to obtain the information about the spacial alignment of the molecule at the time of the breakup. Furthermore, the energy of the fragments (i.e., the KER) gives insight into the distance at which the breakup occurred. In turn this information can be linked to the time scale of the process, whether it was prompt or the molecule had time to contract. Lastly, Coulomb explosion involves additional interesting processes such as multiple ionization, ICD (cf. section 2.3.1) and charge transfer.

The way to check for coincident ion events, is to exploit momentum conservation. The momenta of the two ions emerging from the Coulomb explosion of a dimer have to sum up to zero. In Fig. 5.13 coincidences are observed in terms of the TOF of two ion events t_1 and t_2 .⁷ For a Coulomb explosion, these two times will have to be correlated, meaning if one ion is emitted towards the ion detector – resulting in a short TOF – the other needs to be emitted in the opposite direction, which results in a larger TOF. The results is a coincidence lines with a negative slope in Fig. 5.13. The diagonal that separates the upper left from the lower right is the boundary for $t_1 = t_2$, where both of the ions have identical TOFs. Since the ions are sorted with increasing TOF and the one plotted on the x -axis is the one that arrives earliest, the lower right of the plot remains empty. The vertical and horizontal lines observed in the plot coincide with TOFs for the corresponding ionic species from pure ionization (indicated by the labels). For example, the line marked Ar^+ coincides with the TOF for pure single ionization of atomic argon. This part of the data distributed vertically and horizontally represent *false* coincidences. They occur if one ion from an actual dissociative event is detected together with one from a non-dissociative ionization event, meaning two independent interactions occurred within one shot of the electron gun. Then, of course, no correlation exists between the TOFs, i.e. one TOF as a function of the other is constant: $t_2(t_1) = \text{const}$.

Besides the most prominent channel, the Ar^+/Ar^+ (region (a)), a multitude of different fragmentation channels of the dimer can be observed. Next to fourfold symmetric and asymmetric charged final states such as $\text{Ar}^{2+}/\text{Ar}^{2+}$ (region (b)) and

⁷This corresponds to longitudinal momentum conservation since $t_{\text{TOF}} \propto p_z$ (4.2).

5. Results

$\text{Ar}^+/\text{Ar}^{3+}$ (channel (c)) even a channel for a trimer breakup (region (d)) could be detected. Here, the trimer dissociates into a dimer and a monomer ion: $e^- + \text{Ar}_3 \rightarrow \text{Ar}_2^+ + \text{Ar}^+ + 3e^-$. On the other hand effectively no $\text{Ar}_2^+/\text{Ar}_2^+$ coincidences are observed which, from this point, can be due to a negligible amount of neutral quatomers or an unfavored fragmentation path. Looking at the $\text{Ar}_2^+/\text{Ar}^+$ area in Fig. 5.13, apart from the narrow coincidence line a significant background can be seen (a closeup is presented in Fig. 5.18). This indicates an additional momentum in the breakup which does not satisfy the two-particle momentum conservation. Most likely, the momentum is carried away by a fourth (e.g. neutral) constituent. An already interesting result given that the dimer ion is considered to be the most abundant ionic species in small cluster fragmentation (see section 2.3). The trimer, on the other hand, can also dissociate into three argon ions 3Ar^+ . This cannot be discriminated in the two-particle coincidence and will appear as background underneath the Ar^+/Ar^+ coincidence in region (a). Since the statistics for trimer related coincidences are generally low and the area selected for the dimer breakup is narrow compared to the background, this contribution can safely be neglected.

For the coincident two-body Coulomb explosion, the sum kinetic energy release (or KER) of the fragments can be related to their internuclear separation. The KER of the fragments reflects the Coulombic energy at the particular internuclear distance the explosion occurs: $E_{\text{KER}} \propto 1/R_{\text{int.}}$. By selecting the corresponding events from Fig. 5.13, KER spectra for various channels can be created and the dedicated internuclear separation curves give insight into the breakup mechanism. Exemplarily, the KER spectra for the breakup of neutral dimers into doubly-charged ($\text{Ar}_2 \rightarrow \text{Ar}^+ + \text{Ar}^+$) and triply-charged ($\text{Ar}_2 \rightarrow \text{Ar}^{2+} + \text{Ar}^+$) final states are presented in Fig. 5.14 (panels (a) and (b), respectively). Additionally, the trimer breakup into a doubly-charged ($\text{Ar}_3 \rightarrow \text{Ar}_2^+ + \text{Ar}^+$) final state is plotted in panel (c). Here, the association of the KER to a particular internuclear separation, let alone its orientation or structure, is not straight forward due its geometry. Furthermore, the two charges in the final state localize at two fragments, suggesting a complex reorientation process to occur after ionization. In each panel also Gaussian curves, which were obtained by a fitting procedure, are shown.

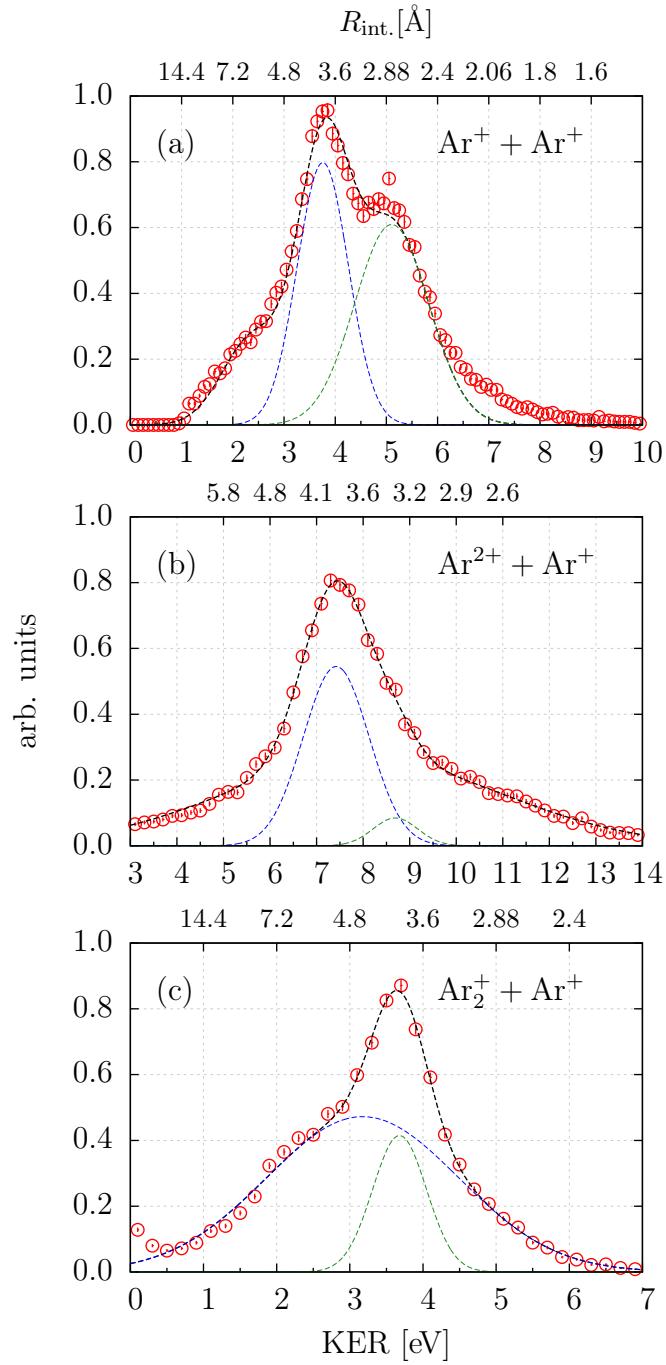


Figure 5.14.: Kinetic energy release spectra (KER) for different breakups of small argon clusters. Panel (a): $\text{Ar}_2 \rightarrow 2\text{Ar}^+$. Panel (b): $\text{Ar}_2 \rightarrow \text{Ar}^{2+} + \text{Ar}^+$. Panel (c): $\text{Ar}_3 \rightarrow \text{Ar}_2^+ + \text{Ar}^+$. Dashed curves represent Gaussian fits. Top scales indicate internuclear distances in Angstrom.

5.2.1. Doubly-charged Final State: $\text{Ar}^+ + \text{Ar}^+$

The dimer breakup into two singly-charged argon ions in panel (a) shows two main contributions. The one with the highest intensity at 3.76(9) eV (dashed-blue), which translates to an internuclear distance of $R_{\text{int.}} = 3.83(1) \text{ \AA}$, and the dashed-green with slightly lower intensity at 5.10(12) eV or $R_{\text{int.}} = 2.82(7) \text{ \AA}$. Comparing this to the neutral dimers internuclear separation of $R_{\text{int.}}(\text{Ar}_2) = 3.77 \text{ \AA}$ (see [Patkowski et al. (2005)]), it is apparent that the two contributions to the KER spectrum in panel (a), that is to say the mechanisms leading to these contributions, occur on different time scales. While the latter (dashed-green) occurs at a significantly smaller separation compared to the size of the neutral dimer, the former (dashed-blue) takes place at, within the statistical error, exactly the neutrals internuclear separation. This suggests already a number of different mechanisms leading to dissociation. In a molecular picture, the dissociation of a neutral dimer (or any molecule, for that matter) can take happen in essentially two ways. Either the final state is reached to directly, that is, the projectile electron excites the system to the dissociative potential curve or it is reached through predissociation. The latter involves coupling to an energetically higher lying excited state. If this state intersects with a dissociative curve charge can be transferred resonantly between the constituents and the system coulomb explodes. If no intersection occurs, still the system can dissociate by emitting the excess energy in terms of a photon. This process is usually called radiative charge transfer (RCT) (cf. section 2.3.1).

By taking into account that the interaction involving inelastic electron impact obeys the Franck-Condon principle, which basically reflects the fact that the interaction time takes place on a much shorter time scale than the molecular movement, a KER signature related to an internuclear distance smaller than that of the neutral has to undergo some rearrangement before the Coulomb explosion takes place. Since such a rearrangement does not occur instantly, we can infer, that the dashed-green contribution in Fig. 5.14(a) is subject to predissociation.

More information about the underlying processes can be obtained by looking at similar experiments. In a photoionization experiment by Ueda et al. investigating the $2p$ ionization of Ar_2 , where after an Auger decay that takes place in one of the constituents and a subsequent Coulomb explosion, essentially two channels are found: one leading to a triply-charged and one leading to a doubly-charged final

state [Saito et al. (2007); Ueda et al. (2007)]. For the latter the KER spectrum shows only a single peak at 5.2 eV ($\hat{=} 2.77 \text{ \AA}$), which coincides with the dashed-green contribution in panel (a), and no correlation between low energetic electrons could be found to identify the process as ICD (cf. section 2.3.1). They conclude that the only pathway is through radiative charge transfer (RCT) from the intermediate $\text{Ar}^{2+}(3p^{-2}) + \text{Ar}$ states. As mentioned above, RCT is a predissociation mechanism where the excess energy is emitted via a photon [Johnsen and Biondi (1978)]. For the given projectile energy of 120 eV the $2p$ electron with an ionization potential of roughly ~ 250 eV is energetically not accessible. On the other hand, for direct creation of the doubly ionized state the total cross-section is $2.79 \times 10^{-17} \text{ cm}^2$ while the contribution of the $(3p^{-2})$ channel – whose IP can be assumed to be 43.39 eV – is $2.48 \times 10^{-17} \text{ cm}^2$, which corresponds to 89 % [Jha et al. (2006)].⁸ This means for electron impact the state can be accessed directly. The neutral dimer undergoes a transition to a one-site doubly-charged state of the dimer ion ($\text{Ar}_2 \rightarrow \text{Ar}^{2+} + \text{Ar}$), subsequently contracts up to a point where the overlap between the valence electron and the inner-shell hole is sufficiently large. Finally, one electron can transfer while the excess energy is released by photon emission (see Fig. 2.8).

Similar features in the KER spectrum for the doubly-charged final state in Ar_2 have also been observed in strong field ionization experiments by Ulrich et al. and Manschwetus et al. [Manschwetus et al. (2010); Ulrich et al. (2010)]. These experiments were carried out with focal intensities of $\sim 3 \times 10^{14} \text{ W/cm}^2$ and a wavelength of ~ 800 nm. For linear polarized light, two distinctive KER peaks appear at 3.8 eV and 5.3 eV. Interestingly, compared to the single photon experiment described above, the contribution at higher KER is only about 7 % in intensity of the other, making the dissociation at the neutral internuclear separation the most probable. The suggested mechanism, leading to the higher KER contribution implied here, too, is RCT proceeding via a one-site doubly-ionized state. The difference is that, similar to electron impact ionization at the present energy, this state cannot be reached by intermediate Auger decay but is populated directly.

For the dashed-blue contribution at 3.76(9) eV, on the other hand, a direct coupling to the dissociative state seems the most likely. An intuitive picture of such a process can be given in terms of a sequential ionization, where the projectile ionizes

⁸The corresponding single ionization cross-section is $2.98 \times 10^{-16} \text{ cm}^2$ with a contribution of the $(3p^{-1})$ channel of 94 %, which is roughly an order of magnitude larger.

the target in two steps, one constituent after the other. Of course, this should be reflected by the reconstruction of the alignment of the dimer axis at the time of the interaction. If the projectile interacts twice, once at each center, the process should be most efficient if the dimer is aligned parallel to its direction. This process corresponds to an IP of 35.3 eV.⁹ It constitutes the second KER peak – Coulomb explosion of the dimer at equilibrium internuclear distance – that was found by Manschwetus et al. [Manschwetus et al. (2010)]. There, it is interpreted as sequential two-site field ionization leading to a pronounced alignment of the ionic fragments with respect to the laser polarization.

A second, ultra-fast and efficient process that is known to lead to dissociation is ICD (see section 2.3.1). This type process sees the dimer as closely adjacent but individual atoms. Resembling Auger decay, which takes place between the dimer constituents, the energy of the decay is transferred to the neighboring atom, which is ionized. Naturally, the argon dimer is not the subject of ICD that leads to a doubly-charged final state. This is owed to the fact that the removal of a $3s$ electron and the subsequent transition $3p \rightarrow 3s$ – the energy difference being 13.5 eV – is not sufficient to valence-ionize the neighboring atom ($V_{\text{IP}}(\text{Ar}^+) = 15.76$ eV). The only possibility to invoke ICD by inner-shell ionization is the removal of a $2p$ electron. Following a one-site Auger to $\text{Ar}^{2+}(3s^{-1}3p^{-1}) + \text{Ar}$, ICD can take place creating a triply-charged final state (see next section). There is, however, also the possibility of invoking ICD by creating an excited state by simultaneous ionization and excitation in the outer-shell, as mentioned in section 2.3.1 [Lablanquie et al. (2007)]. A schematic view of this process is depicted in Fig.2.7. After populating a $\text{Ar}^{2+}(3p^{-2}nl) + \text{Ar}$ satellite state, the repulsive potential curve (red) is reached by virtual photon exchange. The direct process described above corresponds to an immediate population of the $\text{Ar}^+ + \text{Ar}^+$ state. In the publication by Lablanquie et al. no electron spectra were presented and hence no unambiguous proof of such a process was given [Lablanquie et al. (2007)].

Further investigation in the underlying mechanisms can be done by looking at the angular distributions of the ionic fragments. Such distributions are shown in Fig. 5.15 for the two main contributions. While panel (a) shows the angular distribution related to $R_{\text{int.}} = 3.83(1) \text{ \AA}$, panel (b) shows the angular distribution for

⁹ $V_{\text{IP}}(\text{Ar}_2^{2+}) = 2V_{\text{IP}}(\text{Ar}^+) + E_{\text{KER}}$.

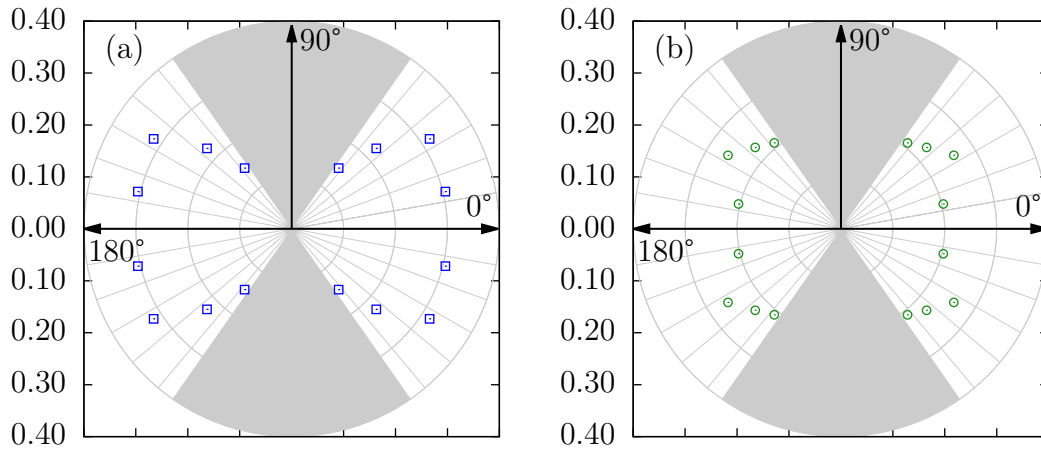


Figure 5.15.: Angular distributions of ionic fragments for KER distribution from Fig. 5.14(a). Panel (a) shows the distribution for $R_{\text{int.}} = 3.831(96) \text{ \AA}$ while panel (b) for $R_{\text{int.}} = 2.822(69) \text{ \AA}$. Gray-shaded region indicates areas of reduced acceptance.

$R_{\text{int.}} = 2.82(7) \text{ \AA}$. The gray-shaded areas mark regions of reduced acceptance of the detector due to the comparable TOFs of the fragments for 90° emission, which prevents a distinction. The integral value of each dataset has been normalized to one. For the doubly-charged final state, due to the symmetry in charge and mass, only the angular region between 180° and 90° can be accessed.¹⁰ Each angle smaller than 90° corresponds to an angle larger 90° for the other corresponding fragment of the breakup, due of the cylindrical symmetry of the spectrometer. Hence, the data in Fig. 5.15 has been mirrored to grant a better visualization.

While it is difficult to explain the actual shape of the distribution, a number of features can be extracted. First and foremost it is apparent that the data for panel (a) has a greatly enhanced probability for the Coulomb explosion of the dimer to take place with the molecular axis oriented along the projectile direction. This agrees with the possibility that a dimer breakup at the neutral internuclear distance can occur by sequentially ionizing the two constituents. For the other possible process, the ICD, the breakup is not the result of a double collision and should therefore not reflect this symmetry. In other words, one would expect an isotropic distribution. Since, one has to assume that two competing processes can reach the

¹⁰In the laboratory system the electron detector is in the z -direction which corresponds to a polar angle 0° (see Fig. 3.1).

same final state, the distribution in panel (a) should consist of both features. Due to the limited acceptance in the perpendicular direction, this effect cannot directly be observed. Additionally, it is difficult to find a signature of the ICD process in terms of the correlation of the electron energy with the KER. The problem is that in general the probability of creating low energy electrons in electron impact experiments is high. Hence, the direct ionization process will add to the low energy end just like a possible ICD process would, making it essentially a matter of the partial probability of the processes whether or not they can be distinguished. One can gain an idea of the probability of the necessary simultaneous ionization and excitation process by looking at the cross-sections. Generally, cross-sections for processes that leave the argon ion in an excited state are in the order of 10^{-19} cm² [Tan and McConkey (1974)]. If one adds up all the states above the ICD threshold, the cross-section increases two orders of magnitude. This is about the same scale as the cross-section for $3p$ double ionization, which will invoke RCT and lead to a different KER. From the data at hand, the most likely conclusion is that dimer breakup to a doubly-charged final state is reached by a sequential ionization process of the two constituents. However, ICD as a second competing mechanism can not be ruled out to contribute as well.

For the breakup to occur at a smaller internuclear distance and the corresponding distribution in panel (b), the situation is different. If the mechanism required to invoke RCT takes place at one of the two scattering centers by double ionization, the dissociation itself should not be bound by the direction of the initial ionization, hence, the probability should not be enhanced by a specific alignment of the dimer with respect to the projectile at the time of the collision. Additionally, the radiation lifetime of the intermediate $\text{Ar}^{2+} + \text{Ar}$ state is long compared to the interaction time. While the interaction takes place in the order of fs, the radiative lifetime is in the order of several ns [Zaitsevskii and Dement'ev (1991)]. The resulting distribution of the fragments should consequently be isotropic. Indeed, looking at the distribution in panel (b) it is essentially independent of the projectile direction, especially when compared to panel (a). The conclusion here is that the dissociation proceeds via a one-site doubly-charged state as depicted in Fig. 2.8, which subsequently undergoes RCT.

5.2.2. Triply-charged Final State: $\text{Ar}^{2+} + \text{Ar}^+$

For the triply charged final state, the situation improves with respect to the experimentally accessible angular range of the detected ion. Since now the charges of the fragments are different (but the masses are still equal), the higher charged one – the Ar^{++} – arrives earliest without regarding its initial emission angle. Hence, over the complete polar range of 180 to 0° the doubly charged ion is distinguishable and orientation information could be acquired. Additionally, this particular breakup does, obviously, not exhibit equal TOFs of the fragments for 90°-emission. This means in particular that the angular acceptance, which was significantly reduced for the symmetric doubly-charged final state, is greatly enhanced.

Looking at the KER distribution in Fig. 5.14(b), only one pronounced feature is observable which peaks at an energy of 7.42(5) eV. This peak is associated with an internuclear separation at the time of the dissociation of $R_{\text{int.}} = 3.88(3) \text{ \AA}$. Although slightly larger, it still coincides with the neutral dimers separation, indicating a swift Coulomb explosion that leaves the ion little time to contract. The fact that the peak position is shifted to a larger internuclear distance is mainly due to the fact the peak shape is asymmetric and in order to perform a fit, two Gaussians had to be used to account for the shape. It is, however, not likely that two discrete features are embedded which would shift the peak position slightly to a higher KER, giving a closer match to the neutrals internuclear distance.

In order to create a triply-charged final state in Ar_2 , the ionization potential for the direct preparation is 59.15 eV and related to the sequential ionization to $\text{Ar}^{2+}(3p^{-2}) + \text{Ar}^+(3p^{-1})$. If one assumes double ionization to take place first, for which the cross section at 120 eV is $\sigma(3p^{-2}) = 2.48 \times 10^{-17} \text{ cm}^2$, the projectile is left with, at the most, 76.61 eV.¹¹ For the subsequent single ionization, the cross-section is then $\sigma(3p^{-1}) = 3.48 \times 10^{-16} \text{ cm}^2$, which is only slightly below the maximum of the cross-section of $\sigma(3p^{-1})_{\text{max}} = 2.73 \times 10^{-16} \text{ cm}^2$ at 49.5 eV [Jha et al. (2006)]. If one were to reverse the order, the single ionization cross-section drops in favor of an increased double ionization cross-section. The likelihood of such an event, however, would additionally depend on the probability for the scattered projectile to interact with the remaining constituent, which, in turn, would depend on the orientation. Geometrically, the fraction of the complete solid angle covered by the other argon

¹¹ $V_{\text{IP}}(3p^{-2}) = 43.39 \text{ eV}$ [Ralchenko et al. (2011)].

atom in the dimer is 6.7%.¹²

Another possible pathway for a triply-charged final state is reportedly through ICD [Morishita et al. (2006); Santra and Cederbaum (2003); Ueda et al. (2007)]. In the performed photoionization experiments, ICD takes place after an one-site Auger decay into a $\text{Ar}^{2+}(3s^{-1}3p^{-1}) + \text{Ar}$ state. The ionization potential to prepare such a state directly by electron impact is with 61.23 eV 17.85 eV above the $\text{Ar}^{2+}(3p^{-2})$ threshold [Ralchenko et al. (2011)]. In order to be subject to ICD, the difference of the $(3p^{-2})$ and the $(3s^{-1}3p^{-1})$ states has to be larger than the single ionization potential. The first possible configuration which accomplishes this is the 1P at 17.85 eV. This state is mixed with the $(3p^{-3}3d)^1P$. Considering that it involves the interaction of an inner-shell, the cross-section is expected to decrease. In fact, the theoretical value at 120 eV is $\sigma(3s^{-1}3p^{-1}) = 0.31 \times 10^{-17} \text{ cm}^2$, which is 12.5 % of the cross-section for removal of two valence electrons. The dissociation then proceeds by transition of an $3p$ electron to the $3s$ hole where the excess energy is then transferred to the neutral constituent. Intuitively, one assumes such a process more probable than two subsequent collisions and consequently, the ICD process should dominate the fragmentation.

To investigate the mechanism leading to the triply-charged final state, the possible correlation between the KER and the electron energy gives valuable insight. In Fig. 5.16 the KER is plotted against the electron energy. The focus here is set on the lower end of the energy scale in order to be sensitive for the electrons that are emitted during ICD. Depending on the initial state that de-excites, the excess energy of the $3p$ electron is expected to be of only a couple eV. It has been indicated in section 2.3.1 that the KER and the energy of the ICD electron will have to be correlated. Therefore, in Fig. 5.16, an ellipse is plotted with an angle of -45° with respect to the x -axis and enclosing the peak structure. The combined energy of the ICD electron and the KER is 9.9 eV, which is indicated by the dashed line.

Indeed, the KER does show a correlation with the electron energy indicating that the underlying process leading to the dissociation is ICD where, in contrast to photoionization experiments, the starting point was not an inner shell hole. Instead, the intermediate $(3s^{-1}3p^{-1})$ state is reached directly. It should, however, not be concealed that due to the rather high spectrometer extraction field that was neces-

¹²By taking into account a van der Waals radius of 1.88 Å.

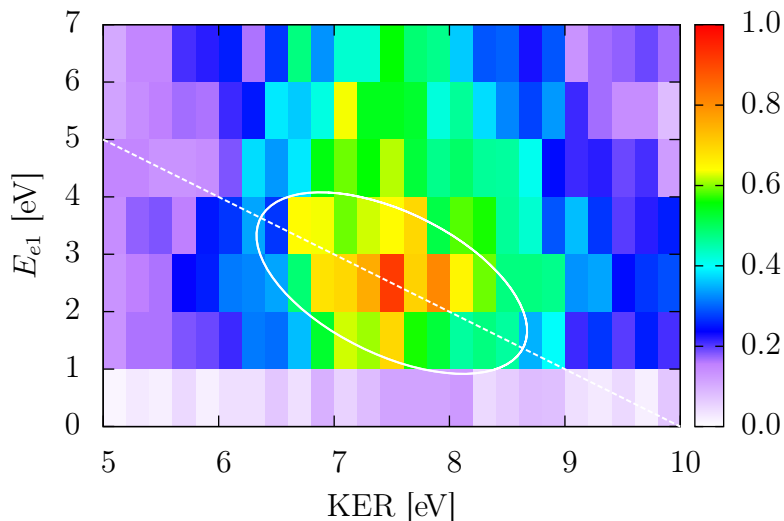


Figure 5.16.: KER vs. electron energy E_{e1} . The white ellipse is tilted by -45° with respect to the x -axis. The dashed line denotes the electron-KER correlation for a combined energy of 9.9 eV.

sary to provide enough acceptance for the ionic fragments, the energy resolution – especially for the electrons – did suffer (cf. section 4.5.1).

Now, it can be investigated how the dimer breaks up in the laboratory system by looking at the angular distribution of the Ar^{2+} fragments. Figure 5.17 shows two such plots. Both correspond to the main peak at $R_{\text{int.}} = 3.88(3) \text{ \AA}$. While panel (a) shows the angular distribution of the slow emitted electrons in the system of the dimer, panel (b) shows the actual distribution of the Ar^{2+} . For the implied process leading to this particular feature, ICD, the first expectation would have been that it leads to an isotropic distribution in the lab system. As it has been described above, to invoke the dissociation it is sufficient to interact with one of the dimer constituents and the breakup itself, although fast, should take place independently of the projectile. Looking at the distribution in panel (b) it shows a pronounced elongation along the spectrometer axis. Of course, even if a signature for ICD has been found in terms the correlation between the KER and E_{e1} , it does not rule out the the probability of a sequential ionization process. Therefore, the angular distribution of the Ar^{2+} fragments can include both signatures: an isotropic component

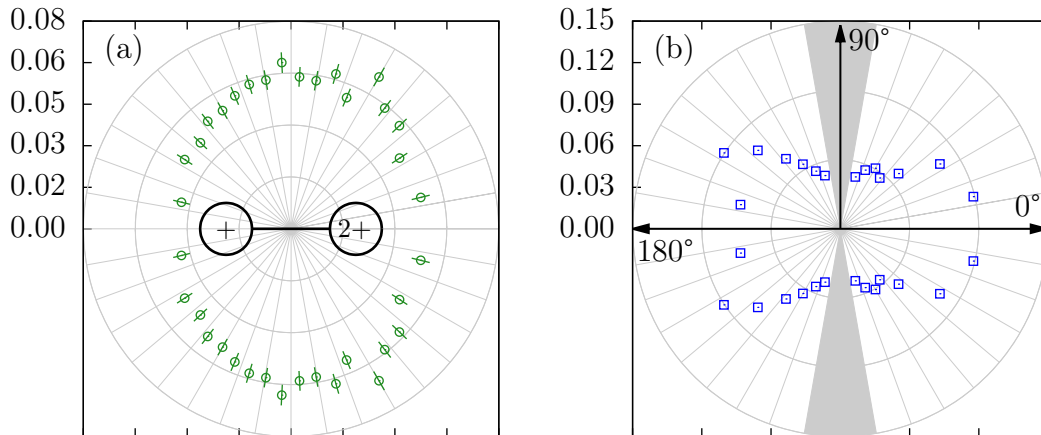


Figure 5.17.: Angular distributions of ionic fragments for KER distribution from Fig. 5.14(b). Both panels show the distribution related to an internuclear separation of $R_{\text{int.}} = 3.880(25) \text{ \AA}$. Panel (a): electron distribution in molecular frame with an additional condition on the electron energy from 1 eV to 4 eV. Panel (b) shows the corresponding ionic distribution in the lab system. Gray-shaded region indicates areas of reduced acceptance.

and an aligned component. At this stage, it is extremely difficult to separate the two contributions. Unlike photoionization, the ejected electrons in electron impact ionizations experiments are not subject to discrete energies. On top of that, especially for double ionization, the probability for the ejected electrons to be of low energy is large. As an example, Fig. 5.17(a) shows the angular distribution of the electrons for identical internuclear distance as in panel (b) but with a condition on the energy to be between 1 eV to 4 eV. The direction of the doubly-charged fragment is also indicated. This distribution turns out to be mainly isotropic with a slight tendency for emission perpendicular to the internuclear axis.

5.2.3. Doubly-charged Trimer Breakup: $\text{Ar}_2^+ + \text{Ar}^+$

The bottom panel (c) in Fig. 5.14 distinguishes itself from the above by the fact that the parent cluster was not a dimer but a trimer, following the reaction $\text{Ar}_3 \rightarrow \text{Ar}_2^+ + \text{Ar}^+$. While it is not obvious that this channel can be assigned to the data judging from Fig. 5.13, a closer look provides significant evidence. In Fig. 5.18

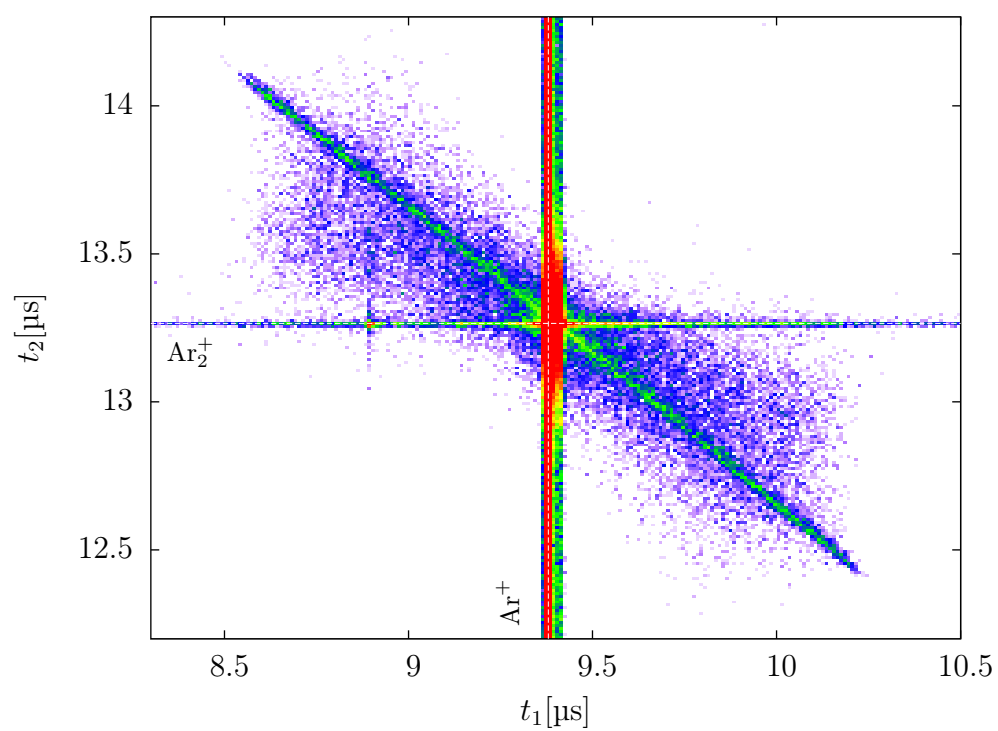


Figure 5.18.: Magnified TOF coincidence signal between argon dimer ions and monomer ions.

the area between $8.2\ \mu\text{s}$ to $10.5\ \mu\text{s}$ and $12.3\ \mu\text{s}$ to $14.2\ \mu\text{s}$ TOF is magnified. One can see the ion signal centered around the zero-momentum TOFs of Ar_2^+ and Ar^+ [Rühl et al. (1994)]. As explained above, the horizontal and vertical lines are false coincidences between a fragment from an actual dissociation and an uncorrelated fragment. Here, the major contribution is likely to be from dimer ions where the trimer breaks up into a singly charged final state ($\text{Ar}_2^+ + \text{Ar}$) [Bonhommeau et al. (2006, 2007)]. The actual coincidence signal consists of two contributions that both experience a negative slope, the *background* that is distributed over some area and the sharp line. The so-called background originates from an actual dissociation, meaning that the measured ions belong to the same breakup. The spread comes from an unaccounted fragment that could be either charged or neutral. For example one could imagine a quatromer to dissociate to a dimer and a monomer ion plus a neutral atom: $\text{Ar}_4 \rightarrow \text{Ar}_2^+ + \text{Ar}^+ + \text{Ar}$. The sharp line structure, on the other hand, indicates that the momentum of the measured fragments has been conserved and the breakup was indeed that of a trimer into $\text{Ar}_2^+ + \text{Ar}^+$. Structurally, the neutral trimer is by most accounts assigned to a shape of an equilateral triangle with a bond length of $3.8\ \text{\AA}$, while the stable singly-charged trimer ion is assumed linear with a bond length of $2.5\ \text{\AA}$ [Gadea et al. (1994); Gonzalez-Lezana et al. (1999); Kuntz and Hogreve (1991); Lara et al. (1995)]. The trimer was recently found to be subject to ICD, similar to the way described for the triply-charged final state for the argon dimer, resulting in a 3Ar^+ final state [Liu et al. (2007)].

The corresponding KER to this channel is depicted in Fig. 5.14(c). It shows a main contribution at $3.68(3)\ \text{eV}$ and a broad shoulder extending to lower KER. In this case, of course, the trimers KER cannot be mapped to the internuclear separation directly since some of the energy might also be converted into rotation. On the other hand, it is compelling that the internuclear separation given by the reflection principle is $R_{\text{int.}} = 3.91(4)\ \text{\AA}$ for the main KER peak, pretty much exactly the bond length of the triangle. Of course, in the simplest picture, one can imagine the trimer to dissociate along the height of the triangle with the dimer ion on one end and the monomer ion on the other. The corresponding angular distributions are presented in Fig. 5.19. In panel (a) the electron distribution with respect to the monomer ion is plotted with an additional condition for the electron energy, restraining it to a low energy region between $1\ \text{eV}$ to $4\ \text{eV}$. Obviously, these electrons show no relation to the direction of the Ar^+ fragment and exhibit a almost perfectly isotropic emission.

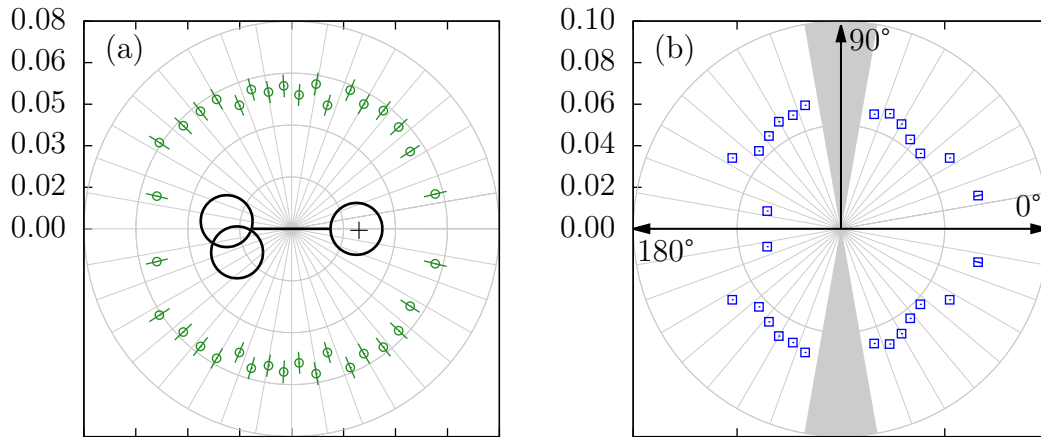


Figure 5.19.: Angular distributions of ionic fragments for KER distribution from Fig. 5.14(c). Data in both panels are related to a KER of 3.680(34) eV. Panel (a): electron distribution in the frame of the monomer ion with an additional condition on the electron energy from 1 eV to 4 eV. Panel (b) shows the corresponding ionic distribution for Ar^+ in the lab system. Gray-shaded region indicates areas of reduced acceptance.

The ion in panel (b), on the other hand seems to prefer the direction of the projectile or the orthogonal direction with a dip in the 45° direction.

6. Summary and Outlook

The purpose of this work was to present an overview of electron impact ionization on van der Waals clusters composed of argon and neon. This specific class of target species was chosen since they present an intermediate state between sole constituents and macroscopic matter. In order to do a thorough examination, the work was split into two different parts: one for single ionization, and another, where the target is dissociated into two charged particles that subsequently undergoes Coulomb explosion. The first part was carried out as a kinematically complete experiment, where all charged final state fragments are detected and their momenta are reconstructed. For the study of dissociation the two ionic fragments were detected in coincidence with one electron. Since the number of charged fragments in the final state always includes the number of created fragments plus the projectile, these experiments were not kinematically complete.

Experimentally, the studies that were carried out by the use of a reaction microscope, which was specifically modified for electron impact studies. In particular the preparation of the target by supersonic expansion naturally gives rise to cluster formation and was integral to this work. Furthermore, the experimental technique made it possible to acquire data for several cluster sizes in a single run of the experiment and as such under identical conditions. Consequently, the ionization of different targets are comparable with a very high sensitivity. On top of that, the spectrometer is highly efficient, having a an acceptance of almost the complete 4π solid angle. This is an enormous advantage given that the abundance of small clusters after expansion is only of few percent with respect to the monomers. In principle, all charged particles that emerge from a collision can be detected and their momenta are determined with high precision. Especially for the ions from a $(e, 2e)$ collision the acceptance is 4π . Compared to previous setups, the part of the spectrometer responsible for ion detection was modified to enable time-focusing conditions to improve the momentum resolution of the ions. For dissociative ioniza-

tion, where the cluster Coulomb explodes, the ionic fragments obtained very large momenta of up to 100 a.u. Full coverage of the solid angle required much larger fields, which, in turn, reduced the electron momentum resolution. To still be able to detect the ionic fragment a special detector was designed. The emission direction is now isotropic with respect to the azimuthal angle, due to the much larger momenta compared to the initial momentum gained during the supersonic expansion. This new detector design distinguishes itself from a hexanode with hole (cf. [Senftleben (2009)]). First, the position sensitive anode does not contain any gaps which have to be accounted for and, furthermore, the readout of the anode is much simpler, since it does not require complex timing electronics.

The $(e, 2e)$ studies on argon were carried out with an intermediate projectile energy of 100 eV. The investigated targets were atoms, dimers and small clusters. The latter are not stable upon ionization and dissociate almost exclusively into dimer ions. They represent all remaining sizes larger than dimers that are contained in the jet. For all targets the removal of a $3p$ valence electron was studied. Additionally, the cluster target revealed a channel where a neutral constituent is left in an excited state. The atomic target, too, revealed a series of excitations that were absent for the dimer. This is seen as a first hint towards fragmentation processes that appear prominently in the dimer. The partially integrated differential cross-sections were compared and revealed an enhanced out-of-plane emission of electrons with increasing target size, pointing to an enhanced probability of elastic scattering. For the excitation of the cluster, the cross-section was expectedly strongly isotropic. Here, the angular correlation between the final state electrons no longer exists due to the additional inelastic process. Furthermore, with the target size, the probability for emission of the ejected electron in the direction of the scattered projectile was increased, indicating a reduction of PCI due to the presence of the cluster.

For $(e, 2e)$ on argon atoms and dimers, triple-differential cross-sections were obtained and compared. For the ionization of the dimer, this very accurate look into the phase space revealed an enhanced emission into the backwards hemisphere for a coplanar arrangement, while the emission into non-coplanar geometries was enhanced. These findings could not be related to the rather simple two-center interference model for randomly aligned molecules. The chosen energy of the emitted electron was placed in the maximum of the elastic scattering cross-section, which apparently maximized the probability of an additional scattering process at the

other dimer constituent. The atomic data sets were compared to a plain distorted wave calculation with PCI treatment by means of the Gamow factor and a hybrid R-matrix model. While the latter achieved satisfactory agreement in the scattering plane, the same for the DWBA can only be achieved by inclusion of PCI. Overall, the agreement is only mediocre which can, on one hand, be attributed to the complexity of the target and on the other hand is owed to the low projectile energy.

Similar studies as for argon were carried out for neon at an even lower projectile energy of 61 eV. Neon has only half the mass of argon and its dimer has a smaller internuclear distance of 3.1 Å. The experimental triple-differential cross-section were compared to a theoretical model for atomic neon. Therein, the final state correlation was added in terms of the Gamow factor, whereas in the plain first-order it is neglected. Consequently, the plain model did poorly for the angular regions of the scattered projectile. With inclusion of PCI, the shape improves tremendously, leading to sound agreement in the scattering plane. For the remaining geometries, the agreement is only mediocre. The comparison between the atomic and dimer data revealed less deviation as compared to the argon experiment for the scattering geometries that were chosen. Instead of a generally enhanced emission in the perpendicular plane, now only distinct enhancements for special angular ranges were found. The full-perpendicular plane revealed a distinct suppression in the direction perpendicular to the momentum transfer. By looking at the three-dimensional 3DCS, two prominent lobes appear which are located in between the scattering plane and the perpendicular plane. By comparing the shape of the photoionization cross-section for neon dimers a strong indication of molecular symmetry participation in the ionization process is apparent.

Lastly, Coulomb explosion of small argon clusters at 120 eV was studied, where two ions were detected in coincidence with an electron. The studied dissociation channels were the doubly-charged final state ($\text{Ar}^+ + \text{Ar}^+$) and the triply-charged final state ($\text{Ar}^{2+} + \text{Ar}^+$) for argon dimers. Furthermore, the doubly-charged final state ($\text{Ar}_2^+ + \text{Ar}^+$) of the argon trimer was observed. For all channels, kinetic energy release spectra and angular distributions for the ionic fragments were presented.

For the doubly-charged final state of the dimer two main peaks apparent in the KER spectrum which can be assigned to different mechanisms. The main contribution which corresponds to the Coulomb explosion taking place at the equilibrium internuclear distance of the neutral dimer and one contribution corresponding to a

smaller internuclear distance. While for the main peak the main mechanism was found to be sequential ionization of the two constituents. This was illustrated by favored alignment of the dimer parallel to the projectile direction. Generally, ICD should also be possible to create a doubly-charged final state, however, due to reduced resolution for the electrons this could not convincingly be identified. On the other hand, the ion's angular distribution show a significant component perpendicular to the projectile direction, which can indicate an underlying isotropic distribution. The peak at smaller internuclear separation was assigned to radiative charge transfer (RCT) after double ionization of one constituent. This is reflected in the isotropic angular distribution of the ions since now the dissociation is a secondary process, taking place after the ionization.

The triply-charged final state of the argon dimer shows only a single peak in the KER spectrum and it corresponds to the equilibrium internuclear separation. The possible mechanisms to reach this final state are again sequential ionization, but now a double ionization has to follow a single ionization or vice versa, and ICD by one-site double ionization, which includes an inner valence shell electron. A spectrum of the electron energy correlation versus the KER reveals a correlation which matches the proposed sum energy ($E_{e2} + \text{KER}$) for this process, hence, pointing out that ICD is in fact taking place. The angular distribution for the doubly-charged fragment shows an elongation parallel to projectile direction. This indicates, that also sequential ionization is taking place.

Finally, the doubly-charged trimer breakup was studied and showed a more complex KER spectrum than the previous examples. This is mainly owed to the fact that the configuration of the neutral trimer is an equilateral triangle and the breakup into a dimer ion and a monomer ion is not expected to take place back-to-back, as it is the case for diatomic species. Consequently, the KER does generally not reflect the internuclear separation. The angular distribution of the monomer ion shows an enhancement in the projectile direction and perpendicular direction, separated by a dip. This points towards discrete orientations for the breakup with respect to the projectile. From the data at hand, their origin could not be explained.

To summarize, electron impact ionization of small rare gas cluster was examined and for the first time 3DCSs are presented in a kinematically complete experiment and deviations were found from the corresponding atomic cross-sections. On one hand this is due to enhanced elastic scattering in argon off neighboring atoms, on

the other hand, in neon, it they are assigned to effect of molecular orbitals and the resulting symmetry properties. For dissociative ionization of argon, several fragmentation pathways were found. The underlying mechanisms are sequential ionization of the constituents as well as interatomic decay processes such as ICD and RCT which are invoked by one-site double ionization and lead to triply-charged and doubly-charged final states, respectively.

In the future, experimentally, an improved control over cluster creation, e.g., by means of temperature stabilization of the expanding gas, would be a significant step. Ultimately, a size selected cluster target would provide great insight into parent sizes that are known to dissociate, but it remains to be proven whether the effective target density will allow for reasonable runtime of the experiment. For the case of Coulomb exploding clusters, the biggest issue is the improvement of the resolution by either shortening the ion side of the spectrometer further or re-accelerating the fragments in a second acceleration stage, to allow for lower fields for the electron extraction. For dedicated experiments the use of hexanode detector for the ions would improve the acceptance due to its multi-hit capability. On the theoretical side, the lack of calculations for dimer ionization proves to be troublesome, especially in the case of neon. This is understandable given the complexity of the dimer. Dedicated electron impact calculations, however, would be of great help to shed some light, e.g., on the influence of molecular orbitals to the cross-section. Hopefully, in the future it is possible to close this gap.

A. Atomic Units

Physical quantity	a.u.	SI units		Special
mass	m_e	9.1094×10^{-31}	kg	1823^{-1} amu
ang. mom.	\hbar	1.0546×10^{-34}	J s	
charge	e	1.6022×10^{-19}	C	
length	a_0	5.2918×10^{-11}	m	0.53 Å
energy	E_h	4.3597×10^{-18}	J	27.2141 eV
time	\hbar/E_h	2.4189×10^{-17}	sec	
velocity	v_0	2.1877×10^6	m/s	
momentum	$m_e v_0$	1.9929×10^{-24}	kg m/s	
el. pot.	E_h/e	27.211	V	

p_e [a.u.] = $0.27 \cdot \sqrt{E$ [eV]	$1 \text{ eV} \hat{=} 8065.66 \text{ }^1/\text{cm}$
B [Gs] = $357/T_{cyc}$ [ns]	$1 \text{ amu} \hat{=} 1.66 \times 10^{-27} \text{ kg}$
r_e [mm] = $33.7 \cdot \sqrt{E$ [eV]/ B [Gs]	

Table A.1.: Conversion factors for atomic units and relevant formulas scaled to appropriate units.

Commonly in atomic physics, the scale of the SI system is ill-suited. For once, the energy scale is very small compared to the energies that usually occur, while on the other hand, the length scale too large compared to the atomic scale. As a consequence, all units are adapted to the natural dimension of the hydrogen atom and the electron mass m_e and charge e . All these quantities listed in table A.1 together with their conversion factor are assigned as one *atomic unit* with the abbreviation a.u. Additionally, handy conversion formulas of important properties are listed.

B. Charge-Sensitive Amplifier

In the following, construction information is gathered for a three-channel charge-sensitive preamplifier. It was constructed and used to operate the wedge-and-strip anode (section 3.2.3). The construction is based on the commercially available charge amplifier module CR-11x, manufactured by Cremat.¹ The general design considerations were based on availability, performance and cost. Consequently, all parts used are readily available.

#	№	Value	Stock
3	CON1...3	SIL-8	
1	CON4	PM 5.08/3/90 3.5	↔ RS
1	Q1	2N3904	
1	Q2	2N3906	
2	D1,2	7.5V Zehner	
2	D3,4	1N4148	
2	R11,12	2k2	
4	R7...10	1M/0.5W VR37	↔ RS
3	RO1...3	50M/2kV HTS68	↔ RS
7	C15...18; CO1...3	4n7/3.5kV	
2	C7,8	10μ/63V elko	
6	C1...6	0.1μ 1210	
6	C9...14	10μ/16V X5R 1210	↔ RS
6	R1...6	4R7 1210	

The power-supply was designed compatible to the NIM-standard² for seamless integration into existing hardware, accepting input voltages from ± 10 V to ± 25 V.

Figure B.1 shows the circuit diagram, the corresponding layers and parts placement of the double-sided circuit board are shown in Fig. B.2. It was designed to accept three modules, one for each electrode of a common wedge-and-strip anode, allowing operation with a single amplifier box.

¹<http://www.cremat.com>

²Nuclear Instrumentation Module.

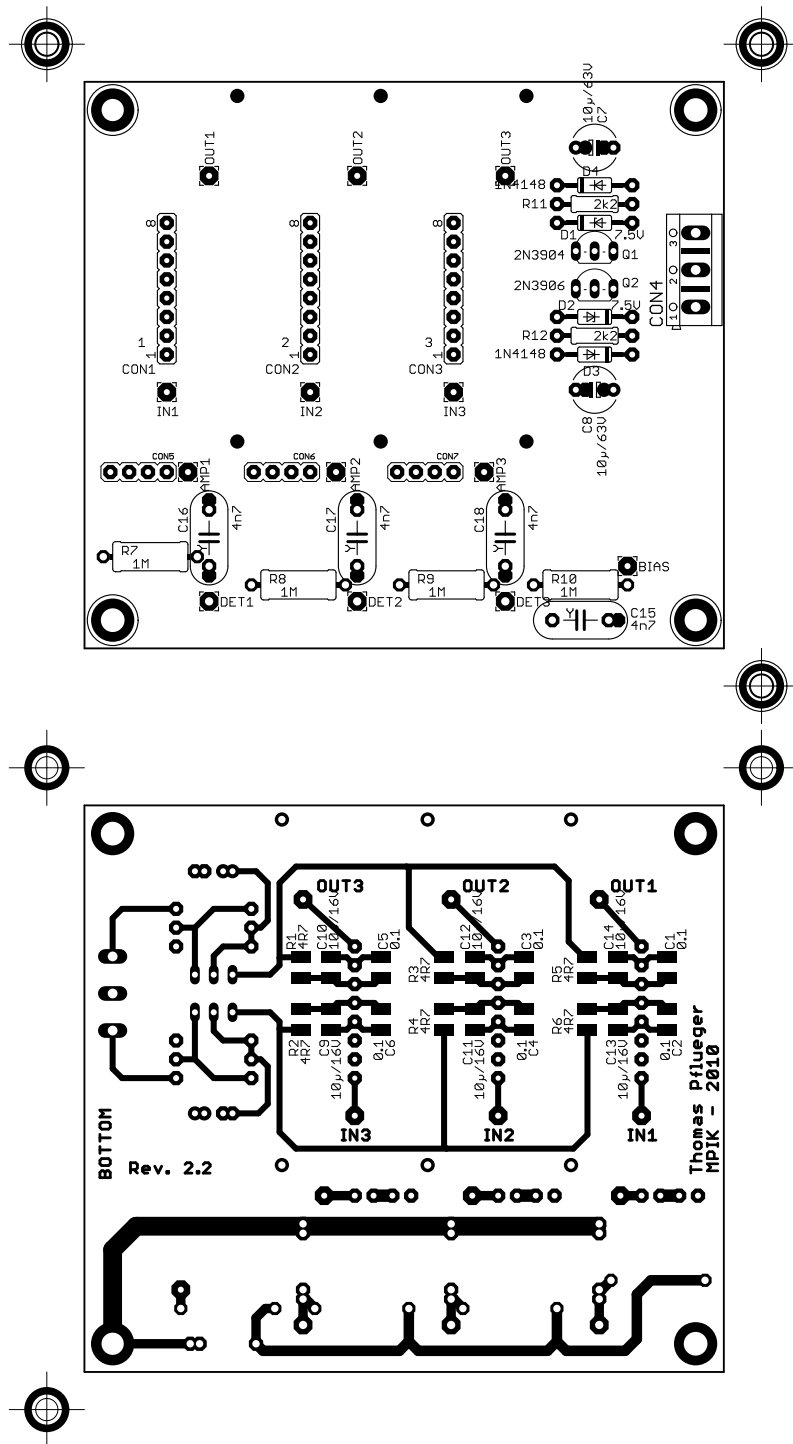


Figure B.2.: Top and bottom layers of the circuit board design.

Bibliography

- Al-Hagan, O. et al. (Jan. 2009). “Atomic and molecular signatures for charged-particle ionization”. In: *Nat Phys* 5, pp. 59–63.
- Amami, S. M. and D. Madison (2011). Private communication.
- Auger, P. (1925). “Sur l’effet photoélectrique composé”. In: *J. Phys. Radium* 6, pp. 205–208.
- Averbukh, V. et al. (2004). “Mechanism of Interatomic Coulombic Decay in Clusters”. In: *Phys. Rev. Lett.* 93, p. 263002.
- Bartlett, P. L. and A. T. Stelbovics (2002). “Calculation of electron-impact total-ionization cross sections”. In: *Phys. Rev. A* 66, p. 012707.
- Bartschat, K (2009). Private communication.
- Bartschat, K and P. G. Burke (1987). “The R-matrix method for electron impact ionisation”. In: *Journal of Physics B: Atomic and Molecular Physics* 20, p. 3191.
- Bartschat, K. and O. Vorov (2005). “Channel-coupling, target-structure, and second-order effects in electron-impact ionization of $Ar(3p)$ and $Ar(3s)$ ”. In: *Phys. Rev. A* 72, p. 022728.
- Bastida, A. et al. (Jan. 1996). “Electron impact ionization of small argon clusters”. In: *Chemical Physics Letters* 249, pp. 1–6.
- Bell, K. L. and A. E. Kingston (1975). “The angular and energy distributions of electrons ejected in the ionization of helium atoms by protons and electrons”. In: *Journal of Physics B: Atomic and Molecular Physics* 8, p. 2666.
- Bloom, E. D. et al. (1969). “High-Energy Inelastic $e - p$ Scattering at 6° and 10° ”. In: *Phys. Rev. Lett.* 23, pp. 930–934.
- Bonhommeau, D. et al. (2006). “Fragmentation dynamics of argon clusters (Ar_n , $n = 2$ to 11) following electron-impact ionization: Modeling and comparison with experiment”. In: *The Journal of Chemical Physics* 124, p. 184314.

- Bonhommeau, D. et al. (2007). “Fragmentation of rare-gas clusters ionized by electron impact: new theoretical developments and comparison with experiments.” In: *International Reviews in Physical Chemistry* 26, pp. 353–390.
- Botero, J. and J. H. Macek (1992). “Threshold angular distributions of $(e, 2e)$ cross sections of helium atoms”. In: *Phys. Rev. Lett.* 68, pp. 576–579.
- Brauner, M et al. (1989). “Triply-differential cross sections for ionisation of hydrogen atoms by electrons and positrons”. In: *Journal of Physics B: Atomic, Molecular and Optical Physics* 22, p. 2265.
- Bray, I. et al. (2010). “Single ionization of helium by electron impact”. In: *Phys. Rev. A* 81, p. 062704.
- Bray, I. (1994). “Convergent close-coupling method for the calculation of electron scattering on hydrogenlike targets”. In: *Phys. Rev. A* 49, pp. 1066–1082.
- Bray, I. and A. T. Stelbovics (1992). “Convergent close-coupling calculations of electron-hydrogen scattering”. In: *Phys. Rev. A* 46, pp. 6995–7011.
- Brion, C. and J. Thomson (1984). “Compilation of dipole oscillator strengths (cross sections) for the photoabsorption, photoionization and ionic fragmentation of molecules”. In: *Journal of Electron Spectroscopy and Related Phenomena* 33, pp. 301–331.
- Buck, U. and H. Meyer (1986). “Electron bombardment fragmentation of Ar van der Waals clusters by scattering analysis”. In: *The Journal of Chemical Physics* 84, pp. 4854–4861.
- Burgt, P. J. M. van der and J. W. McConkey (1995). “Detection of neutral metastable fragments from electron-impact on argon clusters”. In: *The Journal of Chemical Physics* 102, pp. 8414–8423.
- Canney, S. et al. (1997). “ $(e, 2e)$ Spectroscopy of solids with improved energy resolution”. In: *Journal of Electron Spectroscopy and Related Phenomena* 83, pp. 65–76.
- Cederbaum, L. S. et al. (1997). “Giant Intermolecular Decay and Fragmentation of Clusters”. In: *Phys. Rev. Lett.* 79, pp. 4778–4781.
- Chaudhry, A. et al. (2011). “Theoretical Approaches”. In: *Analysis of Excitation and Ionization of Atoms and Molecules by Electron Impact*. Vol. 60. Springer Series on Atomic, Optical, and Plasma Physics. Springer New York, pp. 15–36. ISBN: 978-1-4419-6947-7.
- Cherepkov, N. A. (2012). Private communication.

- Chesnel, J.-Y. et al. (2007). “Young-Type Experiment Using a Single-Electron Source and an Independent Atomic-Size Two-Center Interferometer”. In: *Phys. Rev. Lett.* 98, p. 100403.
- Cohen, H. D. and U. Fano (1966). “Interference in the Photo-Ionization of Molecules”. In: *Phys. Rev.* 150, pp. 30–33.
- Colgan, J. et al. (2002). “Time-dependent close-coupling calculations of the triple-differential cross section for electron-impact ionization of hydrogen”. In: *Phys. Rev. A* 65, p. 042721.
- Danylchenko, O. et al. (Dec. 2008). “Experimental verification of the Hagena relation for large clusters formed in a conical nozzle”. In: *Technical Physics Letters* 34, pp. 1037–1040.
- Daoud, A et al. (1985). “Coincidence study of the electron impact ionisation of neon: momentum density determination and test of various scattering models”. In: *Journal of Physics B: Atomic and Molecular Physics* 18, p. 141.
- Demekhin, P. V. et al. (2008). “Dynamics of interatomic Coulombic decay in a Ne dimer following the $K-L_1L_{2,3}(^1P)$ Auger transition in the Ne atom”. In: *Physical Review A (Atomic, Molecular, and Optical Physics)* 78, p. 043421.
- Demekhin, P. V. et al. (2009). “Interatomic Coulombic decay and its dynamics in NeAr following K-LL Auger transition in the Ne atom”. In: *The Journal of Chemical Physics* 131, p. 104303.
- Descouvemont, P and D Baye (2010). “The R -matrix theory”. In: *Reports on Progress in Physics* 73, p. 036301.
- Dorn, A. et al. (2007). “Identification of higher order contributions in three-dimensional $(e,2e)$ cross-sections for helium”. In: *Journal of Electron Spectroscopy and Related Phenomena* 161. Pp. 2–5.
- Duerr, M. (2006). “Electron Induced Break-up of Helium: Benchmark Experiments on a Dynamical Four-Body Coulomb System”. PhD thesis. Rupprecht-Karls-University of Heidelberg.
- Dunn, G. H. (1962). “Anisotropies in Angular Distributions of Molecular Dissociation Products”. In: *Phys. Rev. Lett.* 8, pp. 62–64.
- Dürr, M. et al. (2006). “Three-Dimensional Images for Electron-Impact Single Ionization of He: Complete and Comprehensive $(e, 2e)$ Benchmark Data”. In: *Phys. Rev. Lett.* 96, p. 243202.

- Dürr, M. et al. (2007). “Analysis of experimental data for ion-impact single ionization of helium with Monte Carlo event generators based on quantum theory”. In: *Phys. Rev. A* 75, p. 062708.
- Dürr, M. et al. (2008). “Higher-order contributions observed in three-dimensional ($e, 2e$) cross-section measurements at 1-keV impact energy”. In: *Phys. Rev. A* 77, p. 032717.
- Echt, O. et al. (1981). “Magic Numbers for Sphere Packings: Experimental Verification in Free Xenon Clusters”. In: *Phys. Rev. Lett.* 47, pp. 1121–1124.
- Ehrhardt, H. et al. (1969). “Ionization of Helium: Angular Correlation of the Scattered and Ejected Electrons”. In: *Phys. Rev. Lett.* 22, pp. 89–92.
- Ehrhardt, H. et al. (1982). “Triply Differential Cross Sections for the Ionization of Helium by Fast Electrons”. In: *Phys. Rev. Lett.* 48, pp. 1807–1810.
- Ehrhardt, H. et al. (1986). “Differential cross sections of direct single electron impact ionization”. In: *Zeitschrift für Physik D Atoms, Molecules and Clusters* 1, pp. 3–32.
- Foltin, M. and T. Märk (1991). “Metastable fragmentation of Ne^{+4} cluster ion initiated by excimer decay”. In: *Chemical Physics Letters* 180. Pp. 317–320.
- Foltin, M. et al. (1991). “Magic metastable decay of singly charged argon clusters”. In: *The Journal of Chemical Physics* 94, pp. 810–811.
- Franck, J. and G. Hertz (1914). “Über Zusammenstöße zwischen Elektronen und Molekülen des Quecksilberdampfes und die Ionisierungsspannung desselben”. In: *Verh. Dtsch. Phys. Ges.* 16, 457–467.
- Furtado, F. M. and P. F. O’Mahony (1989). “Double scattering in energy-sharing ($e, 2e$) reactions”. In: *Journal of Physics B: Atomic, Molecular and Optical Physics* 22, p. 3925.
- Gadea, F. X. et al. (1994). “The structure of Ar_3^+ ”. In: *Chemical Physics Letters* 223, pp. 369–376.
- Gonzalez-Lezana, T. et al. (1999). “Comparative configurational study for He, Ne, and Ar trimers”. In: *The Journal of Chemical Physics* 110, pp. 9000–9010.
- Haberland, H. (1985). “A model for the processes happening in a rare-gas cluster after ionization”. In: *Surface Science* 156, Part 1, pp. 305–312.
- Hagena, O. F. (1987). “Condensation in free jets: Comparison of rare gases and metals”. In: *Zeitschrift für Physik D Atoms, Molecules and Clusters* 4, pp. 291–299.

- Hagena, O. F. (1981). “Nucleation and growth of clusters in expanding nozzle flows”. In: *Surface Science* 106, pp. 101–116.
- (1992). “Cluster ion sources (invited)”. In: vol. 63. Bensheim (Germany): AIP, pp. 2374–2379.
- Hansen, J. E. and W Persson (1987). “A revised analysis of the spectrum of Ar III”. In: *Journal of Physics B: Atomic and Molecular Physics* 20, p. 693.
- Hargreaves, L. R. et al. (2009). “ $(e, 2e)$ study of two-center interference effects in the ionization of N_2 ”. In: *Phys. Rev. A* 80, p. 062704.
- Hargreaves, L. R. et al. (2010). “A simple method for absolute normalization of $(e, 2e)$ cross sections”. In: *Measurement Science and Technology* 21, p. 055112.
- Hergenhahn, U. et al. (Jan. 2002). “Observation of excitonic satellites in the photoelectron spectra of Ne and Ar clusters”. In: *Chemical Physics Letters* 351, pp. 235–241.
- Jahnke, T. et al. (2004). “Experimental Observation of Interatomic Coulombic Decay in Neon Dimers”. In: *Phys. Rev. Lett.* 93, p. 163401.
- Jahnke, T. et al. (Feb. 2010). “Ultrafast energy transfer between water molecules”. In: *Nat Phys* 6, pp. 139–142.
- Jha, L. K. et al. (2006). “Electron impact single and double ionization of argon”. In: *The European Physical Journal D - Atomic, Molecular, Optical and Plasma Physics* 40. Pp. 101–106.
- Johnsen, R. and M. A. Biondi (1978). “Measurements of radiative charge-transfer reactions of doubly and singly charged rare-gas ions with rare-gas atoms at thermal energies”. In: *Phys. Rev. A* 18, pp. 996–1003.
- Jönsson, C. (1961). “Elektroneninterferenzen an mehreren künstlich hergestellten Feinspalten”. In: *Zeitschrift für Physik A Hadrons and Nuclei* 161. Pp. 454–474.
- Klar, H et al. (1987). “Electron impact ionisation of atomic hydrogen at intermediate energies”. In: *Journal of Physics B: Atomic and Molecular Physics* 20, p. 821.
- Kuchiev, M. U. and S. A. Sheinerman (1989). “Post-collision interaction in atomic processes”. In: *Soviet Physics Uspekhi* 32, p. 569.
- Kuntz, P. J. and J. J. Hogreve (1991). “Classical path surface-hopping dynamics. II. Application to Ar_3^+ ”. In: *The Journal of Chemical Physics* 95, pp. 156–165.
- Lablanquie, P. et al. (2007). “Appearance of interatomic Coulombic decay in Ar, Kr, and Xe homonuclear dimers”. In: *The Journal of Chemical Physics* 127, p. 154323.

- Lahman-Bennani, A. et al. (1986). “High momentum range of electron momentum distributions investigated by means of high energy (e, 2e) collisions”. In: *Journal of Electron Spectroscopy and Related Phenomena* 40, pp. 141–161.
- Lara, M. P. de et al. (1995). “Fragmentation of Ar_3^+ clusters via vibrational predissociation”. In: *Chemical Physics Letters* 242, pp. 336–342.
- Liu, X.-J. et al. (2007). “Evidence of sequential interatomic decay in argon trimers obtained by electron triple-ion coincidence spectroscopy”. In: *Journal of Physics B: Atomic, Molecular and Optical Physics* 40, F1.
- Madison, D. H. et al. (1977). “Triple-differential cross sections for electron-impact ionization of helium”. In: *Phys. Rev. A* 16, pp. 552–562.
- Madison, D. H. and O. Al-Hagan (2010). *The Distorted-Wave Born Approach for Calculating Electron-Impact Ionization of Molecules*.
- Manschwetius, B. et al. (2010). “Mechanisms underlying strong-field double ionization of argon dimers”. In: *Phys. Rev. A* 82, p. 013413.
- Märk, T. D. (1987). “Cluster ions: Production, detection and stability”. In: *International Journal of Mass Spectrometry and Ion Processes* 79, pp. 1–59.
- Märk, T. D. et al. (1986). “Unimolecular decay of metastable Ar cluster ions. Evolution of magic numbers in Ar cluster mass spectra”. In: *International Journal of Mass Spectrometry and Ion Processes* 74, pp. 281–301.
- McCarthy, I. E. and E Weigold (1995). *Electron-atom collisions*. Vol. 5. Cambridge Monographs on Atomic, Molecular, and Chemical Physics. Cambridge University Press.
- Messiah, A (1999). *Quantum Mechanics*. Vol. 2. Dover Publications Inc.
- Mielewska, B. et al. (2004). “Differential cross sections for elastic electron scattering in argon over the angular range 130° – 180° ”. In: *Phys. Rev. A* 69, p. 062716.
- Miller, D. R. (1988). “Free Jet Sources”. In: *Atomic and molecular beam methods*. Ed. by G. Scoles. Vol. 1. Oxford University Press, pp. 13–53.
- Morishita, Y. et al. (2006). “Experimental Evidence of Interatomic Coulombic Decay from the Auger Final States in Argon Dimers”. In: *Phys. Rev. Lett.* 96, p. 243402.
- Nixon, K. L. et al. (2010). “Low energy (e,2e) studies of the noble gases in the perpendicular plane”. In: *Journal of Physics B: Atomic, Molecular and Optical Physics* 43, p. 085202.
- Patkowski, K. et al. (2005). “Accurate ab initio potential for argon dimer including highly repulsive region.” In: *Molecular Physics* 103, pp. 2031–2045.

- Pflüger, T. et al. (2011). “Observation of multiple scattering in ($e, 2e$) experiments on small argon clusters”. In: *Phys. Rev. Lett.* 107, p. 223201.
- Pflüger, T. (2008). “Electron impact single ionization of small argon clusters”. MA thesis. Rupprecht Karls Universität Heidelberg.
- Poterya, V. et al. (2009). “Fragmentation of size-selected Xe clusters: Why does the monomer ion channel dominate the Xe_n and Kr_n ionization?” In: *International Journal of Mass Spectrometry* 280. Pp. 78–84.
- Prideaux, A. et al. (2005). “Exchange distortion and postcollision interaction for intermediate-energy electron-impact ionization of argon”. In: *Phys. Rev. A* 72, p. 032702.
- Ralchenko, Y. et al. (2011). *NIST Atomic Spectra Database (version 4.1)*. Online.
- Rapp, D. and P. Englander-Golden (1965). “Total Cross Sections for Ionization and Attachment in Gases by Electron Impact. I. Positive Ionization”. In: *The Journal of Chemical Physics* 43, pp. 1464–1479.
- Ray, H. and A. C. Roy (1992). “Exchange effects in electron-impact ionization of atomic hydrogen”. In: *Phys. Rev. A* 46, pp. 5714–5724.
- Reid, R. H. G. et al. (1998). “Initial-state, final-state and higher-order effects in electron impact ionization of helium atoms”. In: *Journal of Physics B: Atomic, Molecular and Optical Physics* 31, p. 563.
- Ren, X. et al. (2010). “Tracing multiple scattering patterns in absolute ($e, 2e$) cross sections for H_2 and He over a 4π solid angle”. In: *Phys. Rev. A* 82, p. 032712.
- Ren, X. et al. (2011). “Electron-impact ionization of helium: A comprehensive experiment benchmarks theory”. In: *Phys. Rev. A* 83, p. 052711.
- Rioual, S et al. (1997). “Triple differential cross sections for the electron-impact ionization of argon and neon”. In: *Journal of Physics B: Atomic, Molecular and Optical Physics* 30, p. L475.
- Rosel, T et al. (1991). “Coplanar symmetric ($e, 2e$) cross section on helium and neon”. In: *Journal of Physics B: Atomic, Molecular and Optical Physics* 24, p. 3059.
- Rühl, E. et al. (1994). “Fragmentation of doubly charged argon clusters”. In: *Zeitschrift für Physik D Atoms, Molecules and Clusters* 31. Pp. 245–251.
- Saito, N. et al. (2007). “Evidence of radiative charge transfer in argon dimers”. In: *Chemical Physics Letters* 441, pp. 16–19.

- Sakai, K. et al. (2011). “Electron-Transfer-Mediated Decay and Interatomic Coulombic Decay from the Triply Ionized States in Argon Dimers”. In: *Phys. Rev. Lett.* 106, p. 033401.
- Sakurai, J. J. (1994). *Modern Quantum Mechanics*. Addison-Wesley Publishing Company.
- Saloman, E. B. (2010). “Energy Levels and Observed Spectral Lines of Ionized Argon, Ar II through Ar XVIII”. In: *Journal of Physical and Chemical Reference Data* 39, p. 033101.
- Santra, R. and L. S. Cederbaum (2003). “Coulombic Energy Transfer and Triple Ionization in Clusters”. In: *Phys. Rev. Lett.* 90, p. 153401.
- Scharf, D. et al. (1986). “Vibrational predissociation induced by exciton trapping in inert-gas clusters”. In: *Chemical Physics Letters* 126, pp. 495–500.
- Schubert, E et al. (1979). “Triple differential cross sections for the electron impact ionisation of helium at 35 eV collision energy”. In: *Journal of Physics B: Atomic and Molecular Physics* 12, p. 967.
- Schulz, M. et al. (Mar. 2003). “Three-dimensional imaging of atomic four-body processes”. In: *Nature* 422, pp. 48–50.
- Senftleben, A et al. (2010a). “Search for interference effects in electron impact ionization of aligned hydrogen molecules”. In: *Journal of Physics B: Atomic, Molecular and Optical Physics* 43, p. 081002.
- Senftleben, A. (2009). “Kinematically complete study on electron impact ionisation of aligned hydrogen molecules”. PhD thesis. Rupprecht Karls Universität Heidelberg.
- Senftleben, A. et al. (2010b). “Fivefold differential cross sections for ground-state ionization of aligned H₂ by electron impact”. In: *The Journal of Chemical Physics* 133, p. 044302.
- Siegmund, O. H. W. et al. (1986). “Operational Characteristics of Wedge and Strip Image Readout Systems”. In: *Nuclear Science, IEEE Transactions on* 33, pp. 723–727.
- Sisourat, N. et al. (July 2010). “Ultralong-range energy transfer by interatomic Coulombic decay in an extreme quantum system”. In: *Nat Phys* 6, pp. 508–511.
- Soler, J. M. et al. (Aug. 1984). “The effect of ionization on magic numbers of rare-gas clusters”. In: *Chemical Physics Letters* 109, pp. 71–75.

- Stelbovics, A. T. (1990). “Scattering theory of close-coupling equations”. In: *Phys. Rev. A* 41, pp. 2536–2546.
- Stepanek, J. (2003). “Electron and positron atomic elastic scattering cross sections”. In: *Radiation Physics and Chemistry* 66, pp. 99–116.
- Stevenson, M. A. and B. Lohmann (2008). “Fully differential cross-section measurements for electron-impact ionization of argon over the complete in-plane angular range”. In: *Physical Review A (Atomic, Molecular, and Optical Physics)* 77, p. 032708.
- Stia, C. R. et al. (2003). “Interference effects in single ionization of molecular hydrogen by electron impact”. In: *Journal of Physics B: Atomic, Molecular and Optical Physics* 36, pp. L257–L264.
- Stolterfoht, N. et al. (2001). “Evidence for Interference Effects in Electron Emission from H₂ Colliding with 660 MeV/amu Kr³⁴⁺ Ions”. In: *Phys. Rev. Lett.* 87, p. 023201.
- Tan, K.-H. and J. W. McConkey (1974). “Simultaneous ionization and excitation of Ar by electrons with particular attention to configuration-interaction effects”. In: *Phys. Rev. A* 10, pp. 1212–1222.
- Tao, F.-M. and Y.-K. Pan (1992). “An accurate ab initio calculation of the Ne₂ potential”. In: *Chemical Physics Letters* 194, pp. 162–166.
- Taylor, K. T. (1977). “Photoelectron angular-distribution beta parameters for neon and argon”. In: *Journal of Physics B: Atomic and Molecular Physics* 10, p. L699.
- Ueda, K. et al. (2007). “Electron–ion coincidence momentum spectroscopy: Its application to Ar dimer interatomic decay”. In: *Journal of Electron Spectroscopy and Related Phenomena* 155, pp. 113–118.
- Ullrich, J et al. (2003). “Recoil-ion and electron momentum spectroscopy: reaction-microscopes”. In: *Reports on Progress in Physics* 66, pp. 1463–1545.
- Ulrich, B. et al. (2010). “Double-ionization mechanisms of the argon dimer in intense laser fields”. In: *Phys. Rev. A* 82, p. 013412.
- Ulrich, B. et al. (2011). “Imaging of the Structure of the Argon and Neon Dimer, Trimer, and Tetramer”. In: *The Journal of Physical Chemistry A* 115, pp. 6936–6941. eprint: <http://pubs.acs.org/doi/pdf/10.1021/jp1121245>.
- Wadt, W. R. (1978). “The electronic states of Ar₂⁺, Kr₂⁺, Xe₂⁺. I. Potential curves with and without spin–orbit coupling”. In: *The Journal of Chemical Physics* 68, pp. 402–414.

- Wannier, G. H. (1953). “The Threshold Law for Single Ionization of Atoms or Ions by Electrons”. In: *Phys. Rev.* 90, pp. 817–825.
- Ward, S. J. and J. H. Macek (1994). “Wave functions for continuum states of charged fragments”. In: *Phys. Rev. A* 49, pp. 1049–1056.
- Whelan, C. T. et al. (1994). “Coulomb three-body effects in $(e, 2e)$ collisions: The ionization of H in coplanar symmetric geometry”. In: *Phys. Rev. A* 50, pp. 4394–4396.
- Williams, J. F. et al. (2006). “Threshold Electron-Impact Ionization Mechanism for Hydrogen Atoms”. In: *Phys. Rev. Lett.* 96, p. 123201.
- Wiza, J. L. (1979). “Microchannel plate detectors”. In: *Nuclear Instruments and Methods* 162, pp. 587–601.
- Yeh, J. and I. Lindau (1985). “Atomic subshell photoionization cross sections and asymmetry parameters: $1 \leq Z \leq 103$ ”. In: *Atomic Data and Nuclear Data Tables* 32, pp. 1–155.
- Young, T. (1804). “The Bakerian Lecture: Experiments and Calculations Relative to Physical Optics”. English. In: *Philosophical Transactions of the Royal Society of London* 94, pp. 1–16.
- Zaitsevskii, A. V. and A. I. Dement’ev (Dec. 1991). “Radiative decay of the Ar $2+2$ excimer: an ab initio study”. In: *Optics Communications* 86, pp. 461–464.
- Zhang, X et al. (1990). “Energy sharing $(e, 2e)$ collisions-ionisation of helium in the perpendicular plane”. In: *Journal of Physics B: Atomic, Molecular and Optical Physics* 23, p. L173.
- Zhen-Hua, M. et al. (2008). “A Single Photon Imaging System Based on Wedge and Strip Anodes”. In: *Chinese Physics Letters* 25, pp. 2698–2701.
- Zitnik, M et al. (1993). “TDCS for the electron impact ionization approaching the dipolar limit”. In: *Journal of Physics B: Atomic, Molecular and Optical Physics* 26, p. L851.

